國立交通大學

National Chiao Tung University

博士論文

Doctoral Dissertation

複雜氧化物介面交互作用之控制

Controlling the Interaction in Complex Oxide Interfaces

系　　所：　Institute of Physics

學　　號：　9727806

姓　　名：　VU THANH TRA

指導教授：　Prof. JIUNN YUAN LIN

共同指導教授：　Prof. YING HAO CHU

Hsinchu, Friday, June 14, 2013

複雜氧化物介面交互作用之控制

Controlling the Interaction in Complex Oxide Interfaces

姓　　名：	武卿亞	**Student: Vu Thanh Tra**
指導教授：	林俊源	**Advisor: Prof. Jiunn Yuan Lin**
共同指導教授：	朱英豪	**Co- Advisor: Prof. Ying Hao Chu**

國立交通大學

物理研究所

博士論文

A Thesis

Submitted to Institute of Physics

College of Science

National Chiao Tung University

In partial Fulfillment of the Requirements

for the Degree of

Doctor

in

Physics

June 2013

Hsinchu, Taiwan, Republic of China

Abstract

In this thesis, we investigated control the interactions of complex oxide interfaces. Hetero-interfaces between complex oxides have sparked considerable interest due to their fascinating physical properties and offer new possibilities for next-generation electronic devices. While most studies are aiming at exploring new interfaces by combining different materials, another key to realizing the practical applications is the control through external stimulus. As the first subject, we propose a generic approach to use an additional layer, e.g. ferroelectric $Pb(Zr_{0.2}Ti_{0.8})O_3$, on $LaAlO_3$ (LAO)/$SrTiO_3$ (STO) interface as a nonvolatile modulation of the conduction behaviors at this interface. In order to reveal the insight, the change of the interface band structure was comprehensively investigated by a combination of the ferroelectric pattern assisted x-ray photoelectron spectroscopy and scanning tunneling spectroscopy. This study opens an avenue to the nonvolatile control of complex oxide interfaces.

Moreover, in strongly correlated oxides, heterointerfaces provide a powerful route to manipulate the charge, spin, orbital, and lattice degrees of freedom to create new functionalities. As the second part of study, the ferromagnetic (F) $La_{2/3}Ca_{1/3}MnO_3$(LCMO)/superconducting (S) $YBa_2Cu_3O_{7-x}$ (YBCO) heterostructures of two distinct interfaces with atomically precise interface control have been fabricated to explore the interactions between these two functional layers. A new mechanism of charge transfer in these heterostructures was identified. This charge transfer, in addition to the previously considered F/S proximate effect, is critical to the superconductivity, magnetism, and x-ray absorption spectroscopy observed in these heterostructures.

Acknowledgment

This thesis presents the summary of my research work conducted in the Department of Materials Science and Engineering, and Institute of Physics at National Chiao Tung University. I would like to express my sincere gratitude to all the people who helped me during my study.

First and foremost I would like to thank my supervisors, Prof. Jiunn Yuan. Lin and Prof. Ying Hao Chu, for their patient and insightful guidance without which I could not have completed this thesis. My thanks go to the entire Smart Group and Quantum Matter physics groups in National Chiao Tung University, in particular the kind support and help during the experimental work from Prof. Chung Lin Wu, and Prof. Chen Yi Chen' groups in National Cheng Kung University; Prof. Chiu Ya Ping's group in National Sun Yat Sen University; Prof. Chiu Po Wen's Group in National Tsing Hua University, Prof. Lin Hong Ji's group in National Synchrotron Radiation Research Center, Taiwan. I would also like to thank all my friends in the groups for the morale and academic support throughout this work; Especially Dr. Heng-Jui Liu, Dr. Virendra Kumar Verma, Mr. Jang - Jan Chi, Mr. Jhih - Wei Chen, Mr. Yu – Chen Lun, and Mr. Chao-Hui Yeh.

I am grateful to the financial support from the National Science Council of Republic of China (under contract no. NSC-101-2119-M-009-003-MY2), the Ministry of Education (under grant no. MOE-ATU 101W961), and the Center for Interdisciplinary Science at National Chiao Tung University and National Chiao Tung University, especially kindly support from Prof. Jenh-Yih Juang in Department of Electrophysics, National Chiao Tung University for my international conferences trips

My gratitude and thanks are extended to all of my staffs of Institute of Physics and Office of International Affairs (OIA) for dealing with matters such as admission & enrollment registration for International Research Students, an arrival orientation, arrangements of scholarships, housing, visas and organizing various intercultural events.

I would also like to thank the family members of foreign student association – National Chiao Tung University (FSA-NCTU) and Vietnamese student association – National Chiao Tung University (VSA-NCTU) who made my days at National Chiao Tung University really enjoyable and cheerful.

I would like to thank the whole National Chiao Tung University family which made my stay in University and Taiwan a memorable one.

My thanks also go to all those who have played the great sport of Tennis and Badminton with me at National Chiao Tung University.

Finally, I would like to thank my parents and my wife, for their tremendous support, encouragement and kindness

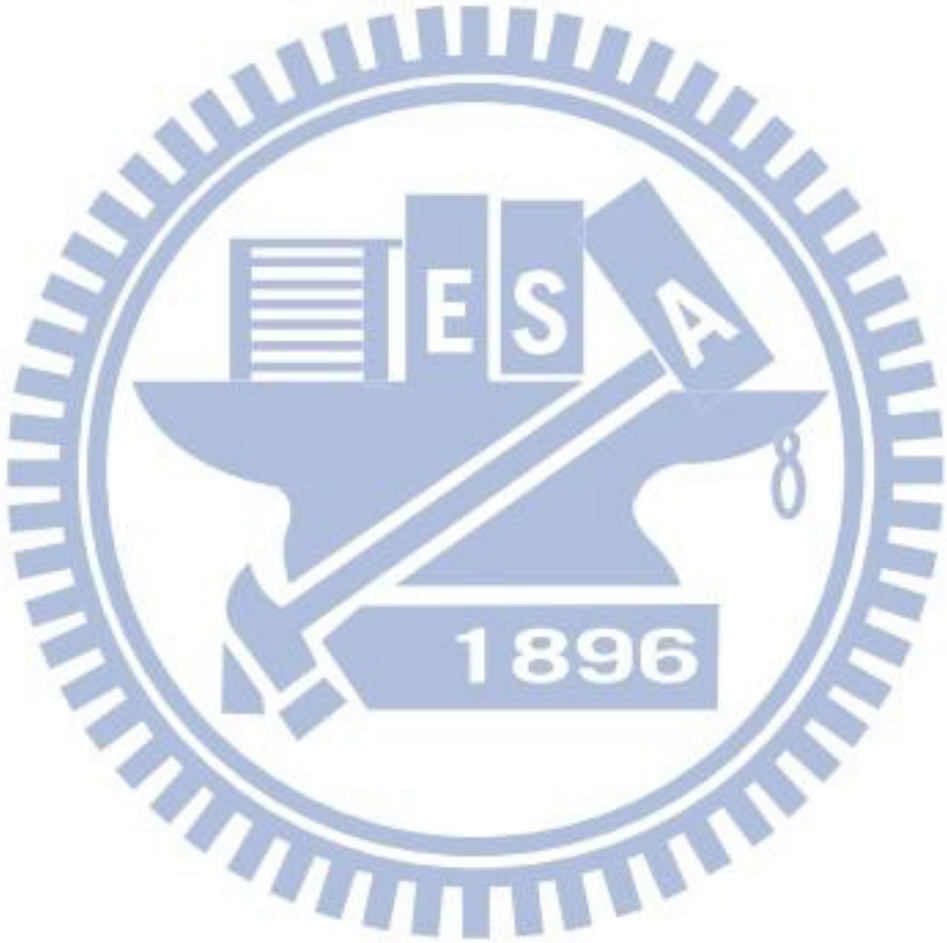

List of Publications

1. C. Y. Wu, **V. T. Tra**, Y. F. Chen, J. K. Lee, and J. J. Lin "Free-electron-like diffusive thermopower of indium tin oxide thin films" J. Appl. Phys. **108**, 123708 (2010)

2. Y. Y. Chu, Y. F. Liao, **V. T. Tra**, J. C. Yang, W. Z. Liu, J. Y. Lin, Y. H. Chu, J. H. Huang, J. Weinen, S. Agrestini, K. D. Tsuei, and D. J. Huang, "Distribution of Electronic Reconstruction at the n-type $LaAlO_3/SrTiO_3$ Interface Revealed by Hard X-Ray Photoemission Spectroscopy", *Appl. Phys. Lett.* **99**, 262101 (2011).

3. B. C. Huang, Y. P. Chiu, P. C. Huang, W. C. Wang, **V. T. Tra**, J. C. Yang, Q. He, J. Y. Lin, C. S. Chang, and Y. H. Chu, "Mapping band alignment across complex oxide heterointerfaces", *Phys. Rev. Lett.* **109**, 246807 (2012)

4. **V. T. Tra**, J. W. Chen, P. C. Huang, B. C. Huang, Y. Cao, C. H. Yeh, H. J. Liu, E. A. Eliseev, A. N. Morozovska, J. Y. Lin, Y. C. Chen, M. W. Chu, P. W. Chiu, Y. P. Chiu, L. Q. Chen, C. L. Wu, and Y. H. Chu, "Ferroelectric control of the conduction at the $LaAlO_3/SrTiO_3$ hetero-interface", *Adv. Mater.* **25**, 3357-3364, 2013

5. H. J. Liu, **V. T. Tra**, Y. J. Chen, D. Yi, R. Huang, H. J. Lin, C. T. Chen, J. -Y. Lin, and Y. H. Chu, "Large magneto-resistance in the magnetically coupled $SrRuO_3$-$CoFe_2O_4$ Self Assembled Nanostructures at room temperature", *Adv. Mater (Accepted).*

6. J. Zhou, C. A. Jenkins, M. Marcus, **V. T. Tra**, R. Trappen, S. Polisetty, E. Wolfe, C. Frye, D. Chen, J.-Y. Lin, Y. H. Chu, and M. B. Holcomb, "Thickness Matters in $La_{0.7}Sr_{0.3}MnO_3/PbZr_{0.2}Ti_{0.8}O_3$Multiferroic Systems", Adv. Mater (accepted).

7. **V. T. Tra**, J.-Y. Lin, Y. -J. Chen, Y.-T. Liu, H. -J. Lin, W. -C. Kuo, J. -Y. Juang, Y.-Y. Chin, J. – M. Chen, J. –M. Lee, J - F. Lee, P. – S. Shi, M. – G. Jiang, C.-T. Chen, Y.-H. Chu, "Termination Control of Charge Transfer in $YBa_2Cu_3O_{7-x}$/ $La_{0.7}Ca_{0.3}MnO_3$ heterostructures", (To be submitted).

Table of Contents

List of Table and Figures

Chapter 2. Introduction

Chapter 3: Experimental Methods

Chapter 4: Ferroelectric control of the conduction at the $LaAlO_3/SrTiO_3$ hetero-interface

Appendix B. Electric field in LAO calculations

Figure B1. X-profile of PZT spontaneous polarization in the stripe 180-degree domain structure (a, b), stray depolarizing field $E_3(x,z)$ existing in LAO layer (c, d) and "sheet" charge $\rho_S(x)$ located in the vicinity of STO surface (e,f). PZT thickness L=50 l.c., LAO thickness H_1=4, H_2=5, H_3=6 l.c., depth z_1=0, z_2=0.5H, z_3=H, domain structure period a=100 l.c. (a, c, e) and a=10 l.c. (b,d, f). Abbreviation l.c. stands for lattice constant units.

Appendix C. Phase-Field Modeling of Ferroelectric Modulation at LAO/STO Interface

Figure C1. (a) Schematic band diagram of STO/LAO/PZT heterojunction; (b) the electric potential distribution in the absence of polarization; (c) the electron concentration in the absence of polarization (z denotes the position in the STO layer, H is half of the layer thickness, so that z/H from -1 to +1 represents the entire layer)

Figure C2. Schematic band diagrams of a PZT/LAO/STO heterojunction in the presence of upward polarization P_{up} (a) and downward polarization P_{down} (b) in PZT layer. The polarization bound charge and electric potential distribution in PZT layer with upward polarization (c) and (d), and with downward polarization (e) and (f)

Figure C3. Comparison of electric potential, electron concentration and local electronic conductivity in STO layer in the presence of upward polarization, no polarization and downward polarization in PZT layer (z denotes the position in the STO layer, H is half of the layer thickness, so that z/H from -1 to +1 represents the entire layer).

Chapter 1: Introduction

As we have known that heterointerfaces based on perovskite oxidies have heralded the possibility of creating new multifunctional properties which would not have been possible to be found by using single-phase bulk materials. The discovery of electronic reconstruction caused the conducting at oxide interfaces has attracted a lot of interest and attention. In addition, heterointerfaces based on oxide thin films show a broad spectrum of generating richer functionality than available with the present conventional semiconductors [1-3]. Since atomic-layer control of the growth is possible in the oxide heterostructures family, the planes along the *c* axis in the ABO_3 perovskite structures can be grown by two alternating layers of AO and BO_2 planes at the interface. When interface effects dominate, different atomic layer stacking sequence at the interfaces presents a variety of opportunities to couple different physical properties at these heterostructures in small length scales. Several studies have successfully demonstrated the unusual atomic and electronic structure at the solid-solid interface of heterostructures [3-7].

A particularly interesting example seems to be presence of a conducting quasi-two electron gas at the interface between the two insulators $LaAlO_3$ (LAO) and $SrTiO_3$ (STO), depending on the terminating layer of the interface. Recently, Ohtomo and Hwang [7] found different electronic behaviour for thin $LaAlO_3$ films on either SrO- or TiO_2 -terminated $SrTiO_3$ substrates, the former interface being insulating and the later interface being n-type conductor. Similar behaviour was found for the $LaTiO_3$ – $SrTiO_3$ interface [8]. So controlling the terminations at the interfaces would be also a key point to study the oxide interfaces. Therefore I have decided to study “Controlling the interaction in complex oxide interfaces” as my doctoral thesis. In the push for practical applications, it is desirable to have the ability to modulate the interface functionalities by external stimulus. So, in the first part of my thesis, “Ferroelectric control of the conduction at the LAO/STO hetero-interface”, we propose a generic approach by inserting a functional layer to the heterostructure to acquire the non-volatile control of the intriguing properties at oxide interfaces. The LAO/STO interface is served as a model system in which a highly mobile quasi-two dimensional electron gas (2DEG) forms between two band insulators [7, 9], exhibiting 2D superconductivity [10] and unusual magnetotransport properties [11]. In this study, we bring in a ferroelectric $Pb(Zr_{0.2}Ti_{0.8})O_3$(PZT) layer nearby the LAO/STO interface. The ferroelectric polarization of PZT layer serves as a control parameter to modulate the 2DEG conducting behaviors. The as-grown polarization leads to charge depletion and consequently a low conduction.

Switching the polarization direction results in a charge accumulation and enhances the conduction at the interface of LAO/STO.

The second part of my thesis, with the title "Termination control of the charge transfer in YBCO/LCMO hetero-structures" is presented in chapter 5. In this part, we study coupling between ferromagnetic (F) and superconductors (S) with two distinct interfaces. It would be one of the topical interests because they offer the appropriate scenario to study competing effects of superconductivity and ferromagnetism on the scale of their characteristics lengths. In addition, coupling between F and S may be understood in two different scenarios: firstly, Cooper pairs of the superconductor may enter the ferromagnet (proximity effect). Second, spins of ferromagnet may enter the superconductor, therefore the proximity effects in F/S interfaces are related to new physical phenomena arising from the interaction between two order parameters that may find potential applications in development of superconductivity and magnetoresistance memory devices. Recent studies the advanced synthesis of epitaxial heterostructures of transition metal oxides, offer intriguing perspectives for the practical realization of such oxide hetero-interfaces. In this regard, Ferromagnetic LCMO and high - temperature superconductor YBCO have been investigated with a variety of experimental methods [2, 12, 13, 14, 15]. However, we are the first ones to examine the coupling between ferromagnetism and superconductivity in $La_{2/3}Ca_{1/3}MnO_3$ / $YBa_2Cu_3O_{7-x}$ heterostructure with different interfaces by Epitaxial design of heterointerfaces. Since both YBCO and LCMO have the ABO_3 perovskite structure, two possible atomic stacking sequences can be formed in (001) – oriented heterostuctures, $La_{0.7}Ca_{0.3}O$ –MnO_2 – BaO – CuO_2 (MnO_2 – terminated interface) and MnO_2 –$La_{0.7}Ca_{0.3}O$ – CuO_2 – BaO ($La_{0.7}Ca_{0.3}O$ – terminated interface). In order to realize this interfacial design, atomically precise interface control is needed and can be achieved by designing LCMO layers with well defined atomic terminations using RHEED controlled PLD growth clearly showing the intensity of oscillation of the specular reflection spot, that indicates a layer –by – layer growth mode with one unit cell precision.

The main focus of this thesis is, controlling the conduction of 2DEG at LAO/STO interface using the ferroelectricity of PZT and study of coupling between the ferromagnetism and superconducting in YBCO/LCMO with different interfaces to understand the physics and explore their applicability in new devices. Therefore, outline of my thesis will include the following parts.

Chapter 2 and chapter 3 of my thesis will give basic background to the rest of this booklet. Chapter two provides an overview of correlated-electron physics, 2DEG and background to the materials such as PZT, LCMO and YBCO, covering basic ideas as well as

a literature review of relevant work. Chapter three discusses the various techniques to fabricate and analyze these structures. This also covers sample preparation and fabrication, as well as in situ and ex situ analysis methods.

The two most important chapters of the thesis, chapter 4 and 5, collate data from some of the experiments during my Ph.D. research. The growth of PZT/LAO/STO and LCMO/YBCO with different interfaces and he properties of these structures as a function of growth parameters such as the functional thickness of each layer during deposition, deposition duration or heterostructure design are discussed. To be more precise, chapter four discusses the structural characterization, electrical transport, X-ray spectroscopy (XPS) and Cross –sectional scanning tunneling microscopy in detail and spectroscopy measurements provide collaborating results. Besides, the theoretical calculations and discussions are also presented. Chapter 5 focuses on the "termination control of the charge transfer in LCMO/YBCO heterostructures. The principles of experiments are similar to those in chapter four, however, here we focus more on how to fabricate with two distinct interfaces to study the coupling between the ferromagnetism and superconducting. Then we also provide the results of the transport measurements and magnetic properties to show quantitatively, how the interface control can manipulate the physical properties in both YBCO and LCMO functional layers. Moreover, the results from XAS provide evidences for the charge transfer at different interfaces which illustrate that only atomically precise control of this interface enabled us to identify a new mechanism of charge transfer in the $YBa_2Cu_3O_{7-x}/La_{0.7}Ca_{0.3}MnO_3$ hetrostructures.

Finally, my thesis closes with a brief summary and supporting materials based on theoretical calculations for the experimental results presented in chapter 5.

References

[1] A. Gozar, G. Logvenov, L. Fitting Kourkoutis, A. T. Bollinger, L. A. Giannuzzi, D. A. Muller, I. Bozovic, *Nature* **2008**, *455*, 782.

[2] J. Chakhalian, J. W. Freeland, G. Srajer, J. Strempfer, G. Khaliullin, J. C. Cezar, T. Charlton, R. Dalgliesh, C. Bernhard, G. Cristiani, H.-U. Habermeier, B. Keimer, *Nat. Phys.* **2006**, *2*, 244.

[3] A. Ohtomo, D. A. Muller, J. L. Grazul, H. Y. Hwang, *Nature* **2002**, *419*, 378.

[4] W. A. Harrison, E. A. Kraut, J. R. Waldrop, R. W. Grant, *Phys. Rev. B* **1978,** *18***,** 4402.

[5] G. A. Baraff, J.A. Appelbaum, D. R. Hamann, *Phys. Rev. Lett.* **1977,** *38***,** 237-40.

[6] Y. Hotta, T. Susaki, H. Y. Hwang, *Phys. Rev. Lett.* **2007**, *99*, 236805.

[7] A. Ohtomo, H. Y. Hwang, *Nature* **2004**, *427*, 423–426.

[8] S. Okamoto, A. J. Millis, and N. A. Spaldin, Phys. Rev. Lett. **2006**, 97, 056802.

[9] N. Nakagawa, H. Y. Hwang, D. A. Muller, *Nature Mater.* **2006**, *5*, 204–209

[10] N. Reyren, S. Thiel, A. D. Caviglia, L. F. Kourkoutis, G. Hammerl, C. Richter, C. W. Schneider, T. Koop, A. -S. Rüetschi, D. Jaccard, M. Gabay, D.A. Muller, J. -M. Triscone, J. Mannhart, *Science* **2007**, *317*, 1196–1199.

[11] A. Brinkman, M. Huijben, M. van Zalk, J. Huijben, U. Zeitler, J. C. Maan, W. G. van der Wiel, G. Rijnders, D. H. A. Blank, H. Hilgenkamp, *Nature Mater.* **2007**, *6*, 493–496.

[12] Chakhalian, J.; Freeland, J.W.; Habermeier, H,-U.; Cristiani, G.; Khaliullin, G.; van Veenendaal, M.; Keimer, B. *Science*. **2007**, 318, 1114–1117.

[13] Stahn, J.; Chakhalian, J.; Niedermayer, Ch.; Hoppler, J.; Gutberlet, T.; Voigt, J.; Treubel, F.; Habermeier, H.-U.; Cristiani, G.; Keimer, B.; Bernhard, C. *Phys. Rev. B.* **2005**, 71, 140509.

[14] Soltan, S.; Albrecht, J.; Habermeier, H.-U. *Phys. Rev. B.* **2004**, 70, 144517.

[15] Sefrioui, Z.; Arias, D.; Pena, V.; Villeegas, J.E.; Varela, M.; Prieto, P.; Leon, C.; Martinez, J.L.; Santamaria, J. *Phys. Rev. B.* **2003**, 67, 214511.

Chapter 2: Background

Recently, heterointerfaces between the complex oxides materials have been an interesting class encompassing the full spepiezoelectric in electronic field, ferromagnetic, multiferroic in magnetic field of physical properties, such as insulating, semiconducting, metallic, superconducting, ferroelectric, and ear optical effects in optics field. These vast physical properties also have a strong correlation to structural variation that can be induced by ambient condition like temperature, pressure, magnetic field, electric field, *etc*., and offer new opportunities for electronic applications. This chapter will give an basic introduction to the key concepts of two dimensional electron gas (2DEG) LAO/STO interface, ferroelectricity of PZT, ferromagnetism of LCMO and superconducting of YBCO and describe the detailed information of corresponding materials in this work.

2.1. Some concepts about 2DEG in correlated-electron oxides and semiconductors

2.1.1 Introduction

One of the fastest and most pervasive technologies of the last decades was semiconductor physics. In a fascinating interplay between theoretical understanding, experimental acumen and technological applications the field was developed rapidly and extensively due to fascinating physical properties and also offering more possibilities for the next generation of electronic devices. Therefore, most of studies are arming at exploring the new interfaces to create the new functionalities. Moreover, in strongly correlated oxide interfaces, heterointerfaces provide a powerful round to manipulate the physical properties (charge, spin, orbital and lattice degree of freedom) and also understand the physics behind which are not able to be found in the single bulk materials. Moore's law [1] would not have been possible without this development. Two-dimensional electron gases (2DEG) probably are one of the prime examples of this innovation. It can be understood the fundamental and principles of 2DEG from quantum mechanics (it can be found in any quantum mechanics books like Sakurai [2] or David Grifiths [3]), and their realization was only made possible once the experimental fabrication techniques were well developed ; there was a gap of about 50 years between concept and device. Once available though, the 2DEG provided a path way and new opportunities for research and development to our future devices. Now we can strongly confirm that 2DEG of LAO/STO is device. In recent years the growth of transition

metal oxides have been studied by different methods, especially by Pulsed laser deposition (PLD) or laser Molecular beam epitaxial (MBE), and has risen to similar levels of control and *in situ* monitoring [4, 5] resulting in the fabrication of high-quality films and heterostructures of these oxides [6–9]. This small part of the chapter gives an overview of theory of quantum wells and correlated electron materials as well as previous work on the systems under investigation here: LAO/STO interfaces. This lays the physics foundation in the later chapters.

2.1.2 The physics background of 2DEG

In Quantum Mechanics, the based and also the fundamental problem is considered the particle-in-a-box example in which a single particle is confined to a certain area by an external potential and described by the time – independent Schrodinger's equation as follows (one-dimensional):

$$-\frac{\hbar^2}{2m}\frac{d^2\Psi}{dx^2}+V\Psi=E\Psi \qquad \textbf{(2.1)}$$

where ($\hbar$) is the reduced Planck's constant, m is the mass of particle, Ψ is the total wave function of electrons, x is the position, V is the (in) finite external potential and E the (eigen) energy of the system. For an in finite external potential, the particle is truly confined, in this case the energies are quantized as

$$E_n=\frac{n^2h^2}{8mL^2} \qquad \textbf{(2.2)}$$

where n is the quantum number and L is the size of the potential well. Or if we set k=n/2L and as the wave number and h= $\hbar/2$, we obtained:

$$E_n=\frac{\hbar^2k^2}{2m} \qquad \textbf{(2.3)}$$

For the realistic case, the potential is finite and the wave function is not completely contained within the potential well. This is shown schematically in **Figure 2.1**. This simple one-dimensional picture can be extended to three dimensions, but in my thesis, we just focus on two-dimensional layers which electrons are confined in only one direction in between the interface of LAO and STO layers of n-type interface. In such of that the particles are confined perpendicular to the layer, but are free to move within the layer (in plane). In that case, any additional quantum properties are well described by the one-dimensional case.

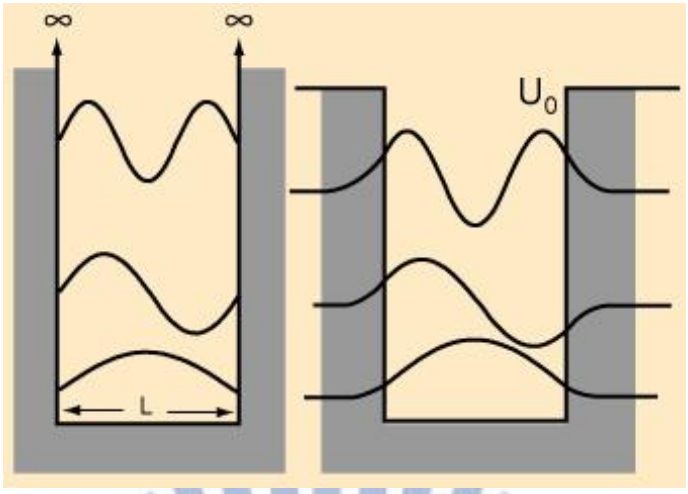

Figure 2.1 *The energy levels of electrons in quantum well: an infinite (left) and a finite (right), taken from Ref. [10].*

2.1.2.1 Potential wells in semiconductors

So far quantum theory has shown that a single particle in a potential well has distinct, numbered energy levels. To realize such a 2DEG system in an experimental device, three conditions need to be met:

1. There has to be a potential well;
2. There have to be particles, here electrons, within the potential well;
3. The electrons within the well should not interact significantly.

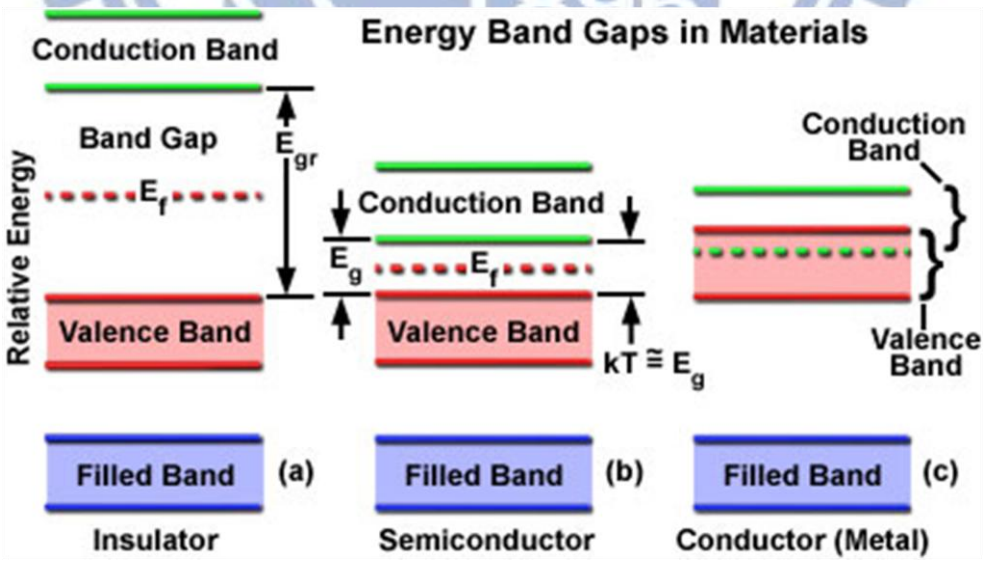

Figure 2.2 *The band structures of simple single materials:* **a)** *insulators,* **b)** *semiconductors and* **c)** *conductors, figure was taken from Ref. [11].*

Again, the interplay between theory and experiments should be the pathway to such future devices. The application of quantum mechanics to solid state science gave rise to band structure theory. There, the (electrical) properties of materials are defined by the appearance of collections of electron levels named bands which we would like to introduce in **Figure 2.2**.

If the Fermi level is within a gap between two bands and thermal fluctuations do not excite some electrons to the upper, conducting band, the material is an insulator (see **Figure 2.2a)**). However, if some electrons are excited to the conduction band, it is a semiconductor (**Figure 2.2b)**). If the Fermi level, the maximum energy level electrons can reach if the system is in its ground state, is within such a band, it is a conductor. See **Figure 2.2 c).** The band gap is unique for each semiconductor material. **Table 2.1** shows some band gaps for representative semiconductors and oxides.

material	band gap E_g (eV)	effective mass m^* (–)	electron mobility μ (cm^2/Vs)	electron density n (cm^{-3})
Si	1.12	1.08	1300	$2.0 .10^{16}$
GaAs	1.42	0.067	6000	$3.0 .10^{15}$
AlAs	2.168	0.146	200	$2.0 .10^{17}$
Nb:$SrTiO_3$	1.8	6	3.2	$1.4 .10^{17}$
$LaAlO_3$	5.6	-	-	-

Table 2.1 *Basic parameters for some representative semiconductors and oxides at room temperature [*12–16*]*.

From **Table 2.1** it can be seen that the band gap varies substantially. By layering different semiconductors a potential well can be created. An example of such a potential well is shown in **Figure 2.3**.

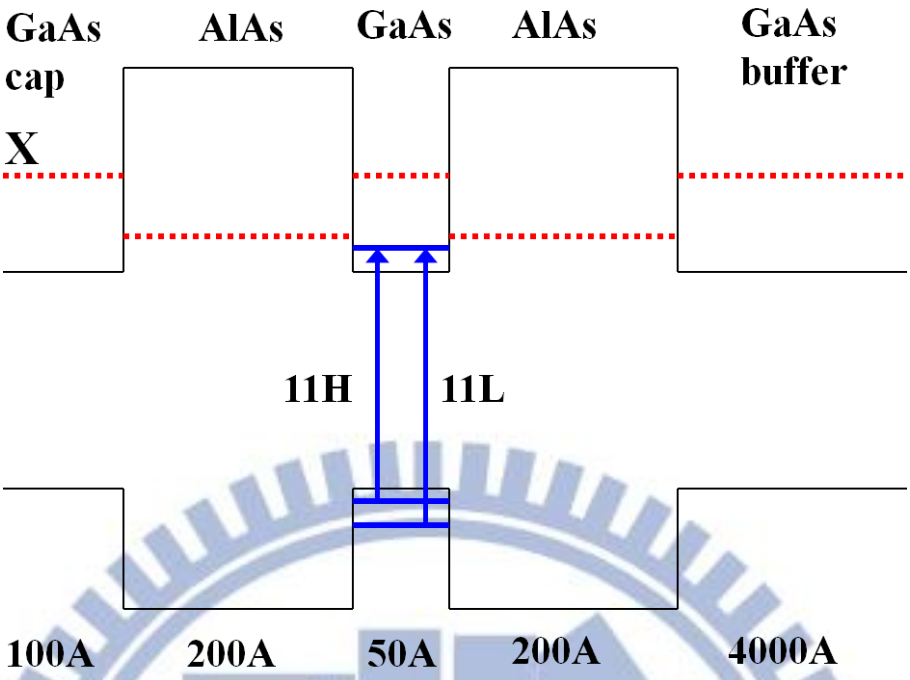

Figure 2.3 *Band diagram of a simple semiconductor potential well, taken from Ref [16].*

The problem is how to get electrons into the potential well. By doping in the semiconductor with atoms of an element that having valence electrons is also one of standard methods. Silicium is four-valent. Doping with phosphorus, which is five-valent would result in an excess of electrons after covalent bonding. These 'excess' electrons are now doped into the conduction band and can freely move throughout the potential well. Such doped atoms, however, also form scattering centers which inhibit mobility of the electron. As the electrons should be disturbed as little as possible within the potential well, the active layer (the central GaAs layer in **Figure 2.3**) should not be doped. Here an additional bonus of the potential well appears. If the layers to the side of the actual well are doped, the free electrons will search out the energy minimum within the well as their ground states. Therefore, the number of electrons within the well can be controlled, without disturbing the crystal perfection of the well itself. This control also gives the opportunity to make sure the electrons are independent from one another. As long as the mean free path is much smaller than the average distance between electrons and the electron-electron interaction will be negligible. Thus, by controlling the density of electrons within the potential well the independent electron regime can be maintained.

2.1.2.2 Independent vs. correlated electrons

With the time - independent electron approximation and the inclusion of electron correlation, the Schrodinger equation can be examined as the following form:

$$-\sum_i \frac{\hbar^2}{2m}\nabla_i^2\Psi + \sum_{\langle i,j\rangle}\frac{1}{2}\frac{e^2}{\varepsilon K\left|\vec{r}_i-\vec{r}_j\right|}\Psi - \sum_{i,j}\frac{e^2}{\varepsilon K\left|\vec{r}_i-\vec{R}_j\right|}\Psi = E\Psi \qquad \textbf{(2.4)}$$

Where, the first term is free electron contribution. The other terms described the interactions formed by the other electrons and ions in the system. The second term of the Schrodinger equation describes the electron-electron interaction, while the third describes the electron-ion interaction. In the independent electron approximation the electron correlation is thought to be ignored. Also, the ions are much more massive than the electrons, so their movement is also negligible. These two assumptions greatly simplify **Equation 2.4** and thus successfully lead to much of the solid state theory in the beginning of the last century. It made the complex Schrodinger equations tractable before the advance of complex numerical calculations like density functional theory that are nowadays able to work with the full, correlated Schrodinger equations. However, the independent electron approximation is not able to explain several important physical properties such as (anti)ferromagnetism, the Mott insulating state and superconductivity. The single-band Hubbard model is often used as a starting point of the discussion of correlated materials. It simplifies the treatment of the background ions, but explicitly includes the electron-electron interaction. The Hamiltonian of the model is given as:

$$H = -\sum_{\langle i,j\rangle\sigma} t_{ij}c_{i\sigma}^{\dagger}c_{j\sigma} + U\sum_i n_{i\uparrow}n_{i\downarrow} \qquad \textbf{(2.5)}$$

where t_{ij} is the hopping parameter between nearest-neighbor sites i and j, $c_{i\sigma}^{+}(c_{i\sigma})$ is the creation (annihilation) operator for an electron on site *i* with spin $(\uparrow \text{or } \downarrow)$, U is the Coulumb energy and $n_{i\sigma} = c_{i\sigma}^{+}c_{i\sigma}$ is the electron occupation of site *i*. The physics of transfer integral captures where delocalizing an electron lowers its energy, similar to Bloch waves and thus represents the kinetic term from **Equation 2.4**. The Coulomb energy denotes the energy it costs to bring two electrons in close proximity, i.e. on the same site. By varying the total number of electrons and the relative energies of t_{ij} and U, a large phase space of properties opens upon. It is the recent and current interest in these properties then using the ferroelectricity to modulate the conductivity and their physical properties.

2.1.3 Polar/non-polar interfaces

As we mentioned above, an example of a polar interface was described: the LAO (001) surface. There is a charge discontinuity between the LaO//AlO2 stacking and the 'vacuum'. The LAO consists in this orientation of alternating layer of $(La^{3+}O^{2-})^{+}$ and $(Al^{3+}O_2^{2-})^{-}$ while the vacuum has an effective charge of zero. Such discontinuities are often resolved by a surface reconstruction in bulk materials [17, 18]. However, such polar discontinuities can also occur inside heterointerfaces; a fact that is very famous from semiconductor physics, where it results in an ionic reconstruction at the interface between different semiconductors or in between layers of the materials have different band structures [19]. In correlated-electron materials, similar the redistribution of electrons to be found in the LTO/STO system. Moreover, the electronic reconstruction at domain walls in $BiFeO_3$ is also found [20, 21, 22], where the polarization discontinuity induced or enhanced to a conducting interface and the destruction of half–metal in $Fe3O_4/BaTiO_3$ due to the electron transfer across the interface [23].

2.1.3.1 Charge transfer at $LaAlO_3/SrTiO_3$ interfaces

The big discovery in 2004, by Ohtomo and Hwang showed that the interface between LAO and STO in the (001) direction can be conducting, depending on the termination at the heterointerface. Such an interface exhibits a polar discontinuity, as LAO has alternating planes ± 1, while the $Sr^{2+}O^{2-}$ and $(Ti^{4+}O_{2+}^{2-})$ planes of STO are neutral [24]. In a purely ionic picture, this discontinuity transfers either only half an electron per unit cell area from LAO into STO for a n-type interface or half a hole per unit cell area for an p-type interface. **Figure 2.4** shows how the electrons and holes are distributed in this model. The former interface is found to be conducting as shown in **Figure 2.4a)** with TiO_2 termination took a place the top of STO (100) substrate, and we know it as n-type LAO/STO interface, while the latter, though nominally hole-doped, is insulating with SrO termination as **Figure 2.4b)** and is called as a p-type interface. Therefore, we can conclude that the hole-doping of closed shell ions is very difficult and complicated, moreover the compensation of holes by oxygen-vacancy would be a key point to be induced electrons results in no net free carriers [25, 26].

a) n-type interface b) p –type interface

Figure 2.4 *The model of charge transfer at LAO/STO interfaces. Diagrams taken from Ref.[25*].

To understand the mechanism behind that, the purely ionic picture is never complete for a correlated-electron material. In other hand, more physical way to explain clearly these results is by looking at the internal dipole that develops across the charged in the LAO layers. In the electronically unreconstructed case, the transition of neutral to immediately charged layers results in a potential build-up due to the electric fields between the oppositely charged layers in LAO (**see Figure 2.5**). This 'polar catastrophe' grows with the LAO thickness and has to be compensated when the energy can no longer be accommodated by internal deformations [27–29]. In a band diagram, this happens when the potential build-up becomes larger in energy than the band gap of STO [29–32]. The valence band of LAO goes higher than the Fermi level, allowing for the charges transfer from the top surface to the interface. This reduces the potential build-up, as seen on the right panel in **Figure 2.5**. Recently, an argument has been made for the existence of in-gap states to which electrons can tunnel [33]. However, their theoretical calculations prove a constant electron density does not depend on the LAO layer thickness, contrary to experimental results [34, 35].

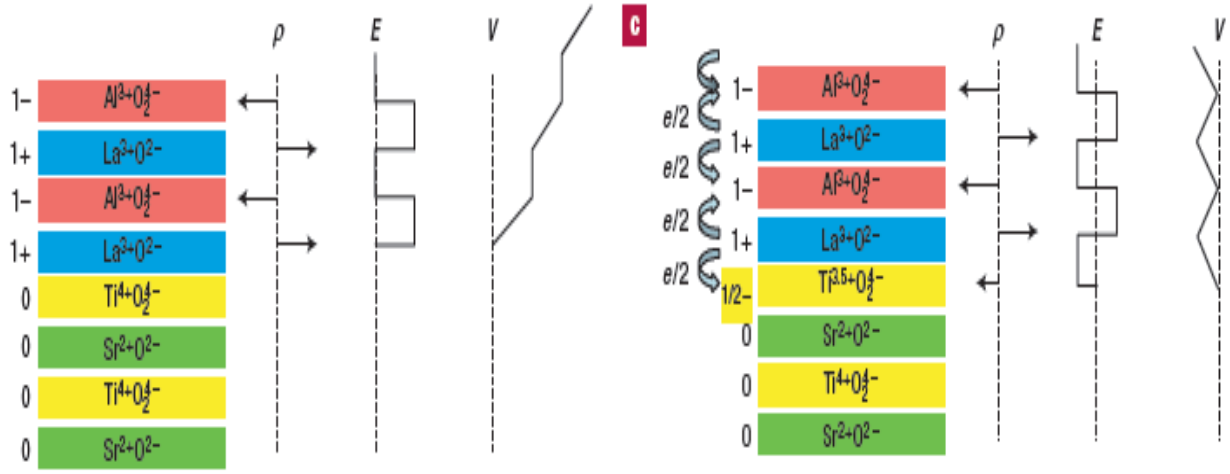

Figure 2.5 *Illustration of the polar catastrophe in an unreconstructed case (left) and a re-constructed case (right), where only half an electron is transferred into the TiO_2 layer. Diagrams are taken from Ref.[25*].

To examine the n-type LAO/STO interface where the terminations at interface controlled by TiO_2-LaO, the crossing of the potential build-up and the band gap implies that up to a critical thickness of the LAO layer, this dipole can be accommodated by the strain within the LAO and no electronic reconstruction (i.e. electron-doping into the TiO_2 layer) occurs. That critical thickness has been found to be 4uc, below that it was still insulating, however, when the LAO thickness reaches 4uc, an abrupt change into conductivity interface [36]. Thicker LAO layers show a decreasing mobility, though the mechanism behind that behavior is one of the many unsolved mysteries in this system [35]. Theoretical calculations actually show a larger critical thickness, but this can have several explanations. One is that the supercell used in the calculations is too small, so we did not include all possible reconstructions of electrons [28, 37]. Another explanation is that in real samples there are surface defects that form in-gap states, so the LAO band needs to shift less before electrons are doped [29, 38]. Finally, (Density functional theory) DFT always has a problem calculating the band structure of materials, which may make these calculations only qualitative, not quantitative. This thickness effect can be used to pattern structures into the conducting layer by selectively depositing thick LAO [39]. Only in those areas where the LAO layer is thicker than 4uc the built in potential is large enough to trigger the electronic reconstruction at the interface and create a conducting interface. Or, by having the dipole develop to just below the threshold value for electronic reconstruction, the conducting state can then be induced by introduction to the LAO layer an electric field and thus altering the dipole across this layer. This can be

done either by a back-gate field-effect transistor configuration [36, 40] or by writing with a conducting AFM tip [41, 42]. Interestingly, this minimum thickness of LAO required for a conducting interface does not seem to apply when the LAO layer itself is again capped with STO. The created two different interfaces of LAO/STO (one is n-type, another is p-type) where n-type LAO/STO is conducting down to a single monolayer (unit cell) of LAO embedded in STO [34, 43, 44]. There is, however, a clear interaction between the two interfaces. Below a LAO thickness of about 6 uc the sheet resistance increases. Hall measurements show that this is due to a decrease of the electron density in the 2DEG, while the electron mobility is constant (as opposed to single interfaces, where the mobility decreasing with increasing thickness [35]). More interestingly, about half a year earlier a jump in the optical absorption spectrum of LAO/STO superlattices samples as observed which does not appear in alloyed films of the same chemical composition [45]. The $LaNiO_3/SrMnO_3$ system also undergoes an insulator-to-metal transition upon increasing the thickness of $LaNiO_3$ layer [46]. Ionically, the system does have a polarization discontinuity ($La^{3+}Ni^{3+}O_3 / Sr^{2+}Mn^{4+}O_3$) so electron reconstruction may play a role here. The analysis of the transport behaviour points to a more complex conduction mechanism for this system compared to the LAO/STO system.

In general case, the electron gas acts as a Fermi liquid with a $1/T^2$ behaviour of the electron mobility[24, 34, 47–49], varying from ~ 6 cm^2/Vs at room temperature to ~1000 cm^2/Vs at 5 K. This correlated electron liquid model was confirmed by scanning tunneling spectroscopy [50]. Though in general the electron-electron interactions are weaker than electron-phonon interactions at room temperature, in STO they are typically weak (as seen from the poor heat conduction) and would give rise to different temperature dependence [34]. The electron density depends on so much of fabrication parameters such as substrate termination [47], oxygen pressure during deposition [24, 49, 51, 52] and, laser frequency in PLD chamber [53]. There is some argument for intermixing [25, 54, 55], but transmission electron microscopy images do not give conclusive evidence. Also, if intermixing would occur, the complimentary p-type interface should also become conducting [47]. A thermally-activated behavior of the electron density, similar to that in semiconductors, with an activated energy of about 6 meV was observed [34]. This point is weakly-bound donors as the source of the electrons [42]. In general, electron densities on the order of $10^{14} cm^{-2}$ at room temperature are achieved.

Remarkably, at low temperatures almost all data converge to a value around $2\times10^{13} cm^{-2}$ [34, 36, 52, 56–58]. These values for the electron density would translate to, respectively, about 0.15 and 0.03 electron per unit cell area at room temperature and 5 K. This value is far below the nominal half electron per unit cell area transferred in the purely ionic model above. One explanation might be that the electrons are distributed over different sub-bands, of which only some contribute to the (Hall) free electron density [59]. However, XPS detects both free and bound electrons and the densities observed with this technique are close to those obtained from Hall measurements [60]. **Table 2.2** compares the transport properties of semiconductor (Si and GaAs) and correlated-electron (LTO/STO and LAO/STO) systems. The electron mobilities in semiconductors are always higher than those in correlated-electron materials. This is not surprising, because the mobility is limited by the scattering of electrons, either from ions or with other electrons. Thus correlated-electron materials, with their higher electron densities, will almost always display lower mobilities than semiconductors.

system	m^* (–)	μ (cm^2/Vs)	n_{3D} (cm^{-3})	n_{2D} (cm^{-2})
Si	1.08	1300	$2.0 .10^{16}$	
GaAs	0.067	6000	$3.0 .10^{15}$	
ZnO / $Mg_xZn_{1-x}O$	0.32	160		$2.5 .10^{13}$
Nb:STO	1.8	6	$1.4 .10^{17}$	
LTO / STO	1.8	3	$8 .10^{21}$	
LAO / / STO	1.5	6		$1.2 .10^{14}$

Table 2.2 *Comparison of the transport properties at room temperature for semiconductor and correlated-electron systems, [12–14, 34, 61].*

To study the possibility of quantum effects in these electron gases, the requirements for Shubnikov-de Haas oscillations can be studied. The occurrence of these oscillations is a clear sign of the quantum nature of the electron gas (see **Table 2.2** and discussion).

2.2 Fundamental properties of Ferroelectricity (PZT)

A ferroelectric material is a subset of piezoelectrics which exhibits a spontaneous electric-polarization that can be reversed by the application of an external electric field.

2.2.1 Perovskite crystal structure

PZT crystallizes in perovskite structure. The illustration of crystal structure is shown in **Figure 2.6.** Here we have used the ABO_3 perovskite structure of Barium titanate ($BaTiO_3$) as an example. The corners sharing A site are occupied by Ba^{2+} ions; O^{2-} ions occupy the interstices, which share electrons with neighboring cells; and Ti^{4+} ions occupy the central position, i.e B-site. In this figure, the central ion is not displaced, thus there is no dipole direction in the cubic phase being exhibited in the structure.

When the temperature is below the Curie temperature, a phase transition from the paraelectric phase to the ferroelectric one takes place in the crystal and electric dipoles form as the central ions displace with respect to the Ba^{2+} ions. In the tetragonal structure, there are 6 possible dipole directions which are corresponding to the central ion may shift up, down, left, right or in and out of the page. However, for the rhombohedral phase, the central ion is took a place along the diagonal towards any of the corner ions, resulting in 8 possible dipole directions. Therefore, one the central ions are displaced, that results in deformation of the shape of the entire cell. For example, when a tetragonal structure is formed as a result of the displacement of central ion in upward direction, the resulting unit cell elongates toward up-down directions. As a consequence, dipoles in neighbouring unit cells are displaced in the same direction, resulting in a knock on effect forming a region that is similar with dipole orientations, knowing as a domain in PZT or perovskite structure [62].

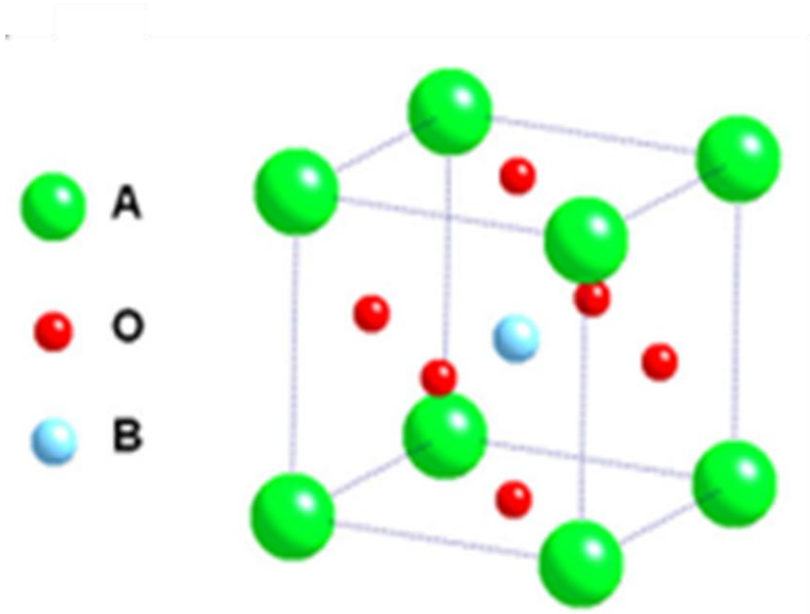

Figure 2.6 *ABO_3 perovskite crystal structure*

2.2.2 Poling

Usually, polarization states of materials form as the natural polarization state of the as grown samples which depends on the materials, its natural polarization may have upward polarization state, downward polarization sate or even mixed states, and it can be switchable, so in order to produce a material with a net polarization and hence piezoelectric properties, domains need to be aligned. The switching polarization directions can be achieved by the application of an external electric field, resulting in the domains aligning with the field. Finally, when the electric field and heat are steadily removed and resulting the polarizations of the domains become 'frozen' in the new aligned directions. This process is called as 'poling' or "switching". The polarization of a material after the poling field is removed is called the remnant polarization, P_R. The maximum polarization achievable during poling is restricted by the available domain states in the material, and it is a function of spontaneous polarization, Ps. In tetragonal polycrystalline ferroelectrics with 6 domain states, the maximum P_R can be achieved is about $0.83P_S$. Whereas, comparing with the Rs, in a rhombohedral polycrystalline ferroelectric with 8 domain states, the maximum P_R achievable is 0.87 Ps [63]. In practice, the achievable remnant polarization is always lower due to complex domain boundary and stress states.

2.2.3 Ferroelectric hysteresis loops

All ferroelectric materials exhibit the characteristic of domain polarization reversal under the application of an external electric field. And the consequence of the domain switching is a non-linear hysteretic loop; In **Figure 2.7**, at small electric fields (**Figure 2.7 A**), the polarization increases linearly, which occurs because of the fact that the field is not large enough to result in the switching of domains with oppositely polarization direction. As the electric field increases (**Figure 2.7 B**) oppositely orientated domains start to switch towards the electric field. At larger applied electric fields (**Figure 2.7 C**), the polarization saturates as oppositely polarized domains switch in the direction of the field until a maximum polarization, known as the saturation polarization and often called as Ps, is achieved. When the electric field is reduced, hysteresis is observed. At zero electric field, there is a non-zero polarization, this is known as the remnant polarization, P_R. To de-polarize the material a negative electric field must be applied, whereby the polarization exhibited can be reversed until saturation is reached (**Figure 2.7 D**). The electric field required to reduce the polarization value to zero is known as the coercive field, Ec. The P_R, Ps, Ec and shape of the hysteresis loop are affected by lattice defects, residual stress, mechanical strains and thickness of the material [62].

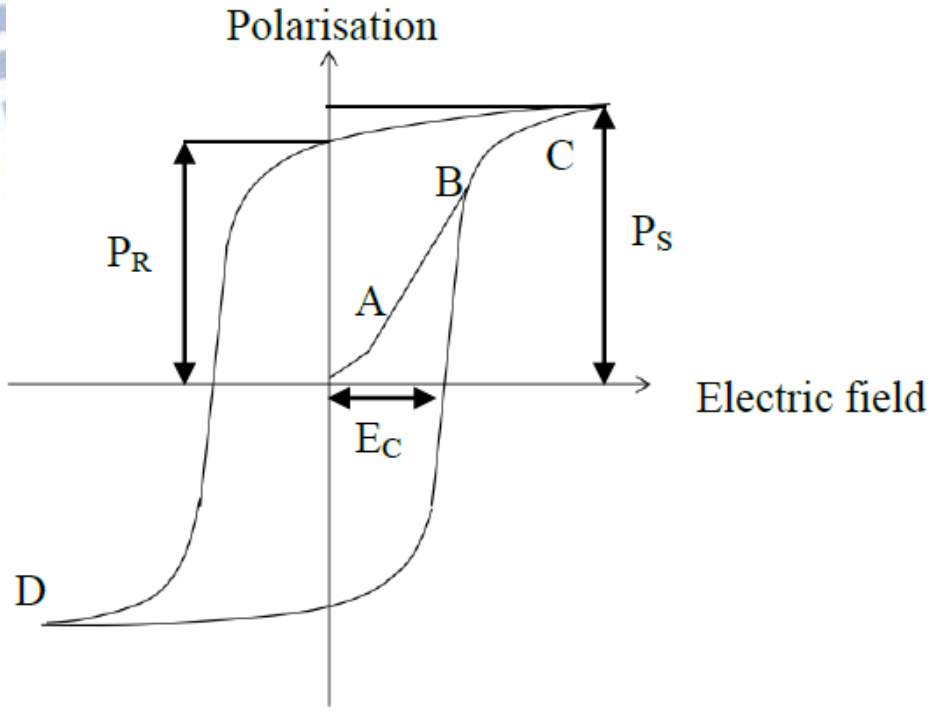

Figure 2.7 *Hysteresis loop of a ferroelectric material: ferroelectric polarization as a function of the applied electric field [62].*

2.3 Ferroelectricity of PZT

2.3.1 Introduction

As we know that the first successful custom man-made piezoelectric material integrated into electrical circuits was barium titanate, and was developed in the 1940s. The piezoelectric effect of these materials was always found to be higher than that in naturally occurring materials, and the properties could be tailored to specific applications. Therefore, the development of PZT in the 1950s gave the foundation for the applications in the industry, because the ferroelectric polarization was found to have a higher piezoelectric coefficient and energy conversions than that of barium titanate. Consequently, PZT (or also BFO) is the most famous piezoelectric ceramic used in industry nowadays. PZT ceramics exhibit dielectric, piezoelectric and ferroelectric properties. Therefore, the previous discussions are extended to explain how PZT ceramics function [62], which has widely been studied recently.

2.3.2 Crystal structure

PZT is the ABO_3 perovskite structure. At the A sites, Pb^{2+} ions exist and at the B sites Ti^{4+}/Zr^{4+} ions exist. The crystal phase of a PZT crystal unit cell is dependent on the ratio of Zr to Ti, and the temperature. The phase diagram of PZT is shown in **Figure 2.8**. At high temperatures, a paraelectric cubic phase exists. During cooling below the Curie temperature of the material, dipoles develop giving rise to the ferroelectric phase. At Zr-rich compositions a rhombohedral crystal structure is exhibited, and at Ti-rich compositions a tetragonal crystal structure is exhibited. At room temperature the boundary between phase transitions occurs when there is 52:48 ratio of Zr:Ti. This is called the morphotropic phase boundary (MPB), and materials of this composition have been shown to exhibit a peak in piezoelectric and dielectric properties. One reason for this is that at the MPB 14 polarization directions are possible; 8 polarization directions associated with the rhombohedral phase and 6 with the tetragonal phase. PZT crystallizes at the MPB therefore may exhibit 14 directions along which the domains may be re-orientated during poling, resulting in a large polarization [63].

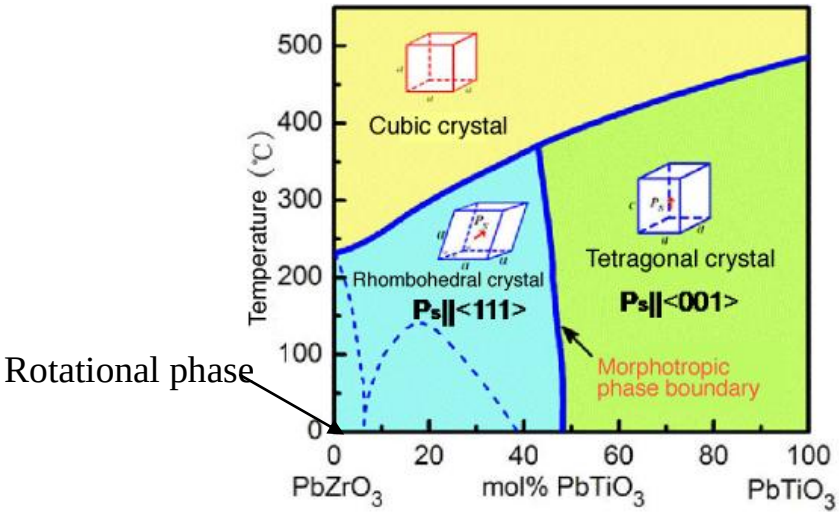

Figure 2.8 *Phase diagram of PZT, taken from Ref.[63]*

2.3.3 Domain formation in PZT

In PZT, the domains exist within the grains, and the width of a domain is proportional to the square root of the size of the grain [62, 64]. Knowing the parabolic relationship between size of a grain and a domain suggests that sub-micrometer grains would accommodate a maximum of one domain. However, Randall *et al.* (1998) suggested that density of a domain increases with dimension of grain size is below 1μm in bulk materials [65]. More examinations of the formation of domain in PZT thin-films integrated with substrates were carried out [66]. It was observed that there were no domain boundaries in grains of sizes lower than 0.2μm, indicating that single domains are being accommodated. For grain sizes varying from 0.2-1.0 μm, they observed a 90˚ domain wall boundary thus two domains existing per grain with a ferroelastic domain boundary. Furthermore, for grain sizes greater that 1 μm, increasing in the number of domains was observed. These domain formations are illustrated in **Figure 2.9**.

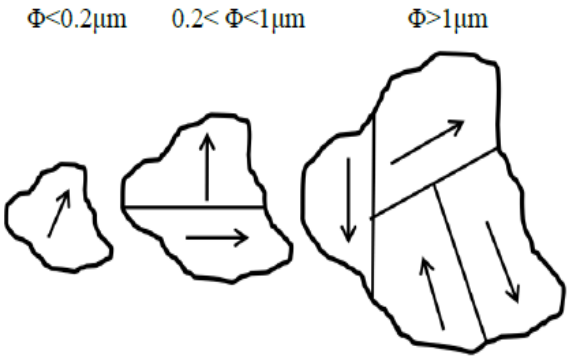

Figure 2.9 *Illustration of possible domain formations within grains [62].*

The number of domains accommodated in a grain has an effect on the orientation of the domains. To minimize electrostatic and elastic energies, the ferroelectric and ferroelastic domains boundaries were well developed and discussed. However, this occurs only when there are neighboring domains present. So, in small grains where only a single domain may be accommodated, these boundary effects are not exhibited. This may result in unrelieved domain boundary strains. When two domains exist within a grain, there is a reduction in the strain pertaining to domain boundary and as a consequence of a ferroelastic domain one [66]. Moreover, there is a reduction in grain-domain wall coupling, resulting in a greater probability of re-orientation during poling. When multiple domains exist within a grain, that leads to development of more complex ferroelectric and ferroelastic domain boundaries. Due to a reduction in inter-domain strains as a consequence of ferroelastic boundaries, and also a reduction in coupling of grain-domain wall, the result would be in increasingly effective domain re-orientation during poling.

In order to produce PZT ceramics with high piezoelectric capabilities, domain re-orientation during the application of a poling field is essential. The efficiency of this observed to be reduced when domains are pinned. It has been explained that this can arise due to grain-domain wall coupling. Besides this, ‘pinning’ occurs in PZT films as a consequence of an integrated substrate. This is examined more closely in chapter 4.

2.4 Ferromagnetism and physical properties of LCMO

In this section, the fundamentals of magnetism are briefly explained. An introduction to the major classes of magnetic behavior is presented via the concept of long-range magnetic order, with a special focus on the phenomenology of ferromagnetic materials. Especially, we focus on physical properties of LCMO.

2.4.1 Magnetism and Magnetic Order

Unlike the ferroelectrics, which have time-reversal symmetry and non-spatial-inversion symmetry, the magnetic crystals break time-reversal symmetry and keep spatial inversion invariant (**Figure 2.10**) [67, 68].

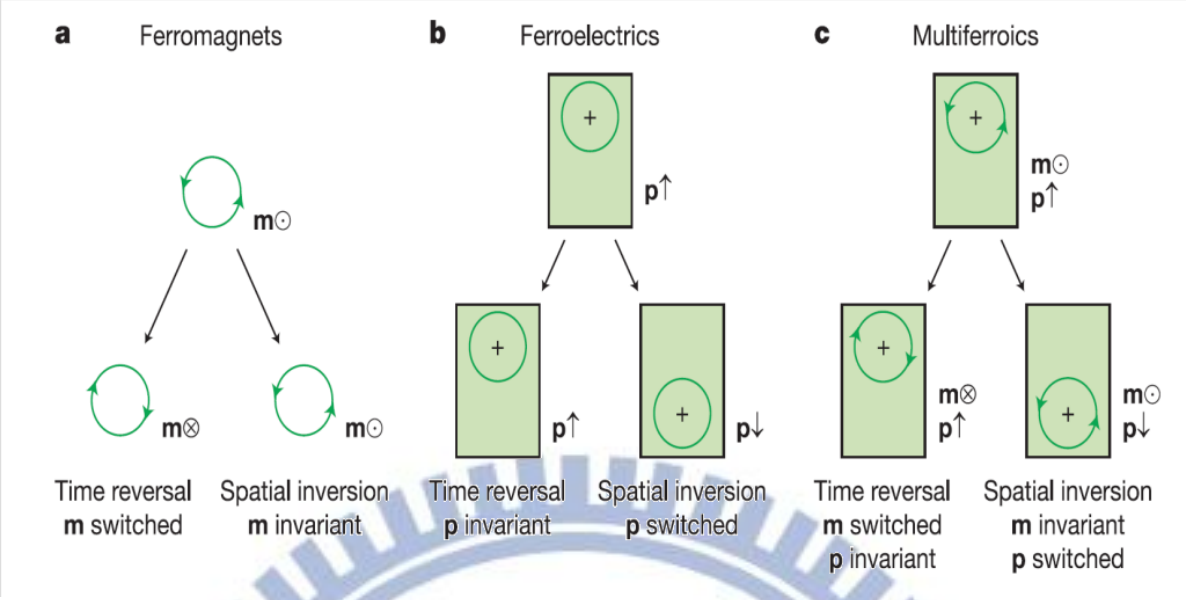

Figure 2.10 *Time-reversal and spatial-inversion symmetry in ferroics.* ***a)*** *Ferromagnets: the local magnetic moment m may be represented classically by a charge that dynamically traces an orbit, as indicated by the arrowheads. A spatial inversion produces no change, but time reversal switches the orbit and thus m.* ***b)*** *Ferroelectrics: The local dipole moment p may be represented by a positive point charge that lies asymmetrically within a crystallographic unit cell and has no net charge. There is no net time dependence, but spatial inversion reverses p.* ***c)*** *Multiferroics that are both ferromagnetic and ferroelectric possess neither of the symmetries [67].*

This means that the magnetic moments is reversed by time inversion to present pairs of time-conjugate orientation states, and any time-conjugate orientation states must be anti-parallel with respect to original spontaneous magnetic vector. The symmetry for magnetic crystal can be subdivided into 122 kinds of magnetic space groups because the typical 32 crystallographic point groups cannot fully describe it. Of these magnetic space groups only 31 kinds belong to the ferromagnetic materials. The ferromagnets are the materials possessing spontaneous magnetization caused by long range and parallel alignment of unpaired spinning and orbiting electrons in the absence of the magnetic field. The similar “domain” concept in ferromagnetics also presents a hysteresis loop under the manipulation of magnetic field [69].

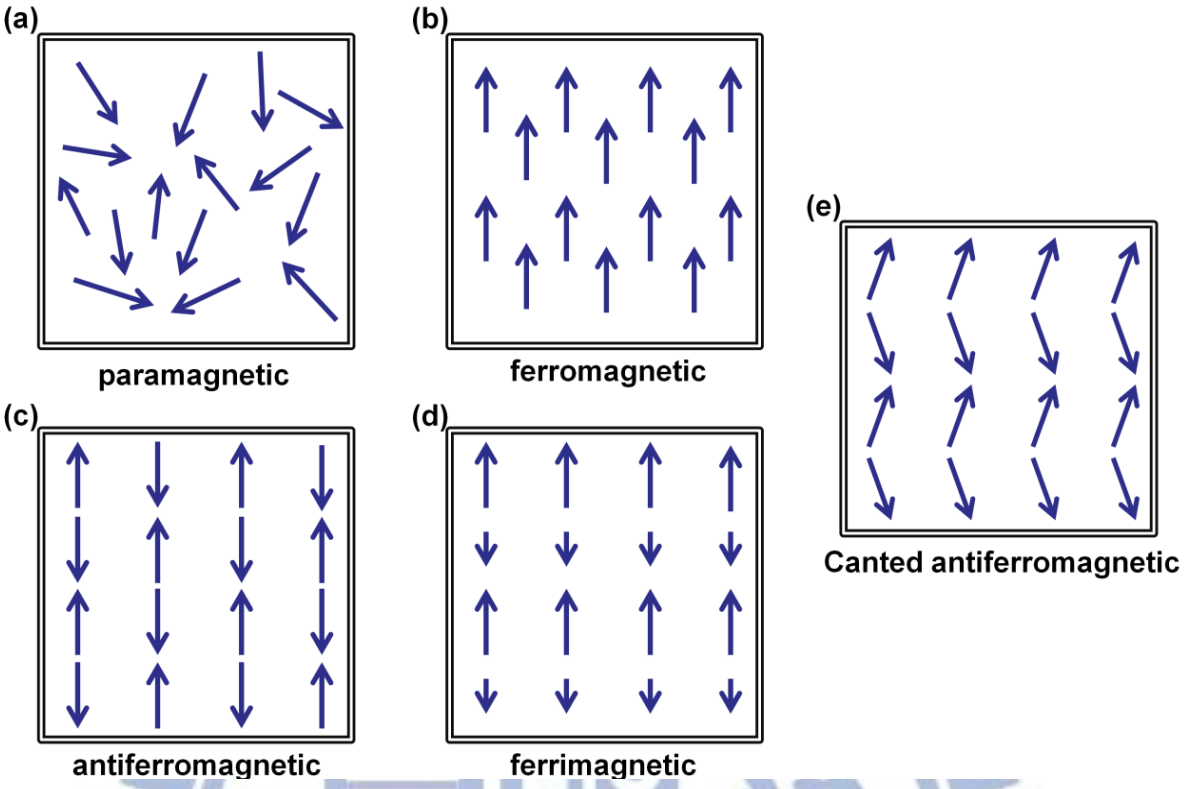

Figure 2.11 *Schematic illustration of five basic types of magnetic orders [69].*

Except for the ferromagnetism, there are still four types of magnetic ordering: paramagnetism, antiferromagnetism, ferrimagnetism and canted anti-ferromagnetism, as shown in **Figure 2.11**. The paramagnetic materials also have the permanent magnetic moments which randomly distribute and bring out the null net magnetization in the absence of magnetic field. When a field is applied, these moments will be slightly inclined to the direction of the applied field. After releasing the field, these moments will go back to the state of randomly distributed as a result of thermal energy. Therefore, the paramagnetic sate can be viewed as high temperature phase of the ferromagnets undergoing the phase transition above Curie temperature [69].

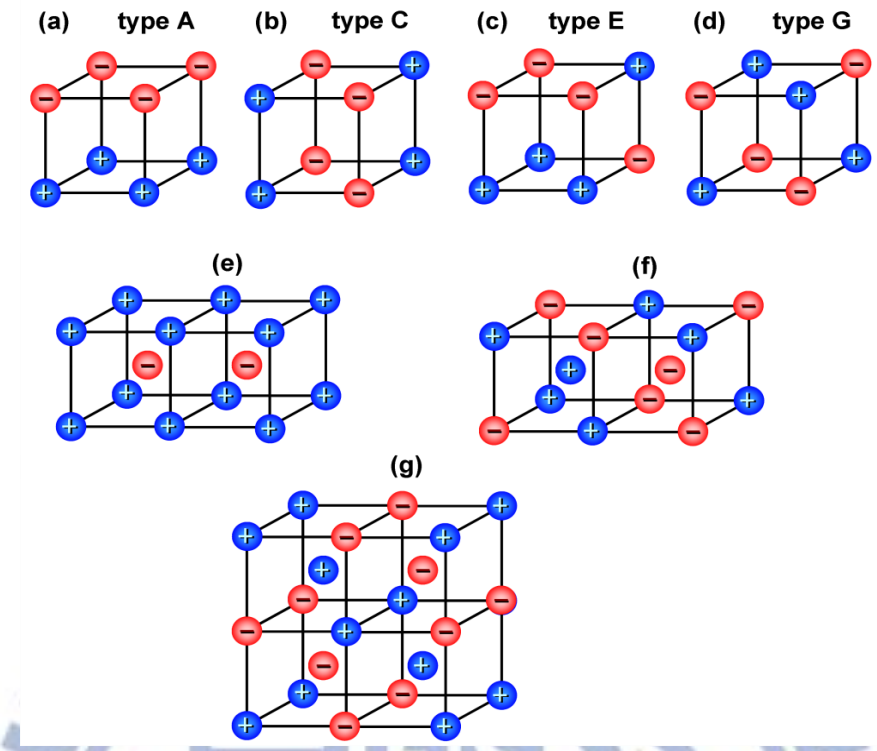

Figure 2.12 ***a)-d)*** *are four types of antiferromagnetic order which can occur on simple cubic lattices; and* ***e)-f)*** *are those can occur on body-center cubic lattices. The two possible spin states are marked + and –[69].*

However, not all paramagnetics are transformed from ferromagnets. Another kind of magnetic ordering calls *antiferromagnetism* would also undergo the phase transition from the ordering of anti-parallel magnetic moments to randomly distributed magnetic moments, and that phase transition temperature is called Néel temperature. In antiferromagnetic materials each unpaired electron spin is aligned anti-parallel with that of neighboring electron to make the magnetization inside the bulk neutralize so that the overall magnetization is zero. According to the different crystal lattices there are also different possible arrangement presented in **Figure 2.12**. For example, G-type ordering is very common in cubic perovskites such as $LaFeO_3$ and $LaCrO_3$ because superexchange interactions through oxygen atoms force all nearest-neighbor magnetic moments to be antiferromagnetically aligned. Sometimes, these magnetic moments of sublattice are not equal or canted away from anti-parallel alignment in antiferromagnetics which is known as *ferrimagnetism* or *canted anti-ferromagnetism* (*weak ferromagnetism*) as shown in **Figure 2.11**, respectively, and hence contribute to net magnetization. The moment in antiferromagnetic materials tend to periodically order in such a way that there is no overall magnetization of the system. In both ferromagnets and antiferromagnets the tendency of the exchange interactions to order the moments is

counteracted by thermal fluctuations; in the limit of zero temperature, the thermal agitations which destroy the ordering vanish, and the degree of order is limited only by quantum effects.

In a electronic band structure and sometimes also the ions in the crystalline lattice, carry a microscopic magnetic moment. For the electrons case, due to the spin angular momentum, there is a very important difference in character between these moment-carriers. The atoms, and their moments, are localized at the crystal lattice points. The electronic band structure, however, propagate through the crystal as Bloch waves, and are regarded as delocalized. Consequently, it is necessary to consider a density of their spins, which is a continuously varying function of positions. In a non-magnetic material, no evidence about long-range ordering of the microscopic magnetic moments over sufficiently large distances, however, the orientation of the localized moments on the atoms varies randomly, and the departures from the band-electron's average spin density of zero are uncorrelated leading the magnetization M (the average moment per unit volume) is zero in both cases. When an external magnetic field H was applied, there are two effects need to consider: first, slightly rotate the microscopic magnetic moments toward the same direction with the field, second one is to induce anti-aligned moments due to the orbital response of the electrons. When the microscopic magnetic moments are aligned with the magnetic field, the material is *paramagnetic*; whereas, anti-alignment leads to *diamagnetism*. In both cases, the external field induces a magnetization, $M = \hat{A}H$; where $\hat{A}$ is the magnetic susceptibility of the material and is positive for paramagnets, negative for diamagnets. In both the above mentioned cases, the magnetization becomes zero when the field is turned off, and the system returning to a state, where the spin orientation is random.

There exists a long-range ordering of the microscopic moments in a magnetic material resulting from spontaneously polarized moments. This interaction between the moments is referred as *exchange interactions*. The magnetic materials exhibiting spontaneous order, can be categorized into ferromagnets and antiferromagnets.

The exchange interactions are responsible in aligning the moments in one direction, in ferromagnetic materials leading to microscopically a non-zero magnetization. The so-called easy axis (the preferred direction of alignment of the moments) is determined by coupling between the moments and the crystal field (e.g. spin-orbit coupling) [70].

2.4.2 Ferromagnetism

In a ferromagnetic material, the exchange interactions produce the spontaneous magnetization. This magnetization is not necessarily to be uniform across the specimen. A ferromagnet may be divided into macroscopic volumes called domains, that are randomly aligned with another but each possessing single oriented magnetic moment, so that the net of magnetization in the absence of external magnetic field is zero. When an external magnetic field was applied, an *expansion* of the domains with moments aligning with the field at the expense of those oriented in other directions. This maximum magnetization is referred to as the saturation magnetization (*M*s) of the material. Due to the dominance of thermal fluctuations over exchange interaction, the spontaneous magnetization of a ferromagnet disappears above a certain critical temperature, the Curie temperature (T_{Curie}). In general, we see a phase transition from ferromagnetic phase to paramagnetic phase above the Curie temperature (T_{Curie}), but some of the materials, like certain rare-earth elements, exhibit anti ferromagnetic ordering at temperatures higher than T_{Curie} [71]. One good example of a second order phase transition is the phase change of a ferromagnetic material to a paramagnetic material (the *normal* phase) with increasing temperature, above the T_{Curie} [72]. This has been confirmed by theoretical calculations studies which predict the onset of ferromagnetic ordering only at extremely low densities, however, much disagreement about the precise density range, and the physics of these low density regimes should be regarded with caution [73]. More detailed models of itinerant electron systems have been more successful than the homogeneous electron gas approximation. These models have demonstrated that a main important role to determine the band structure whether or not that itinerant electron ferromagnetism will appear in a material. Of particular note is the so-called Slater and Stoner models [74, 75], which gives a criterion for the appearance of ferromagnetism in terms of the density of states (DOS) at the Fermi level. His model also gives a very basic phenomenological detail of an itinerant system, and considerable improvement has been made upon it [71, 76]. Nevertheless, it has provided a powerful round to investigate the itinerant electron ferromagnetism materials.

2.5 Colossal magnetoresistance

In this section a brief introduction to the history and origin of the colossal magnetoresistive (CMR) materials is presented. In the following subsections, the early

theoretical models to explain the CMR effect will briefly be presented. Other theoretical models are discussed in the later chapters.

2.5.1 The early days of manganites

In the first study, it is widely recognized that results for manganites were presented in 1950 by Jonker and Van Santen [77]. In that one, La was substituted/doped/replaced either by Ca, Sr, or Ba, and results for polycrystalline samples of (La,Ca)MnO_3, (La,Sr)MnO_3, and (La,Ba)MnO_3. The important result was the appearance of ferromagnetism in these compounds, as described and clarified in their publication that the term "manganites" is not rigorous, and mentioned that *"For the sake of simplicity the compounds containing trivalent, as well as those containing tetravalent, manganese will be designated as manganites"*, a convention that it is followed till today. In addition, they found that the manganites based on their studies about crystallize in ABO_3 perovskite structure, as shown in **Figure 2.13**.

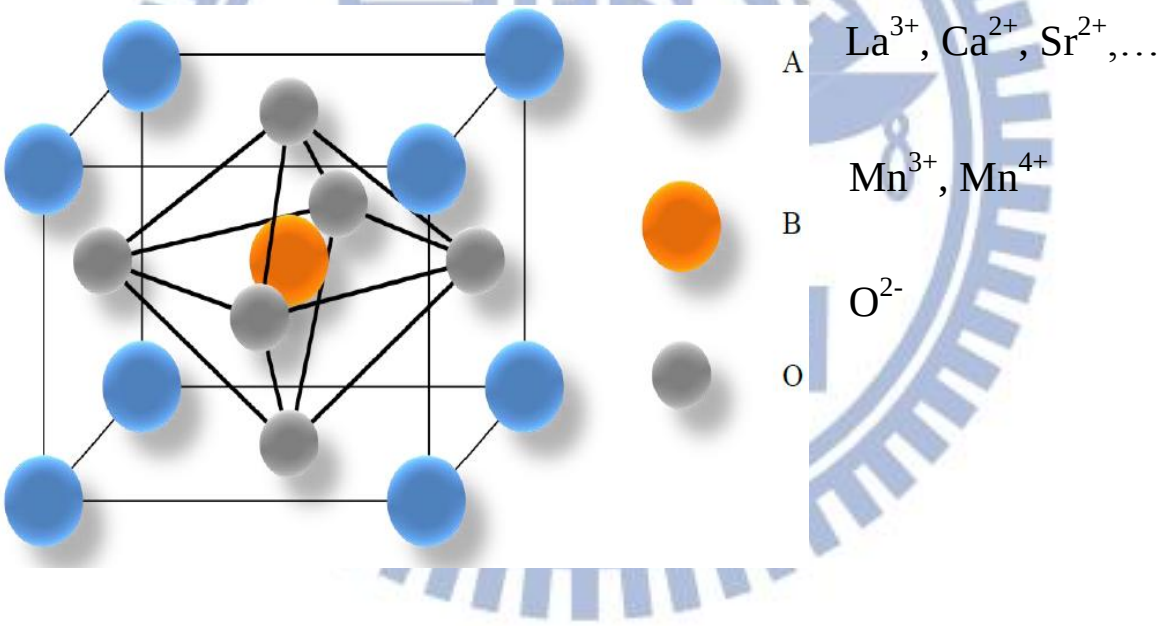

Figure 2.13*: Schematic view of the cubic perovskite structure*

Where A-site of the structure contains a large Rare earth or Alkaline earth ion, such as La, Pr, Ca, Sr, etc., with typical ionic sizes, Ca^{2+} = 0.106 nm Sr^{2+} = 0.127 nm, Ba^{2+} = 0.143 nm, and La^{3+} = 0.122 nm while small ions, such as Mn^{3+}, Mn^{4+}, (Mn^{3+} = 0.07 nm and Mn^{4+} = 0.052) [77] are occupied at the B-sites. The oxygens (O^{2-} = 0.132) surrounding the B-site form an octahedral cage. Manganese is the smallest of all the ions present in the manganite compound. The Curie temperature was obtained by Jonker and Van Santen [77] using

magnetization measurements, and the early samples of manganites contained an excess of oxygen, and the results they obtained are not accurate compared with the modern versions of the (La,Ca)MnO_3 phase diagram, as will be shown later.

In those early studies, the ferromagnetic phase is mostly like a positive *indirect-exchange* interaction. Recently, it should be more likely the *double–exchange* (DE) picture rather than the *indirect-exchange*, which would be discussed later. In the early studies of manganese oxides, it was also noticed that (La,Sr)MnO_3 can only admit up to 70% molar ratio of Sr. Otherwise, there is a two-phase compound which can be obtained for geometrical reasons referred to the tolerance factor, we called as Γ. This factor plays an important role in Mn oxides, where $\Gamma = \frac{r_A + r_O}{\sqrt{2}(r_B + r_O)}$. The perovskite structure is stable in between $0.89 \prec \Gamma < 1.02$, and $\Gamma = 1$ corresponding to the perfect cubic close packed structure. Generally, value of Γ differs appreciably from 1 and the manganites have at least at low temperature, the structure should be a lower rhombohedral symmetry or orthorhombic structure.

After that, a few months after the original publication, Van Santen and Jonker [78], the conductivity of manganites was reported. Anomalies in the conductivity were found at the Curie temperatures. The study of the lattice parameters as a function of hole doping was reported in those early days by Jonker [79], observing that near the composition of 100% La the crystal is distorted, while at higher Sr or Ca densities, it is not. These distortions are associated with the Jahn–Teller effect, which is very important in manganites, as will be shown later. A few years after the original work of Jonker and Van Santen [79], the magnetoresistance data on manganites, the author wrote *"Manganites, when in the ferromagnetic state, show a notable decrease of resistivity in magnetic fields"*[80].

It was already noticed in those early studies that standard explanations for the effect did not work, and that the effect was likely related to the favoring of the ferromagnetic state by a magnetic field. However, one should note that the truly enormous magnetoresistance, the now it is well - known as *"colossal"* effect, was discovered much later, in the 1990s.

2.5.2 Ferromagnetism in $La_{2/3}Ca_{1/3}MnO_3$

In **Figure 2.14**, the phase diagram of $La_{2/3}Ca_{1/3}MnO_3$, as reported by Cheong and Hwang, is shown [81]. $LaMnO_3$ and $CaMnO_3$ are both antiferromagnetic insulators. At a mixturing of $LaMnO_3$ and $CaMnO_3$ is expected to show no spectacular effect. But, in their

ferromagnetism phase diagram it is found that half metal transition and several regions with spin and charge orderings are bound. An important aspect in the unexpectedly rich phase diagram of LCMO is the small but relevant distinction in crystal structure, although both compounds are perovskites. $LaMnO_3$ consists of deformed MnO_6 octahedra, whereas the octahedral are perfect in $CaMnO_3$. Above 10% Ca doping results in suppression of the antiferromagnetic coupling and a ferromagnetic ground state is obtained. In the region with 20% to 50% Ca doping concentration is a ferromagnetic metal, dominated by double exchange that will be introduced in next section. According to LCMO phase diagram by Cheong [81], as shown in **Figure 2.14**, the ferromagnetic metallic phase emerges instantly above a critical concentration, at all temperatures below T_{Curie}.

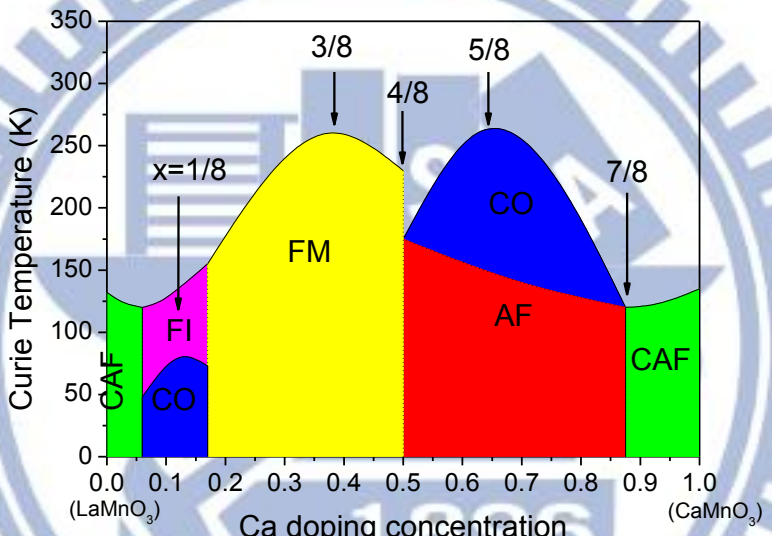

Figure 2.14: *The phase diagram of $La_{1-x}Ca_xMnO_3$, after Cheong and Hwang [81]. There exist well-defind anomalies at $x=\frac{n}{8}$, (n =1,3,5 and 7). FM : Ferromagnetic Metal, FI: Ferromagnetic Insulator, AF: Antiferromagnetism, CAF: Canted Ferromagnetism, and CO: Charge/orbital Ordering, re-drawn from Ref.[82].*

2.5.3 The early theoretical models

As we have known that, in the 1950s, the theoretical studies of manganites had widely studied on the origin of the ferromagnetic phase. The starting point was that when the *colossal* magnetoresistance effects were found that promised the potential applications for next generations of electronic devices. In the following, the basic theoretical description for the manganites namely double–exchange and Jahn–Teller effect will be presented.

2.5.3.1 Double–exchange (DE)

In 1951, Zener presented the basis for understanding the origin of ferromagnetic phase in CMR type materials. After that in a couple of papers [83–84], where mainly qualitative statements and analyses of experiments were also presented and Zener's work has been widely regarded as providing a proper explanation for ferromagnetism in manganites. Zener predicted ferromagnetism as arising from an indirect coupling between incomplete d-shells, via conducting electrons. It is sufficient to consider a qualitative description of the splitting of the five d-levels in the presence of a 3d orbital crystal environment, as shown in **Figure 2.15a)**. The Hund's rule for each individual ion or atom enforces a ferromagnetic Hund's coupling J_H. This effect was argued by Zener to play an important role in this mechanism, enforcing the configuration, where the unpaired spins are aligned to the lowest energy. Because the conduction electrons do not change their spin when they move from ion to other ion, the electron interaction or coupling will maintain the z-projection of the spin, Zener gave a reasonable explaination that those electrons are able to move in the crystal in the optimal manner when the net spin of the incomplete d-shells are all parallel. Otherwise, an up electron can land on a down spin ion, and spend an energy proportional to the Hund's coupling. In the other hand, the conduction electrons have lower their kinetic energy if the background of d-shell spins, or the t_{2g} spins of manganite, is fully polarized. The kinetic energy is regulated by a hopping amplitude noted as *t* factor. The d-shell spins are indirectly coupled via an interaction activated by the conduction electrons. Zener clearly remarked in his papers that a direct coupling between d-shells (not mediated by conduction electrons, but by the direct virtual hopping of d-electrons) is of opposite sign leading to antiferromagnetism, rather than to ferromagnetism. The coupling involved in this direct exchange process is called J_{AF}, and it will be shown to be important in the physics of manganites. So, Zener proposed as *"double exchange"*. This mechanism is sketched in **Figure 2.15b)**. It can be explained as a *simultaneous* transfer of an electron from the oxygen to the Mn on right side, and from the Mn on left to the oxygen, such that the net transfer is of an electron from Mn on left to Mn on right. This regime leading to ferromagnetism that Zener found should not be confused with that of the *super exchange* model, which also uses an oxygen as a bridge between ions. He presented that in the super exchange, the interaction leads to an anti-ferromagnetic alignment of spins. Using the double-exchange idea not to explain ferromagnetism but as a tool to

explain the transfer of electrons that was built in the context of the original idea of ferromagnetism mediated by conduction electrons [83]. Zener's work was continued by Anderson (Nobel prize 1977) and Hasegawa [85] and De Gennes (Nobel prize 1991) [86], who proposed mechanism in detail. They found out that there is a better way to describe the motion of electrons from Mn-to-Mn and electrons transfer is only *one-by-one*, still using the oxygen as a bridge between ions, rather than simultaneously as believed by Zener. Any perturbation approach for the hopping amplitude t of electrons will naturally lead to a one-by-one transfer. Perhaps the most often-quoted portion of the work of Anderson and Hasegawa [85] is the effective hopping term t_{eff} of an electron jumping between two nearest-neighbor Mn ions. In fact, the calculation shows that $t_{eff} = t\cos\frac{\theta}{2}$, where θ is the angle between t_{2g} spins located at the two sites involved in the electron transfer, as shown in **Figure 2.15c)**.

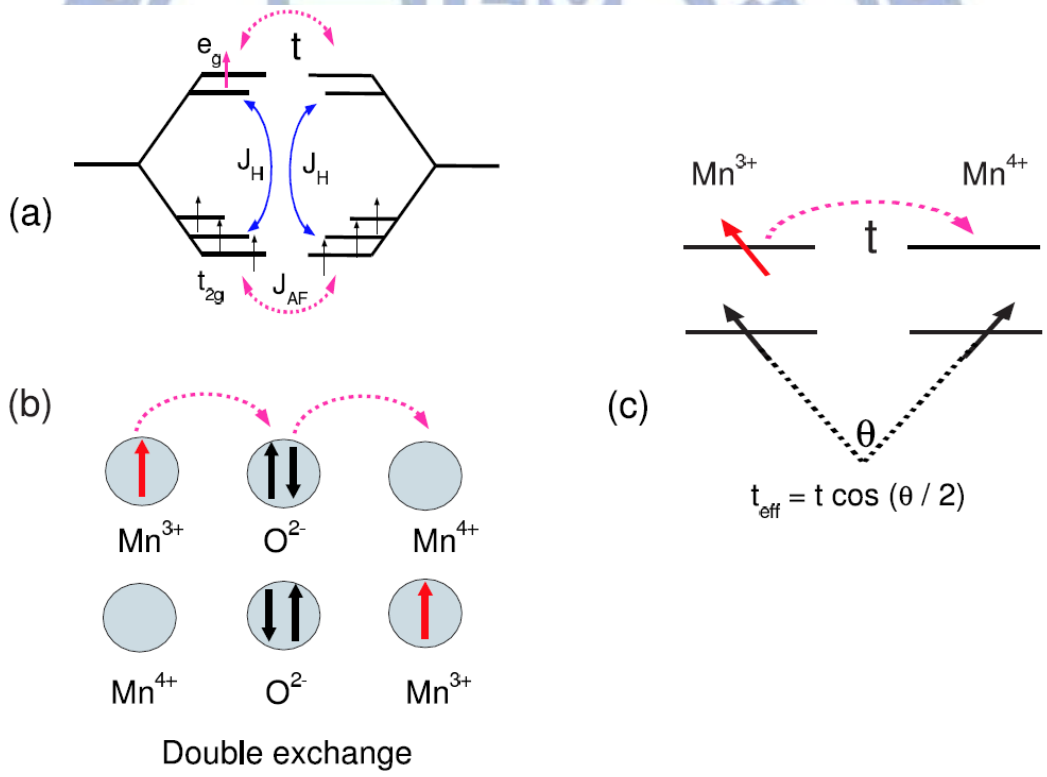

Figure 2.15: **a)** *Schematic representation of the ideas of Zener to explain ferromagnetism. Zener envisioned a system with both localized and mobile electrons, which in the manganite language are the t_{2g} and eg electrons, as indicated.* **b)** *Schematic view of the DE mechanism.* **c)** *The effective hopping t_{eff} mechanism is drawn schematically [82].*

2.5.3.2 Jahn–Teller effect

For an isolated 3*d* ion, five degenerated orbital states are available corresponding to the 3*d* electrons with $l = 2$. In a crystal, the degeneracy is partially lifted by the crystal field. The five *d*- orbitals are split by a cubic crystal field into three t_{2g} orbitals and two e_g orbitals. For the MnO_6 octahedron, the splitting between the lowest t_{2g} level and the highest e_g level is $\Delta = 1.5\,\text{eV}$ (**Figure 2.16**). For the ratio of Mn^{3+} and Mn^{4+} ions, the inter atomic correlations ensure parallel alignment of the electron spins (first Hund's rule); the corresponding exchange energy (This energy will be called later as J_{spin}) is estimated about 3 eV [87]. Although the energy of Mn^{4+} remains unchanged by such a distortion, the Mn^{3+} has lowered energy. Thus, Mn^{3+} has a marked tendency to distort its octahedral environment in contrast to Mn^{4+}. This effect is known as *Jahn-Teller* distortion and it is rather effective in the lightly doped manganites, i.e. with a large concentration, (1 - x), of Mn^{3+} ions. This is illustrated by the structure of $LaMnO_3$ (**Figure 2.16**) in which the MnO_6 octahedra are strongly elongated within the ab-plane in a regular way leading to a doubling of the unit cell. With increasing the Mn^{3+} content, the Jahn-Teller distortions are reduced and the stabilization of the $(3z^2 - r^2)$ e_g–orbital becomes less effective. Nevertheless, in a large number of manganites, the e_g–orbitals of two types, $\left(3z^2 - r^2\right)$ and $\left(x^2 - y^2\right)$ are not occupied by the e_g electrons of Mn^{3+} at random and an orbital order is achieved.

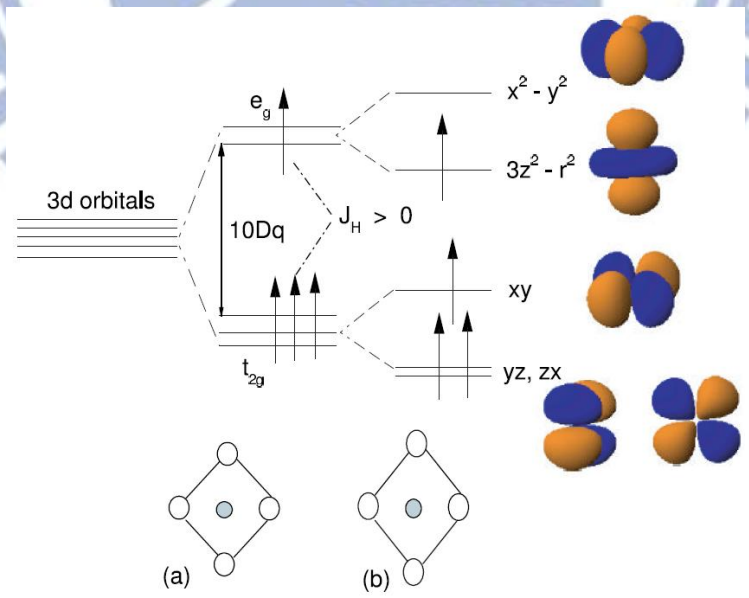

Figure 2.16 *Energy level diagram and 3d orbital eigenstates of Mn^{3+} in a crystal field of cubic and tetragonal symmetry [82].*

2.5.4 Transport and CMR effect

Figure 2.17 shows the typical resistance behavior of Ca-doped CMR material. We measured resistance as a function of temperature for a thin film of 1/3 -Ca doped in $La_{1-x}Ca_xMnO_3$ with thickness about 200nm, where the magnetic field was applied in-plane. The results show clearly that, the resistance is decreased but the Curie temperature is increasing, indicating more of the insulator –like behavior under application of the magnetic field.

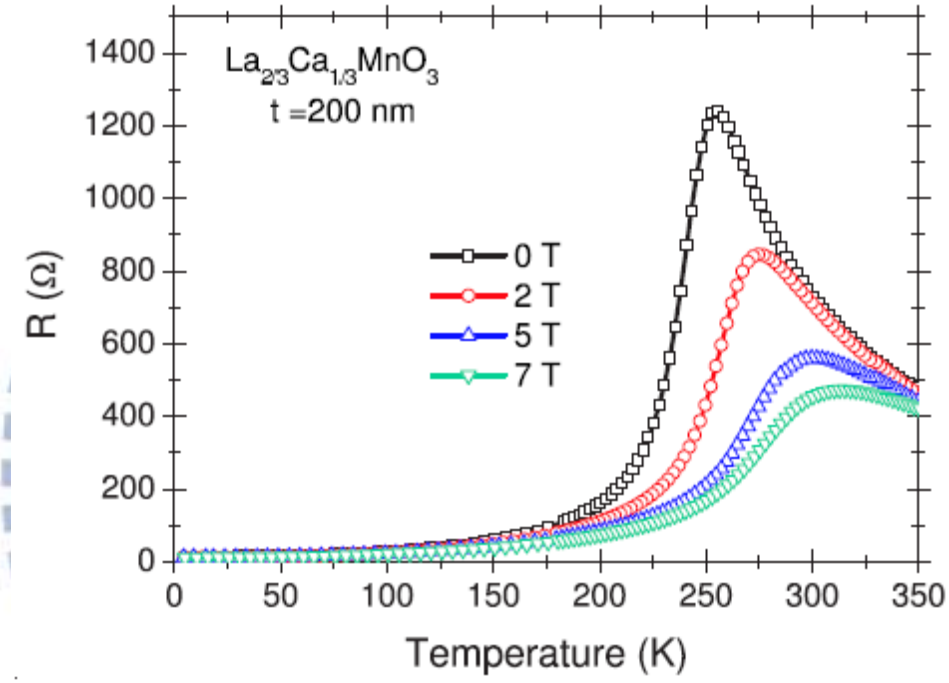

Figure 2.17 *Low temperature resistance for a LCMO thin film with thickness of t = 200 nm under different magnetic fields (in – plane)[88].*

A defining moment for the field of manganites was the publication by Jin *et al.* [88]. Those authors studied films of LCMO and defined the magnetoresistance (MR) ratio as $\frac{\Delta R}{R} = \frac{R_H - R_0}{R_0}$, where R_0 and R_H are the resistances without and with external magnetic field, respectively. They reported MR ratio values much higher than previously observed by other authors [89, 90]. Therefore, the term Colossal Magnetoresistance (CMR) was coined. This new term is a superlative of Giant Magnetoresistance, which was observed in ferromagnetic and nonmagnetic superlattices by switching an external magnetic field.

2.5.5 Others CMR models

After the early studies of manganites described before, Tokura [91] proposed that the charge-ordering (CO) states observed by Wollan and Koehler [92], and Jirák *et al.* [93] are very important to explain the CMR effects, see the phase diagram in **Figure1.15**. They presented results that indicating an immediately collapse of the changing from charge-ordered state into a ferromagnetic state (FM) in the magnetic field. The competition between CO and FM is indeed a key component of the current theories of manganites aiming to explain the CMR phenomenon. It is clear from the experiments and the theory that the CO-FM transition should be first-order unless disordering effects smear it into a rapid but continuous transition. The huge CMR effect in some compounds at very low temperatures, such as that presented in **Figure1.17**, appears to be caused by the CO/FM first-order transition induced by magnetic fields. All the early theoretical studies of manganites in the 1950s and 1960s did not explain this physics, which were based on the so-called double-exchange effects and one-orbital models. Only in the late 1990s and early 2000s Tokura [91] suggested that the CO/FM competition model and the phase separated model proposed by Dagotto [94] have been identified as the key of the CMR phenomenon.

2.5.6 Spin-polarization

A fundamental interest for both basic physics and potential applications for the next generations of electronic devices is the degree of spin-polarization *P* at the fermi energy. The band-structure of ferromagnets is spin dependent and two subbands are found for majority (carrier spin directed parallel to the magnetization) and minority (spin antiparallel to the magnetization) carriers, respectively [95]. The schematic density of states for a strong and a half-metallic ferromagnet (e.g. ferromagnetic manganites) are shown in **Figure 2.18 a)** and **(b),** respectively.

For ferromagnetism materials ($La_{2/3}Sr_{1/3}MnO_3$ or $La_{2/3}Ca_{1/3}MnO_3$ as an example), the spin-polarization is often defined as the normalized difference of the majority $(n\uparrow)$ and minority $(n\downarrow)$ density of states at the Fermi level, given by the following formula:

$$P_n = \frac{n\uparrow - n\downarrow}{n\uparrow + n\downarrow} \qquad \textbf{(2.6)}$$

This definition is absolutely related to the definition of the net magnetization by the integrating as the difference between the integrated majority and minority carrier density as a function of energy,

$$M = \mu_B \int (n\uparrow - n\downarrow) dE \qquad \textbf{(2.7)}$$

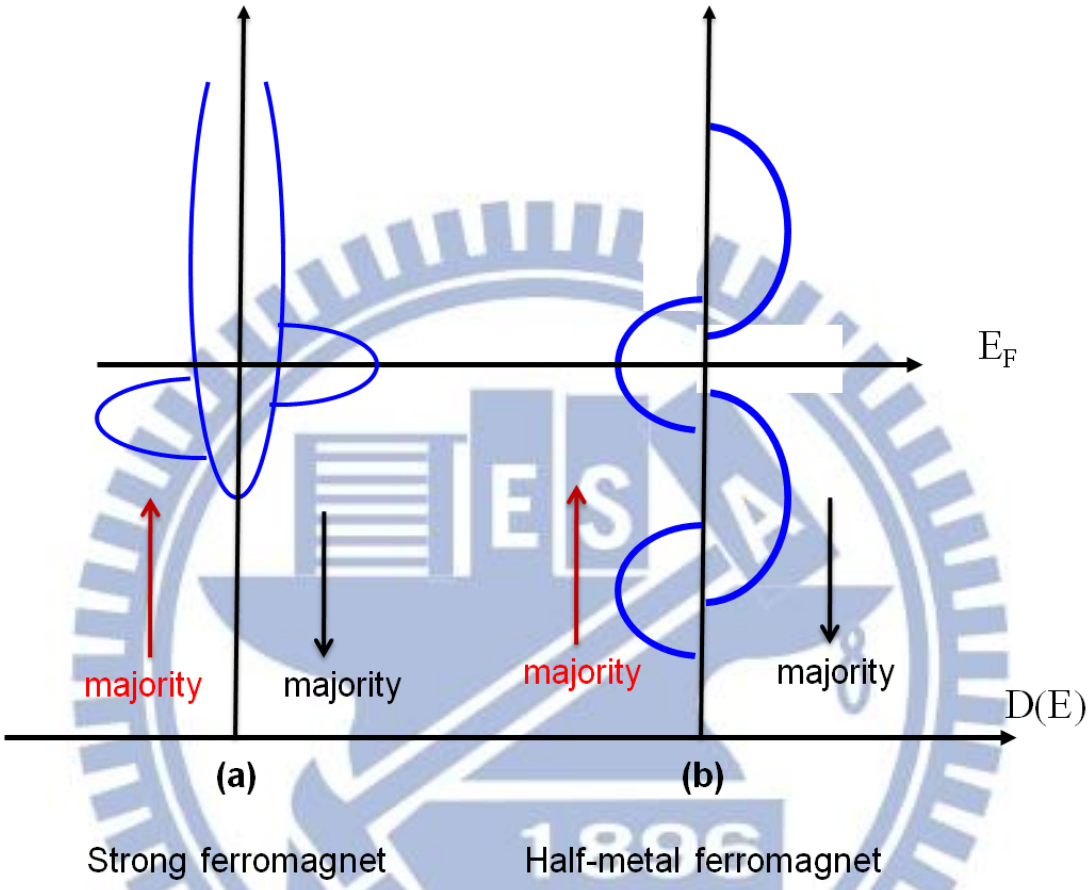

Figure 2.18 *The spin polarization:* **a)** *Schematic density of states of a strong ferromagnet and* **b)** *half-metallic ferromagnet, re-drawn from Ref.[82].*

And we can see that $P(T) \propto M(T)$ is expected. The definition of spin-polarization in this way might be probed by spin-polarized photoemission with left handed and right handed circular polarization. However, the results were pointed out by Mazin [96], showing that the definition of spin-polarization is by no means unique. Often transport properties are very interest, especially for the spintronic applications. In a ferromagnet the majority and minority carriers can be regarded as two parallel transport channels as proposed theoretically by Mott (Nobel prize 1977) [97], Campbell and Fert [98], and experimentally by Meservey and Tedrow [99]. The definition of the spin-polarization in terms of the majority $(J\uparrow)$ and minority $(J\downarrow)$ current densities seems more appropriate. Within classical Boltzmann

transport theory, $J_{\uparrow\downarrow} \propto \langle n\vartheta \rangle_{\uparrow(\downarrow)} \Im_{\uparrow(\downarrow)}$, where <…> denotes a Fermi surface average and $\Im_{\uparrow(\downarrow)}$ the relaxation times for majority and minority carriers, respectively. Assuming a spin-independent relaxation time, one finds

$$P_J = \frac{J\uparrow - J\downarrow}{J\uparrow + J\downarrow} = \frac{\langle n\vartheta^2 \rangle_\uparrow - \langle n\vartheta^2 \rangle_\downarrow}{\langle n\vartheta^2 \rangle_\uparrow + \langle n\vartheta^2 \rangle_\downarrow} \qquad \textbf{(2.8)}$$

The spin-polarization defined by the majority and minority currents can be simply related to the majority $(\rho\uparrow)$ resistivity and minority $(\rho\downarrow)$ resistivity, respectively:

$$P_\rho = \frac{\rho\uparrow - \rho\downarrow}{\rho\uparrow + \rho\downarrow} \qquad \textbf{(2.9)}$$

The majority and minority resistivities can be determined and measured at low temperature from deviations of Matthiessen's rule. These values of resistance depend on the impurities present in the metal and consequently the spin-polarization can be tuned by alloying. The experiments capable of determining the transport spin-polarization are spin polarized tunneling between ferromagnetic contacts and the dynamic conductance of superconductor/ferromagnet (SC/FM) contacts. Mazin [96] analyzed the transport through a SC/FM contact. In the case of ballistic transport without a barrier, the current through the contact is proportional to $\langle n\vartheta \rangle$; thus, the ballistic spin-polarization is given by

$$P_\vartheta = \frac{\langle n\vartheta \rangle_\uparrow - \langle n\vartheta \rangle_\downarrow}{\langle n\vartheta \rangle_\uparrow + \langle n\vartheta \rangle_\downarrow} \qquad \textbf{(2.10)}$$

and does not agree with the spin-polarization in **Equation 2.8** defined via current densities. If a specular barrier is present, the tunneling current depends on the Fermi velocity or even barrier transparency or, in a more complex way, it depends on both of them, and the measured spin-polarization does not agree with any of the definitions introduced so far. This analysis shows that experimental values obtained with different techniques relate to different definitions of the spin-polarization that need not necessarily agree.

2.6 Basic Physical Properties of $YBa_2Cu_3O_y$

2.6.1 Crystal structure

In the last twenty years, following the discovery of superconductivity in $La_{2-x}Ba_xCuO_4$ by Bednorz and M¨uller [100], a large number of related compounds with high superconducting transition temperatures have been found. The basic understanding of these

high-temperature superconductors (HTSC's) is a crystal structure containing CuO_2 planes separated by block layers. These block CuO_2 layers play a role of a charge reservoir. Electrons can be withdrawn from the CuO_2 planes by replacing or adding ions. In addition, for the $YBa_2Cu_3O_y$ (YBCO) case, doping can be controlled by interexchance oxygen content in the CuO chain with the CuO_2 planes. Usually the block layers are insulating and have almost no contributions to the low energy physics. On the other hand, the CuO_2 planes have energy states around the Fermi level (E_F) and thus dominate the low energy physics. Therefore, the CuO_2 planes should be essential to HTSC's and are believed to be the main contribution to the superconducting state of YBCO. The crystal structure and the Brillouin zone of YBCO is shown in **Figure 2.19a)**. The basic structures can be distinguished between YBCO and other high-*T*c cuprates is existed in one dimensional CuO chain aligned along *b*-axis. Therefore, in studying the electronic structure of YBCO, one should sort out the features related to the CuO chain and the influence of the chains on the electronic structure of the CuO_2 planes. Because of the presence of CuO chain in the structure, YBCO does not have a square lattice but rather an orthorhombic structure. According to the band calculations [101], this orthorhombic structure causes a significant anisotropy of the in-plane electronic structure.

a)

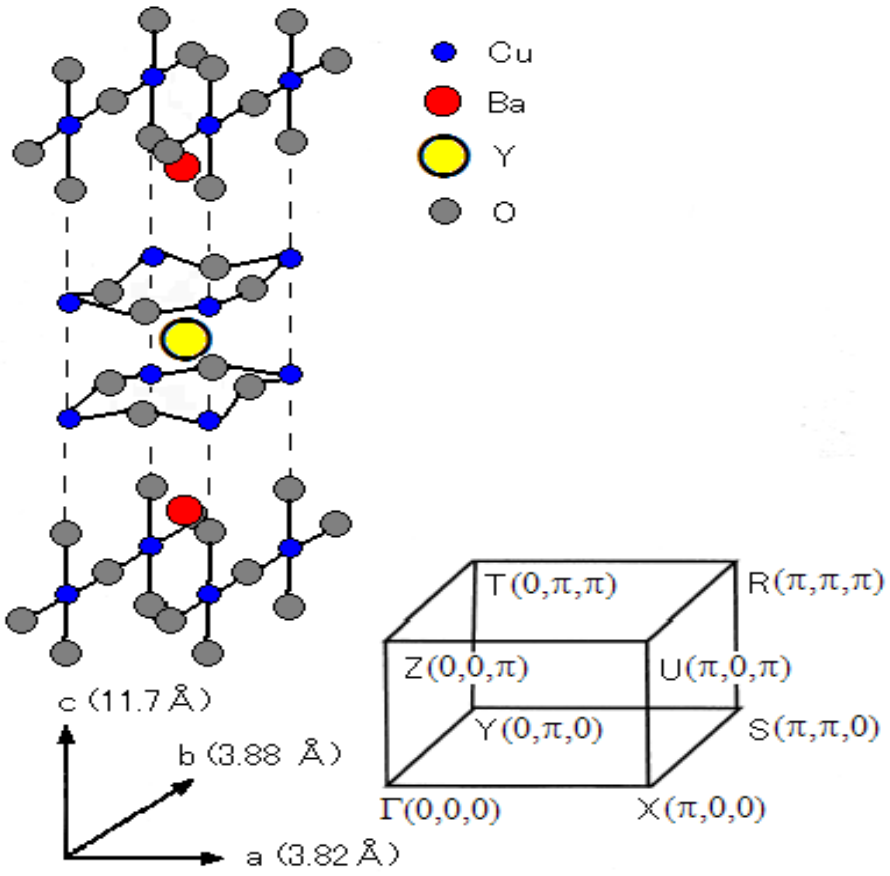

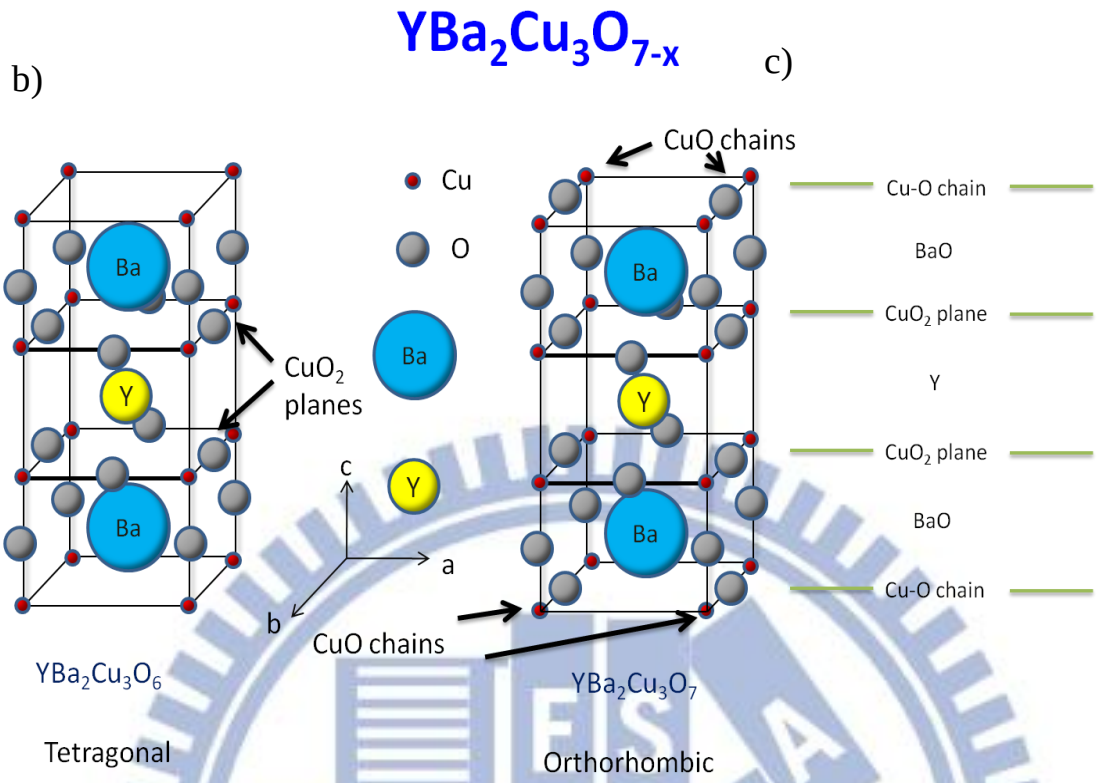

Figure 2.19 a) *The crystal structure and the Brillouin zone of YBCO;* **b)** *Tetragonal structure of YBCO and* **c)** *Orthorhombic of YBCO [102]*

2.6.2 Phase diagram

In YBCO, as the oxygen content ,*y,* increases from 6 to 7, the CuO chain oxygen sites are occupied and holes are doped into the CuO_2 planes in which is the key point to decide the structures and physical properties of YBCO as shown in **Figure 2.19**. As we can see the only difference between these two structures of YBCO is only the oxygen contents in the structure, especially in the Cu-O chain. In **Figure 2.20b)**, there is no oxygen in the Cu- chain, therefore it is tetragonal structure and insulating YBCO. However, when the oxygen is filled in the Cu-O chain, the structure is changing from Tetragonal to Orthorhombic structures and YBCO becomes superconducting as shown in **Figure 2.19c)**. Here again, **Figure 2.20 a)-c)** shows the phase diagram of YBCO [102,103]. In **Figure 2.20b)** the actual measured values of critical temperature Tc are plotted against the p values obtained by using the equation: $1-\frac{T_c}{T_{cmax}}=82.6(p-0.16)^2$ where T_{cmax} is about 93K for YBCO case or we also can determine by $p=11.491y+5.17\times10^9 y^6$ where y =1-c/c_0 and c_0 =1.18447nm at 22^0C is the

c-axis lattice parameter at zero doping region. **Figure 2.20c)** shows the superconducting transition temperature, Tc, of YBCO as a function of oxygen content. This curve, with a tendency toward a plateau near x = 0.66 and maximum near x=0.9 is well known. The reason for the Tc ~60K quasiplateau between x=0.5 and 0.75 is not yet well understood. Our explaination is that when the oxygen content is increased from x=0.5, where YBCO forms the orthorhombic phase with alternating full (which means that the chain oxygen site is fully occupied) and empty (means the chain oxygen site is empty) chains, additional oxygen ions fill the empty chains and make a relatively small contribution to hole doping. For YBCO, how the in-plane hole concentration changes with increasing oxygen content *y* has been controversial. **Figure 2.20 d)** is the relationship between oxygen content *y* and hole concentration.

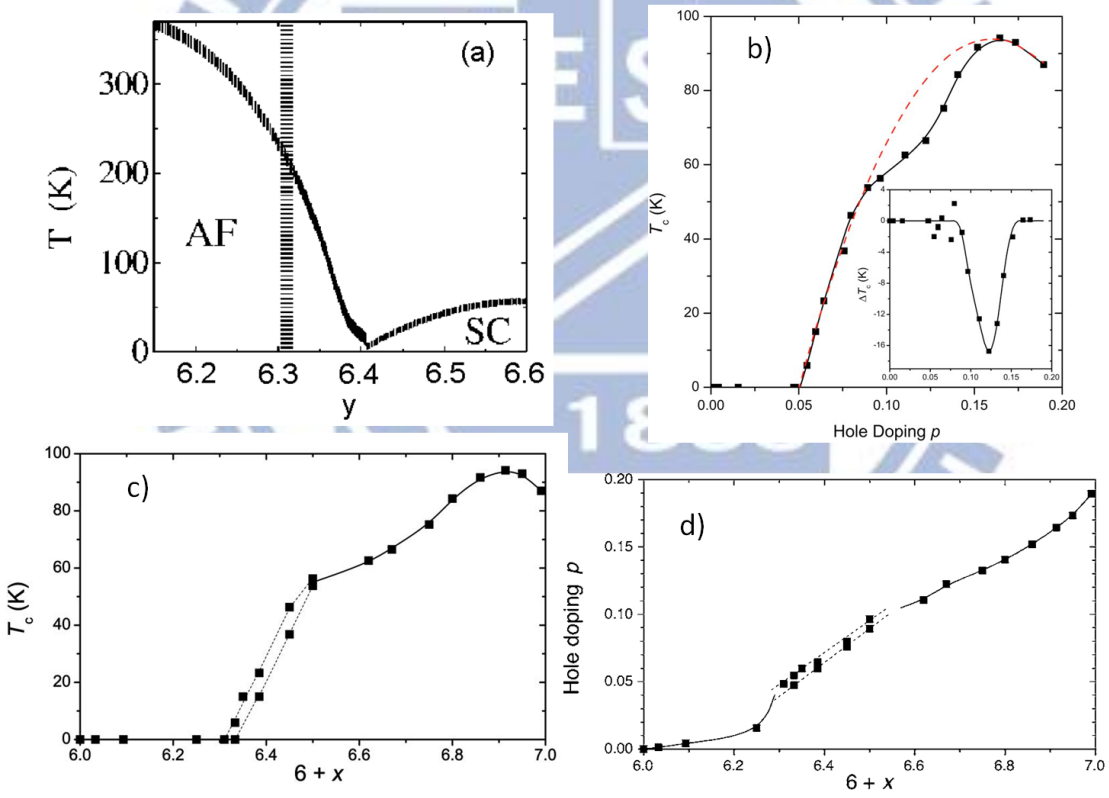

Figure 2.20: a) – c)*: Phase diagram of $YBa_2Cu_3O_y$ [102, 103]. AF: antiferromagnetic insulator. SC: superconductor.* **d)** *Relationship between the oxygen content y and the hole doping in YBCO [104].*

2.6.3 Electronic structure

In the CuO_2 plane, the $d_{x^2-y^2}$ band originated from Cu has the highest energy among the five *d* bands as shown in **Figure 2.21**, because the Cu $d_{x^2-y^2}$ orbital well hybridizes with oxygen *p* orbitals through the in-plane Cu-O bonds which have shorter length than the out-of-plane Cu-O bonds (**Figure 2.20**). Therefore, in the parent insulator with nine *d* electrons (or one *d* hole), the $d_{x^2-y^2}$ band is half-filled and carries 1/2 spin. Since the on-site Coulomb repulsion *U* between $d_{x^2-y^2}$ electrons is stronger than the band width *W* (the kinetic energy of the electrons) in the cuprates, and the electrons tends to avoid the double occupancy of the $d_{x^2-y^2}$ orbital and, at half-filling, the electrons are localized as a Mott insulator. For the CuO_2 plane, the minimum charge excitation energy is not the energy *U* for the electron transfer between the half-filled Cu $3d_{x^2-y^2}$ orbitals, but the energy Δ_{CT} for the charge transfer between the Cu $d_{x^2-y^2}$ band and the O 2*p* bands hybridized with the $d_{x^2-y^2}$ band. The three bands in the CuO_2 plane, $d_{x^2-y^2}$, *px* and *py* , and their energies relative to the chemical potential μ are schematically illustrated in **Figure 2.22a) and c)**, respectively. The Cu $d_{x^2-y^2}$ band is split into the upper and lower Hubbard bands (UHB and LHB) by Coulomb repulsion *U* and the O 2p bands are located between them and separated from UHB by the charge-transfer gap ΔCT , whose magnitude is about $\Delta_{CT} \sim 1.5$ eV for La_2CuO_4 according to the optical conductivity studies [105, 106].

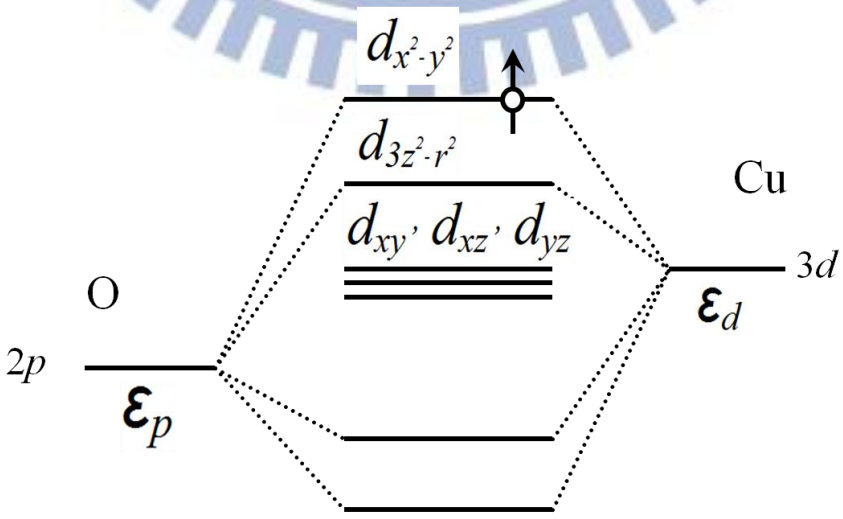

Figure 2.21 *Schematic diagram for the energies of Cu 3d and O 2p orbitals in the cuprates. In La_2CuO_4, for example, the Cu atom is surrounded by an oxygen octahedron elongated along the z-direction [102].*

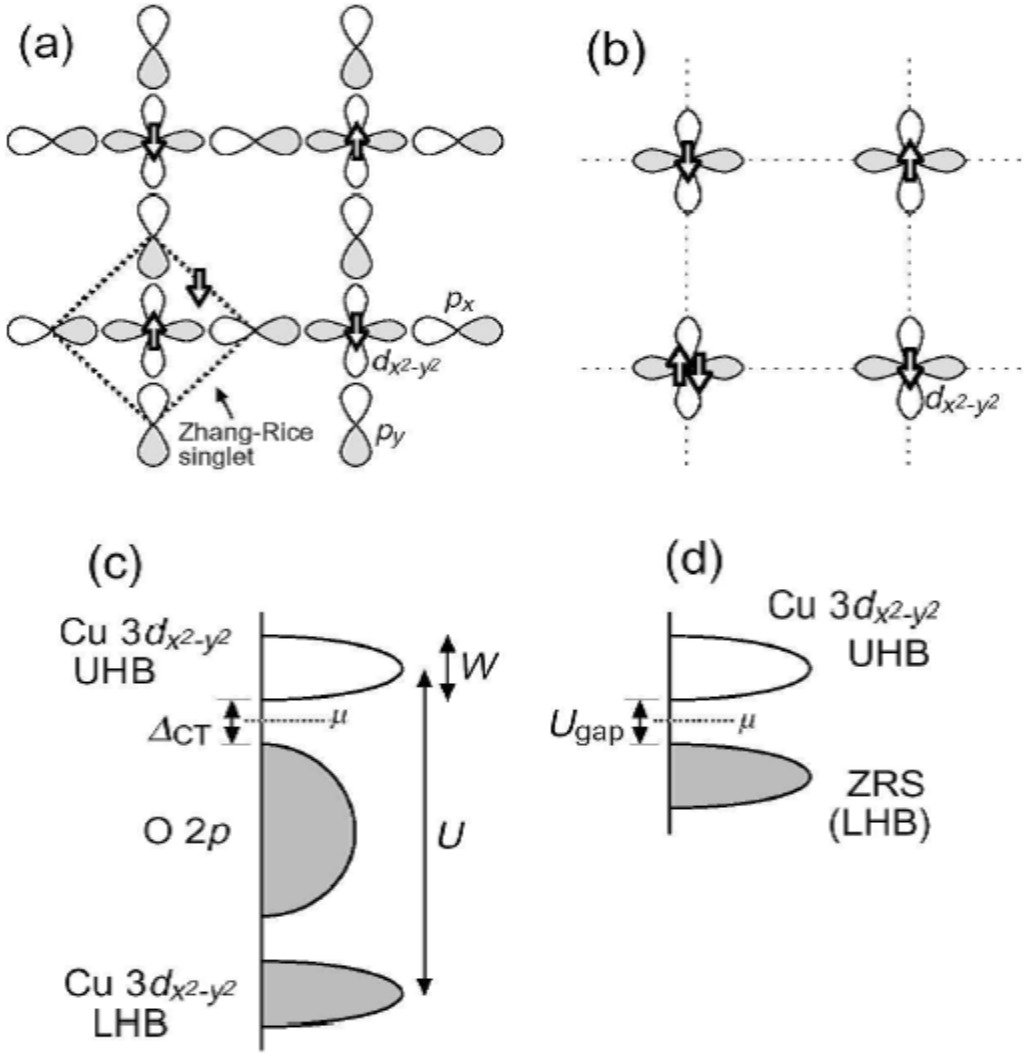

Figure 2.22 *Schematic pictures for the electron orbitals* **a)**, *and* **b**) *the electronic structure* **c)**, **d)** *of the CuO_2 plane. Three bands, Cu 3 $d_{x^2-y^2}$, O 2px and 2py, are considered in* **a)** *and* **c)**. *Only the $d_{x^2-y^2}$ band at the Cu site is considered in* **b)** *and* **d)** [102]**.**

As for the low-energy physics (Δ_{CT}) in the CuO_2 plane, the three-band picture **Figure 2.22a)** and **c)** may be further simplified. Hole doping is introduced into the O 2*p* band in addition to the one *d* hole, a local singlet state called Zhang-Rice singlet (ZRS) has the lowest energy for the *p* hole [107, 108]. As shown in **Figure 2.22a)**, the *p* hole in the ZRS state surrounds the Cu site and carries another 1/2 spin of the direction opposite to the spin of the *d*

hole. Thus one may interpret the UHB and the ZRS band as the effective UHB and LHB split from a band of the $d_{x^2-y^2}$ symmetry at the Cu site by the effective Coulomb repulsion U_{gap} = Δ_{CT} as illustrated in **Figure 2.22b) and d)**. Therefore, most of discussions will be based on the one-band picture

2.6.4 Transport properties

As we know that in high-*T*c cuprates, the transport properties are unusual in terms of standard Fermi-liquid theory. One of the most unusual properties is the temperature dependence of the resistivity. While Fermi-liquid theory predicts the temperature dependence of the resistivity ρ given by $\rho \sim \rho_0 + AT$, a nearly optimally doped y = 6.90 sample shows a robust T -linear dependence, $\rho \sim \rho_0 + AT$, with the large temperature range as shown in **Figure 2.23**. This T -linear behavior is widely observed in other high-*T*c cuprates around the optimized doping. In the under doped region, ρ at low temperatures eventually shows insulating behavior represented as a function of logarithmic T particularly, and the results show that the superconductivity is reduced when applying an external magnetic field [109]. Recent study of the electrical resistivity in LSCO and YBCO has indicated metallic ($d\rho/dT$ > 0) behaviors at high temperatures even down to the extremely light doping limit ($y \sim 6.23$), where the electrical resistivity shows localization behavior at low temperatures. [110].

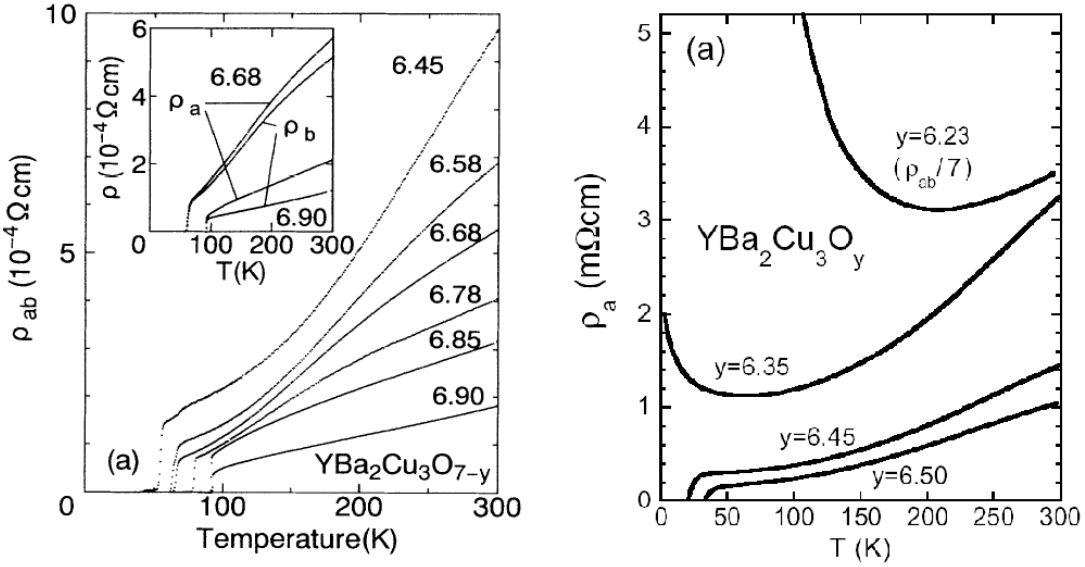

Figure 2.23 *In – plane resistivity as a function of temperature with various doping concentrations in YBCO. [110, 111].*

In conclusion, the research so far has yielded detailed information on many interesting properties, but there are still more interesting phenomena to be discovered. Further confinement of the electrons within these materials, the interaction at the different interfaces would be examined in our experimental section. The experiment methods will be discussed in the chapter 5.

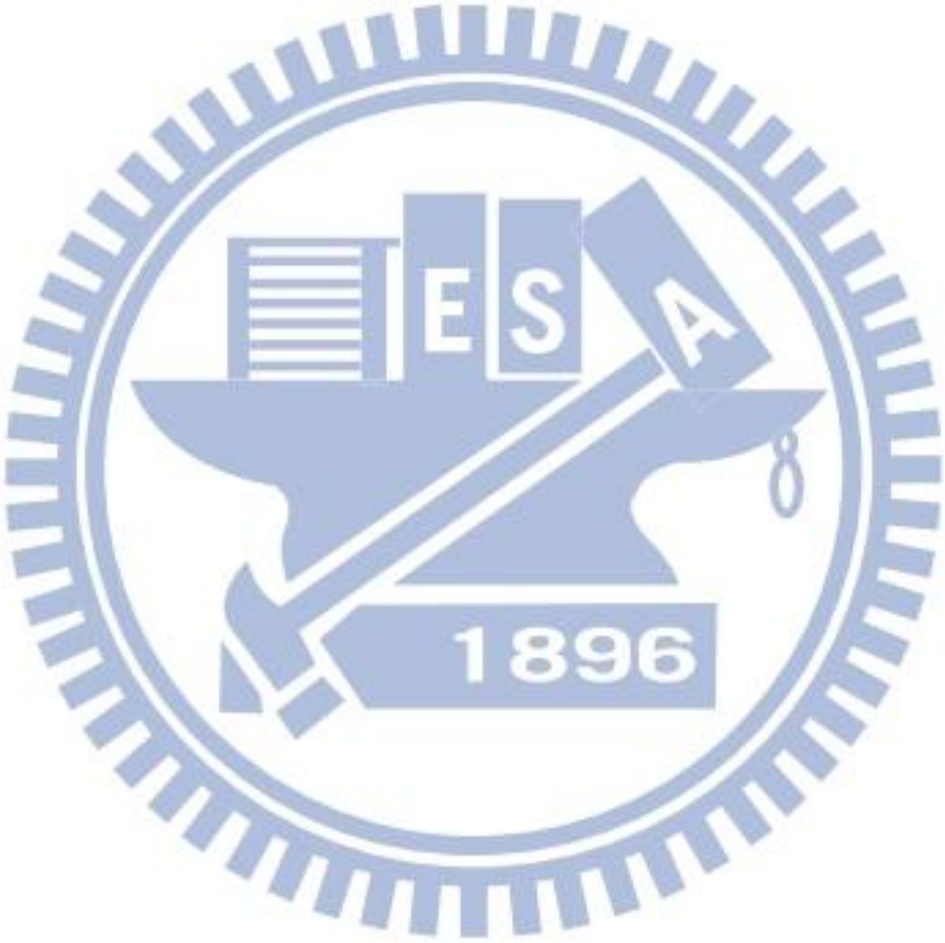

References

[1] *Moore's law*, http://en.wikipedia.org/wiki/Moore's law (04-16-2008).

[2] J. J. Sakurai, *Modern Quantum Mechanics*, Wiley (New York), Revised Edition, **1994**.

[3] D. J. Griffiths, *Introduction to quantum mechanics*, Upper Saddle River, NJ: Pearson Prentice Hall, 2nd ed., **2005**.

[4] G. Koster, B. L. Kropman, A. J. H. M. Rijnders, D. H. A. Blank, H. Rogalla, *Appl. Phys. Lett.* **1998**, *73*, 2920-2922.

[5] A. J. H. M. Rijnders, G. Koster, D. H. A. Blank, H. Rogalla, *Materials Science and Engineering: B* **1998**, *56*, 223-227.

[6] H. Koinuma, N. Kanda, J. Nishino, A. Ohtomo, H. Kubota, M. Kawasaki, M. Yoshimoto, *Appl. Surf. Sci* **1997**, *109-110*, 514-519.

[7] H. N. Lee, H. M. Christen, M. F. Chisholm, C. M. Rouleau, D. H. Lowndes, *Nature* **2005**, *433*, 395-399.

[8] D. A. Muller, N. Nakagawa, A. Ohtomo, J. L. Grazul, H. Y. Hwang, *Nature* **2004**, *430*, 657-661.

[9] J. H. Haeni, P. Irvin, W. Chang, R. Uecker, P. Reiche, Y. L. Li, S. Choudhury, W. Tian, M. E. Hawley, B. Craigo, A. K. Tagantsev, X. Q. Pan, S. K. Strei_er, L. Q. Chen, S. W. Kirchoefer, J. Levy, D. G. Schlom, *Nature* **2004**, *430*, 758-761.

[10] Robert Eisberg, Robert Resnick "Quantum Physics of Atoms, Molecules, Solids, Nuclei and Particles": 2nd Edition, Wiley 2006 .

[11] *Band theory of solids*, http://hyperphysics.phy-astr.gsu.edu/hbase/solids/band.html (05-13-2008).

[12] F. J. Morin, J. P. Maita, *Phys. Rev.* **1954**, *96*, 28-35.

[13] G. E. Stillman, C. M. Wolfe, J. O. Dimmock, *Journal of Physics and Chemistry of Solids* **1970**, *31*, 1199-1204.

[14] O. N. Tufte, P. W. Chapman, *Phys. Rev.* **1967**, *155*, 796-802.

[15] E. F. Schubert, *Room temperature properties of semiconductors: IIIV arsenides* http://www.rpi.edu/~schubert/Educational-resources/Materials-Semiconductors-III-Varsenides. pdf (22-06-2009).

[16] Gerrit Willem Johannes Hassink's Ph.D. thesis University of Twente, Enschede, the Netherlands (2009).

[17] B. C. Russell, M. R. Castell, *Phys. Rev. B*, **2008**, *77*, 245414.

[18] R. J. Francis, S. C. Moss, A. J. Jacobson, *Phys. Rev. B*, **2001**, *64*, 235425.

[19] W. A. Harrison, E. A. Kraut, J. R. Waldrop, R. W. Grant, *Phys. Rev. B* **1978**, *18*, 4402-4410.

[20] Y. H. Chu, Q. He, C. H. Yang, P. Yu, L. W. Martin, P. Shafer, R. Ramesh, *Nano Lett.* **2009**, *9*, 1726-1730.

[21] C.-H. Yang, J. Seidel, S. Y. Kim, P. B. Rossen, P. Yu, M. Gajek, Y. H. Chu, L. W. Martin, M. B. Holcomb, Q. He, P. Maksymovych, N. Balke, S. V. Kalinin, A. P. Baddorf, S. R. Basu, M. Scullin, R. Ramesh, *Nature Mater.* **2009**, *8*, 485-493.

[22] R. J. Zeches, M. D. Rossell, J. X. Zhang, A. J. Hatt, Q. He, C. H. Yang, A. Kumar, C. H. Wang, A. Melville, C. Adamo, G. Sheng, Y. H. Chu, J. F. Ihlefeld, R. Erni, C. Ederer, V. Gopalan, L. Q. Chen, D. G. Schlom, N. A. Spaldin, L. W. Martin, R. Ramesh, *Science* **2009**, *326*, 977.

[23] M. S. Park, J.-H. Song, A. J. Freeman, *Phys. Rev. B* **2009**, 79, 024420.

[24] A. Ohtomo, H. Y. Hwang, *Nature* **2004**, *427*, 423-426.

[25] N. Nakagawa, H. Y. Hwang, D. A. Muller, *Nature Mat.* **2006**, *5*, 204-209.

[26] M. S. Park, S. H. Rhim, A. J. Freeman, *Phys. Rev. B* **2006**, *74*, 205416.

[27] R. Pentcheva, W. E. Pickett, *Phys. Rev. B*, **2008**, *78*, 205106.

[28] N. Pavlenko, T. Kopp, Cond. Mat. **2009**, cond-mat/0901.4610.

[29] H. Chen, A. M. Kolpak, S. Ismail Beigi, *Phys. Rev. B* **2009**, *79*, 161402.

[30] Y. Li, J. Yu, *Cond. Mat.* **2009**, cond-mat/0904.1636.

[31] W.-J. Son, E. Cho, B. Lee, J. Lee, S. Han, *Phys. Rev. B*. **2009**, *79*, 245411.

[32] N. C. Bristowe, E. Artacho, P. B. Littlewood, *Phys. Rev. B.* **2009**, *80*, 045425.

[33] K. Janicka, J. P. Velev, E. Y. Tsymbal, *Phys. Rev. Lett*. **2009**, *102*, 106803.

[34] M. Huijben, G. Rijnders, D. H. A. Blank, S. Bals, S. van Aert, J. Verbeeck, G. van Tendeloo, A. Brinkman, H. Hilgenkamp, *Nature Mat.* **2006**, *5*, 556-560.

[35] C. Bell, S. Harashima, Y. Hikita, H. Y. Hwang, *Appl. Phys. Lett.* **2009**, *94*, 222111.

[36] S. Thiel, G. Hammerl, A. Schmehl, C. W. Schneider, J. Mannhart, *Science* **2006**, *313*, 1942-1945.

[37] U. Schwingenschlogl, C. Schuster, *Europhysics Letters*, **2009**, *86*, 27005.

[38] R. Pentcheva, W. E. Pickett, *Phys. Rev. Lett.* **2009**, *102*, 107602.

[39] C. W. Schneider, S. Thiel, G. Hammerl, C. Richter, J. Mannhart, *Appl. Phys. Lett.* **2006**, *89*, 122101.

[40] A. D. Caviglia, S. Gariglio, N. Reyren, D. Jaccard, T. Schneider, M. Gabay, S. Thiel, G. Hammerl, J. Mannhart, J. M. Triscone, *Nature* **2008**, *456*, 624-627.

[41] C. Cen, S. Thiel, G. Hammerl, C. W. Schneider, K. E. Andersen, C. S. Hellberg, J. Mannhart, J. Levy, *Nature Materials* **2008**, *7*, 298-302.

[42] C. Cen, S. Thiel, J. Mannhart, J. Levy, *Science*, **2009**, *323*, 1026-1030.

[43] N. Ogawa, K. Miyano, M. Hosoda, T. Higuchi, C. Bell, Y. Hikita, H. Y. Hwang, *Phys. Rev. B*, **2009**, *80*, 081106.

[44] R. Pentcheva, M. Huijben, K. Otte, W. E. Pickett, J. E. Kleibeuker, J. Huijben, H. Boschker, D. Kockmann, W. Siemons, G. Koster, H. J. W. Zandvliet, G. Rijnders, D. H. A. Blank, H. Hilgenkamp, A. Brinkman, *Phys. Rev. Lett.* **2010**, 104, 166804.

[45] A. Ohkubo, A. Ohtomo, J. Nishimura, T. Makino, Y. Segawa, M. Kawasaki, *Applied Surface Science* **2006**, *252*, 2488-2492.

[46] S. J. May, T. S. Santos, A. Bhattacharya, *Phys. Rev. B*, **2009**, *79*, 115127.

[47] J. Nishimura, A. Ohtomo, A. Ohkubo, Y. Murakami, M. Kawasaki, *Japanese Journal of Applied Physics* **2004**, *43*, L1032-L1034.

[48] G. Herranz, M. Basletic, M. Bibes, C. Carretero, E. Tafra, E. Jacquet, K. Bouzehouane, C. Deranlot, A. Hamzic, J. M. Broto, A. Barthelemy, A. Fert, *Phys. Rev. Lett.* **2007**, *98*, 216803.

[49] A. Brinkman, M. Huijben, M. van Zalk, J. Huijben, U. Zeitler, J. C. Maan, W. G. van der Wiel, G. Rijnders, D. H. A. Blank, H. Hilgenkamp, *Nature Materials*, **2007**, *6*, 493-496.

[50] M. Breitschaft, V. Tinkl, N. Pavlenko, S. Thiel, C. Richter, J. R. Kirtley, Y. C. Liao, G. Hammerl, V. Eyert, T. Kopp, J. Mannhart, *Cond. Mat.* **2009**, cond-mat/0907.1176.

[51] W. Siemons, G. Koster, H. Yamamoto, W. A. Harrison, G. Lucovsky, T. H. Geballe, D. H. A. Blank, M. R. Beasley, *Phys. Rev. Lett.*, **2007**, *98*, 196802.

[52] W. Siemons, G. Koster, H. Yamamoto, T. H. Geballe, D. H. A. Blank, M. R. Beasley, *Phys. Rev. B*, **2007**, *76*, 155111.

[53] A. Kalabukhov, R. Gunnarsson, J. Borjesson, E. Olsson, D. Winkler, T. Claeson, *Journal of Physics: Conference Series*, **2008**, *100*, 082039.

[54] C. L. Jia, S. B. Mi, M. Faley, U. Poppe, J. Schubert, K. Urban, *Phys. Rev. B* **2009**, *79*, 081405.

[55] P. R. Willmott, S. A. Pauli, R. Herger, C. M. Schlepfutz, D. Martoccia, B. D. Patterson, B. Delley, R. Clarke, D. Kumah, C. Cionca, Y. Yacoby, *Phys. Rev. Lett.* **2007**, *99*, 155502.

[56] A. Kalabukhov, R. Gunnarsson, J. Borjesson, E. Olsson, T. Claeson, D. Winkler, *Phys. Rev. B* **2007**, *75*, 121404.

[57] M. Basletic, J. L. Maurice, C. Carretero, G. Herranz, O. Copie, M. Bibes, E. Jacquet, K. Bouzehouane, S. Fusil, A. Barthelemy, *Nature Materials* **2008**, *7*, 621-625.

[58] F. J. Wong, M. Chi, R. V. Chopdekar, B. B. Nelson Cheeseman, N. D. Browning, Y. Suzuki, Cond. Mat. **2008**, arXiv:0809.0926v1.

[59] Z. S. Popovic, S. Satpathy, R. M. Martin, *Phys. Rev. Lett.* **2008**, *101*, 256801.

[60] M. Sing, G. Berner, K. Go, A. Muller, A. Ru, A. Wetscherek, S. Thiel, J. Mannhart, S. A. Pauli, C. W. Schneider, P. R. Willmott, M. Gorgoi, F. Schafers, R. Claessen, *Phys. Rev. Lett.* **2009**, *102*, 176805.

[61] A. Tsukazaki, A. Ohtomo, T. Kita, Y. Ohno, H. Ohno, M. Kawasaki, *Science*, vol. **2007**, *315*, 1388-1391.

[62] Mark Tillman's Ph.D. thesis , School of Applied Science, Cranfield University (2012).

[63] http://www.spring8.or.jp/en/news_publications/press_release/2010/100511.

[64] G. Arlt, *Journal of Materials Science*, vol. **1990**, *25*, 6, 2655-2666.

[65] C. A. Randall, N. Kim, J. Kucera, W. Cao, T. R. Shrout, *Journal of the American Ceramic Society*, **1998**, *81*, 3, 677-688.

[66] B. A. Tuttle, T. J. Garino, J. A. Voig, , T. J. Headley, D. Dimos, M. O. Eatough, *Science and Technology of Electroceramic Thin Films* **1995**, 117.

[67] W. Meissner, R. Ochsenfeld, *Naturwiss* **1933**, *21*, 787 .

[68] W.L. McMillan, *Phys. Rev.* **1968**, *167*, 331.

[69] N. L. Saini, H. Oyanagi, A. Lanzara, D. Di Castro, S. Agrestini, A. Bianconi, F. Nakamura, T. Fujita, *Phys. Rev. B* **2001**, *64*, 132510.

[70] D.H. Martin, *Magnetism in Solids*, MIT Press **1967**.

[71] L.-P. Levy, *Magnetism and Superconductivity*, Springer-Verlag **2000**.

[72] G.T. Rado, H. Suhl (editor), *Magnetism*, Academic Press **1966**, *4*.

[73] G. Ortiz et al., *Phys. Rev. Lett.* **1999**, *82*, 5317.

[74] J.C. Slater, *Phys. Rev.* **1936**, *49*, 537.

[75] B.C. Stoner, *Proc. Roy. Soc.* **1938**, *165A*, 372.

[76] J. Kübler, *Theory of Itinerant Electron Magnetism*, Oxford University Press **2000**.

[77] G.H. Jonker, J.H. Van Santen, *Physica* **1950**, *16*, 337.

[78] J.H. Van Santen, G.H. Jonker, *Physica* **1950**, *16*, 599.

[79] G.H. Jonker, *Physica* **1956**, *22*, 707.

[80] J. Volger, *Physica* **1954**, *20*, 49.

[81] S.-W. Cheong, H.Y. Hwang, *Ferromagnetism vs Charge/Orbital Ordering in Mixed-Valent Manganites*, in *Colssal Magnetoresistance Oxides*, edited by Y. Tokura, London, Gordon and Breach, Monographs in Condensed Matter Science **2000**.

[82] Soltan Soltan's Ph.D. thesis, Max Planck Institut für Festkörperforschung, Germany (2005)

[83] C. Zener, *Phys. Rev.* **1951**, *82*, 403.

[84] C. Zener, *Phys. Rev.* **1951**, *83*, 299.

[85] P.W. Anderson, H. Hasegawa, *Phys. Rev.* **1955**, *100*, 675.

[86] P.-G. De Gennes, *Phys. Rev.* **1960**, *118*, 141.

[87] M. Quijada, J. Cerne, J.R. Simposon, H.D. Drew, K-H. Ahn, A.J. Millis, R. Shreekala, R. Ramesh, M. Rajeswari, T. Venkatesan, *Phys. Rev. B* **1998**, *58*, 16093.

[88] W.Earenstein, N. D. Mathur, J. F. Scott, *Nature* **2006**, *442*, 759.

[89] E. Dagotta, T. Hotta, and A Moreo, Physics Reports, 2001, 344, 1-153

[90] K. Chahara, T. Ohno, M. Kasai, Y. Kozono, *Appl. Phys. Lett.* **1993**, *63*, 1990.

[91] Y. Tokura, *Colssal Magnetoresistance Oxides*, London, Gordon and Breach, Monographs in Condensed Matter Science **2000**.

[92] E.O. Wollen, W.C. Koehler, *Phys. Rev.* **1955**, *100*, 545.

[93] Z. Jirák, S. Vratislav, J. Zajícek, *Phys. Stat. Sol. A* **1979**, *52*, K39.

[94] E. Dagotto, *Nanoscale Phase Separation and Colossal Magnetoresistance*, Berlin, Heidelberg, Springer **2003**.

[95] S. Chikazumi, *Physics of Ferromagnetism*, Oxford, Clarendon **1997**.

[96] I.I. Mazin, *Phys. Rev. Lett.* **1999**, *83*, 1427.

[97] N.F. Mott, *Proc. R. Soc. A* **1936**, *156*, 368.

[98] R. Meservey, P.M. Tedrow, *Phys. Rep.* **1994**, *238*, 173.

[99] I.A. Campbell, A. Fert, *Ferromagnetic Materials*, ed E.P. Wohlfarth, Amsterdam, North-Holland **1982**, 3.

[100] J. G. Bednorz, K. A. M¨uller, *Z. Phys. B* **1986**, 64, 189.

[101] O. K. Andersen, A. I. Liechtenstein, O. Jepsen, F. Paulsen, *J. Phys. Chem. Solids* **1995**, *56*, 1573.

[102] Hajime Yagi's Ph.D. thesis, *Department of Physics, University of Tokyo, Japan (2006)*.

[103] K. Segawa, Y. Ando, *Phys. Rev. Lett.* **2001**, *86*, 4907.

[104] S. Uchida, N. P. Ong, *Phys. Rev. Lett.* **2012**, *16*, 1245

[105] Y. Tokura, S. Koshihara, T. Arima, H. Takagi, S. Ishibashi, T. Ido, S. Uchida, *Phys. Rev. B* **1990**, *41*, 11657.

[106] S. Uchida, T. Ido, H. Takagi, T. Arima, Y. Tokura, S. Tajima, *Phys. Rev. B* **1991**, *43*, 7942.

[107] F. C. Zhang, T. M.Rice, *Phys. Rev.B* **1988**, *37*, 3759.

[108] H. Eskes, G. A. Sawatzky, *Phys. Rev. Lett.* **1988**, *61*, 1415.

[109] Y. Ando, G. S. Boebinger, A. Passner, T. Kimura, K. Kishio, *Phys. Rev. Lett.* **1995**, *75*, 4662.

[110] Y. Ando, K. Segawa, A. N. Lavrov, S. Komiya, *J. Low. Temp. Phys.* **2003**, *131*, 793.

[111] T. Ito, K. Takenaka, S. Uchida, *Phys. Rev. Lett.* **1993**, *70*, 3995.

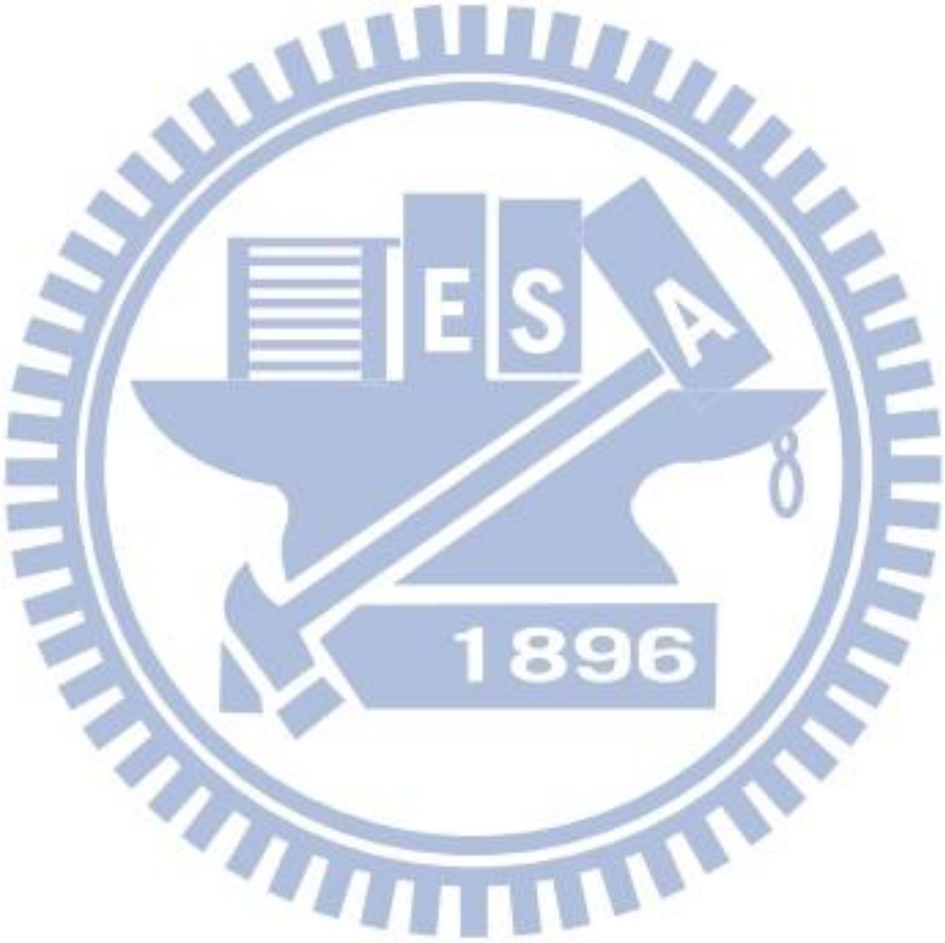

Chapter 3: Experimental Methods

3.1 Sample fabrication – Pulse laser deposition

Pulse Laser deposition (PLD) has become the most popular thin-film growth process over the recent decades because of its fast production of high quality thin films with precise composition from target. This technique was first demonstrated by Smith and Turner in 1956, and they had successfully grown semiconductors and dielectric thin films using ruby laser with a pulsed power of 3J and a rate of 1 pulse/min [1]. However, it did not attract much attentions at that time due to the large, unreliable, and expensive laser source. After the continuous progress of instruments and basic knowledge of higher energy physics, the advantages of this technique was then completely unveiled by the work of Dijkkamp *et al.* on the fabrication of high-temperature superconductors thin film in 1987 [2]. Recently, PLD has been applied for making high quality thin film in all kind of materials, including the oxides, nitrides, or carbides, metallic systems and even polymers or fullerenes.

Nowadays, the most common laser source is the excimer laser, which refers to the laser beam excited from the class of inert gas halide molecules, *e.g.* argon fluoride (ArF), krypton fluorde (KrF), and xenon fluoride (XeF). The excimer laser generally has higher intensity, and thus it is able to break the bonding of substances more efficiently into atoms, ions, or molecules and carries those in the same stochiometry with target to the substrate. In this study, the KrF laser was used with a wavelength of 248nm and pulse width of 30ns.

Except for the laser source, a vacuum system is also important for PLD system. The PLD system used in this study is a commercial machine, our setup is schematically illustrated in **Figure 3.1**. Inside the vacuum system, a target holder is placed at opposite the sample holder. For elongating the lifetime of target, the target holders are designed to automatically rotate and swing by computer program during laser irradiation. The sample holder is a nickel base alloy with a size of 1cm×1cm, which can be heated by laser diode. The temperature is also monitored by infrared radiometer. Comparing to the conventional PLD system, the biggest advantage of this machine is that it equips with reflection high-energy electron diffraction (RHEED) facility. The incident electrons with a glancing angle on the sample can help us to *in situ* observe the thin-film growth condition by the collected diffraction features from sample surface [3]. In a laser ablation process, a pulsed laser beam with a tunable frequency of 1-20 Hz is focused onto a target by a lens outside the chamber. Sometimes the process takes place in very high vacuum or in working pressure of some gas, which is decided on the

nature of deposited films. For example, the oxygen gas usually is used in growing oxide films, in order to redeem the presence of possible oxygen vacancies in the films while depositing.

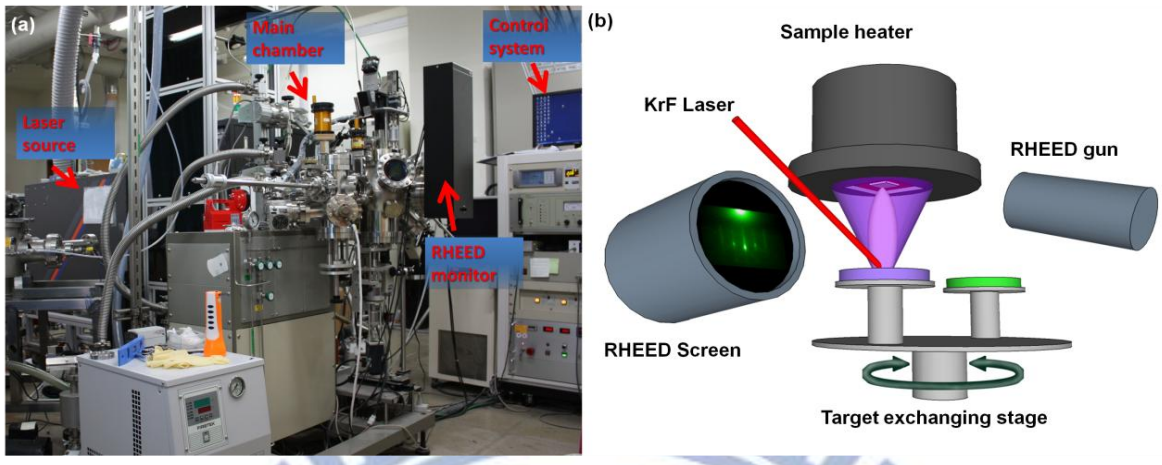

Figure 3.1 a) *The molecular beam expitaxy (MBE) laser deposition system used in this study.* ***b)*** *The schematic deposition process of MBE-PLD system.*

A PLD process involves complicated physical plasma phenomena such as collisional, thermal, and electronic excitation, exfoliation and hydrodynamics *etc* [4]. It generally can be divided into the following three parts:

(1). Dynamics of ablation materials, which is the step of interaction between laser and target.
(2). The subsequent inertial transport of the ablated species in vacuum or in some working pressure.
(3). Nucleation and growth of a crystalline thin film takes place on the substrate surface.

To grow high quality thin films, the deposition environment at these steps is very important and can be decided by several parameters: the laser parameters such as laser fluence (laser density/energy/cm^2), pulse duration and repetition rate (Hz); the preparation conditions, including target-to-substrate distance, substrate temperature, working gas and pressure. The laser fluence will affect the stoichiometry transfer from target and uniformity of films. The fast and strong heating of the target surface by the intense laser beam (typically up to temperatures of more than 5000 K) ensures that all target components irrespective of their partial binding energies evaporate at the same time. And then the ablated products has a angular distribution, obeying the $cos^n\theta$ law, in strongly forward direction from target to sample substrate, where the θ is the angle between the surface normal and the direction of propagation of species within the plasma plume [5]. Sometimes, in addition to the atoms and ions, the formation of large droplets or the target exfoliations in the plum, originating from the fast heating and cooling processes of the target, is un-avoided due to the extreme energy

condition, *e.g.* over high fluence. The *"splashed"* droplet associated with laser ablation results in the formation of micron to submicron size particles on the film surface and roughens the surface. Besides, the critical factor of film crystallinity is controlled by the substrate temperature. The energetic requirement for re-arrangement of the deposited ablation species is provided by the thermal exchange from heated substrate. Typically, when the substrate temperature is high enough, all ablation species on substrate can start to crystallize to form the right compound. In contrast, low substrate temperature will tend to result in the amorphous films. The partial pressure of working gas is also a very important parameter in the growth films. It is well-known that the ambient pressure decides the number of particulates arriving at the substrate, which is expected to follow the Beer's law [6]:

$$I = I_0 \cdot e^{(-\mathrm{P}\sigma\mathrm{x})} \qquad \textbf{(3.1)}$$

where I_0 is the initial plasma density at the target, I is the plasma density arriving at the substrate surface, P is the ambient gas pressure, σ is the total cross section for plasma-to-gas collisions, and x is the target-to-substrate distance. Hence, a ultra-high pressure will retard the source elements to adhere to the substrate and worsen the crystalline quality of the film.

After understanding the background of PLD process, the fabrication parameters of the samples in this study are all optimized. The experimental details will be presented in the results and discussions (Chapter 3)

3.2 Structural characterization

3.2.1 X-ray diffraction

After Röntgen discovered X-ray in 1895, people finally obtained a way into the un-visible world, which could not be observed before, for instance, the matters in atomic scale. X-ray is one kind of electromagnetic radiation with the wavelength in the range of 0.01–100 Å, and the basic element that can interact with X-ray is electron. When X-ray incidents into a matter and meets an atom including Z electrons, the electron will be excited due to the resonance with electromagnetic wave, and then irradiate another electromagnetic wave, called the exiting wave or scattered wave. The scattering amplitude is highly dependent on the electron density of the atom, which call atomic form factor $\left(f_{at}\left(r_k\right)\right)$. For a crystalline material, the atoms are regularly arranged to construct the *lattice*. These atoms (or other basic component, *e.g.* molecules) are called *basis*. And then the *crystal* is in definition the

combination of lattice and basis. Therefore, the generation of diffraction peak is decided by *structure factor rules*, which describes the sum of the scattering wave in terms of atoms and lattice:

$$F_{sc}(\Delta k) \equiv \sum_{r_k}^{basis} f_{at}(r_k) \cdot e^{-i2\pi\Delta k \cdot r_k} \qquad (\mathbf{3.2})$$

Where r_k is the *primitive unit cell vector* in real space and Δk is the *scattering vector*. When the *scattering vector* satisfies the Laue condition ($\Delta k = g$, g is the *reciprocal lattice vector*), diffraction will occur, which means that it also has to satisfy the Bragg's law $(2d\sin\theta = \lambda)$ [7]. It is important to understand the meaning of reciprocal lattice because each reciprocal space point represents a corresponding diffraction peak that we can observe from the experiments.

The X-ray structural analysis is the most common method to determine the crystallines of a material. For a powder sample or polycrystalline films, the typical diffraction feature is a ring pattern, which can be viewed as coalition of a huge of diffraction spots from the randomly distributed small crystal grain in space. For an epitaxial thin film grown on a single substrate, it also shows the diffraction spots feature and has broader width comparing to the single crystal, caused by some defects and mosaic structure. To understand the crystalline orientation of the thin films and epitaxy between films and substrate, some techniques are usually used, such as $\theta-2\theta$ scans, rocking curves, and φ scans. $\theta-2\theta$ scans, or called normal scans, are the scans always satisfy the Bragg's law, which the angle from incident beam to sample surface (θ) always keep half the angle from incident beam to detector (2θ). And thus, the diffraction signal only provides the information of the diffracted planes parallel to the sample surface because there is only variation of out-of-plane components in reciprocal lattice vectors, for example such as the (001) oriented films, only the (00*l*) family planes in the sample can be observed in $\theta-2\theta$ scans. The rocking curve usually means the scans of θ ranging around Bragg angle, which can describe the mosaic degree of the epitaxial films. The φ scans, or the azimuthal scans, means the rotation of the sample itself. To get the φ scans, one should first find the so-call asymmetry reflections of substrate and films (the reciprocal lattice vector including the in-plane component), and then rotate sample stage. For a good expitaxy, the films should present as same numbers of peaks as substrate, which means they have the same symmetrical fold. The techniques mentioned above are all the line scans; however, sometimes line scans cannot reveal the real shape of the diffraction patterns in

reciprocal space, especially those in the crystal with tilted and distorted structure. Therefore, the advanced technique called *reciprocal space mapping* (RSM) needed to resolve these non-regular structures. Reciprocal-space mapping measurement requires setting of the measuring range of $2\theta/\theta$ scans, and setting of the measuring range of off-set angle β, shown in **Figure 3.2**. For a double-axis diffractometer, the off-set angle β is the difference of the θ from out-of-plane direction, and for a triple-axis, β can be the varied by one additional freedom of degree, defined by χ, where χ is an angular circle perpendicular to incident beam. And then the RSM is constructed by a lot of $2\theta/\theta$ scans with different offset angles.

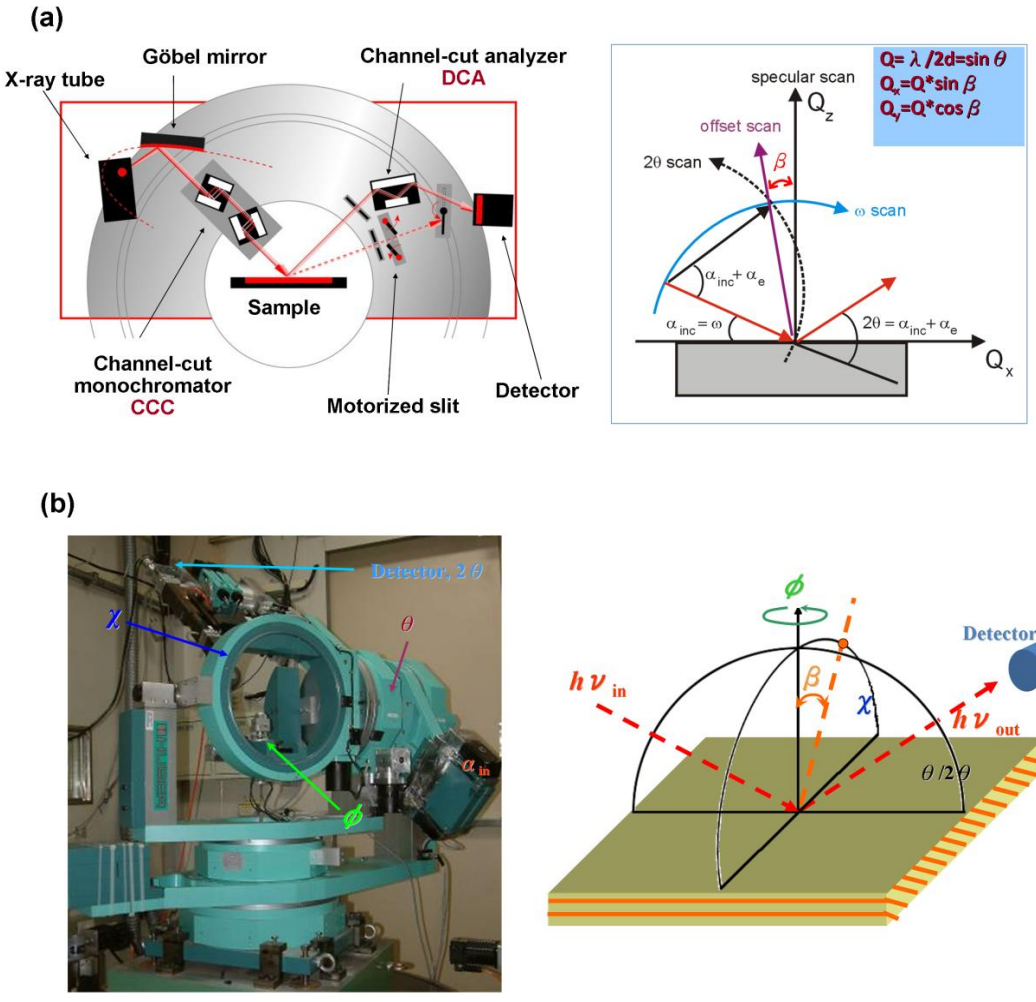

Figure 3.2 ***a)*** *The typical scheme of double-axis diffractometer (left), and the corresponding motion for each angular motor in real space (right). (Figure courtesy of Panalytical B.V)* ***b)*** *The high-resolution triple-axis diffractometer (Huber 8 circle diffractometer) at NSRRC Beamline 17B1 (left), and the scheme of the corresponding motion of each angular motor in*

real space (right) [15].

X-ray diffraction characterization of the films in this dissertation was conducted in two kinds of instruments. One is the commercial machine, which is the PANalytical X'Pert Pro 4-circle x-ray diffractometer with Cu $K_{\alpha 1}$ radiation ($\lambda = 1.54$ Å). The other is the Huber high resolution four-circle diffractometer using a synchrotron as source, where the energy is set as 10KeV (1.24Å); these RSM experiments were mostly performed at wiggler beamline BL13A, BL17A or BL17B1 at the National Synchrotron Radiation Research Center (NSRRC), Taiwan. The incident X-rays were made monochromatic with a Si (111) double-crystal monochromator. With four pairs of slits between sample and detector, the typical scattering vector resolution in the vertical and horizontal scattering planes was set to ~10^{-4} nm^{-1} to dramatically decrease the noise single and raise the resolution during experiments.

3.2.2 Transmission electron microscopy

Transmission electron microscopy (TEM) was performed to characterize the microstructures of the films, such as morphological and crystallographic features. The operation of TEM is similar to the way of optical microscope, which also obeys the lens formula. The detailed setup of TEM instrument is shown in **Figure 3.3 a)**. The electron beam is emitted from the filament accelerated by a high voltage (100kV - 1000kV) and then focused on the sample by electromagnetic lenses (condenser lenses). When the beams pass through the specimen, two kinds of modes can be observed. One is *"image mode"*, where all the transmitted and diffracted beams are focused by object lens to form the first magnified image; the image can be viewed as "*virtual object*" and focused by the intermediate lens to magnify again. The final image is presented at the fluorescent viewing screen (**Figure 3.3 b))**. Because the electron beams behave similarly as light, it also produces diffraction patterns while interacting with specimen. Therefore, the second mode is *"diffraction mode"*. The change from image mode to diffraction mode can be performed by decreasing the electrical current in intermediate lens, and thus the focal length of intermediate lens will extend backward to the "back focal plane". At this time, the diffraction patterns become the virtual object and follow the artificial dashed line to form the magnified diffraction image on the screen. Based on these two modes, more advanced imaging and diffraction techniques are developed to get the detailed structural information, including the bright-field and dark-field image, selected area

electron diffraction (SAD); convergent-beam electron diffraction (CBED), phase-contrast imaging (high-resolution TEM, HRTEM); and Z-contrast imaging [8].

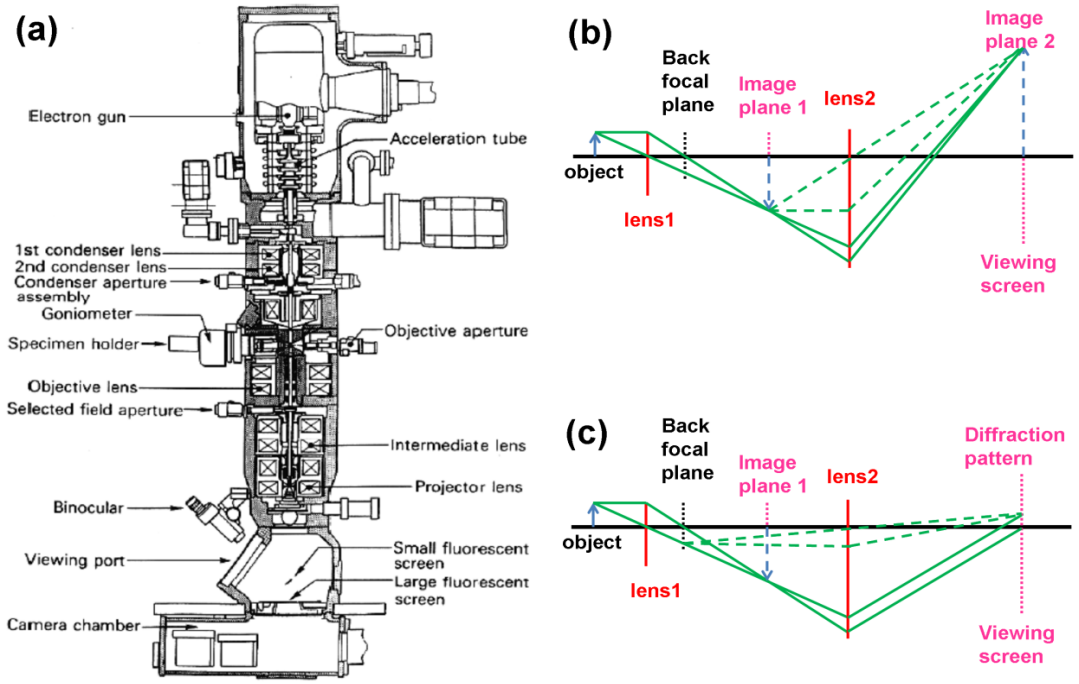

Figure 3.3 ***a)*** *The detailed setup of a common TEM instrument.* ***b)*** *the concept of the image mode in TEM observation.* ***c)*** *The concept of the diffraction mode in TEM observation [8].*

Since electrons scattering is strongly dependent on the atomic electronic potential of the sample, samples should be prepared in very thin region, which less than 1 μm for TEM characterization. In this dissertation, the focused ion beam (FIB, SII Nanotechnology SMI 3050SE) was used to fabricate the specimen for TEM cross-section observation. Before cutting the sample, SiO_2 thin film of 100 nm had been deposited by E-gun system as a passivation layer, preventing the damage from the bombardment of Ar ion beam. Then Pt thin film around 20 nm capped onto the SiO_2 layer for first observation by scanning electron microscopy (SEM). First, the Ar beam with the energy of 30 keV bombarded the surface of sample to localize the chosen area, and then the beam was tuned to lower energy of 5 keV to thin the chosen area finely until the thickness achieved around 50nm. Finally, the specimen was picked up to a Cu grid for following TEM observation. The microscopy that was used is the JEOL JEM-2010F operated at 200 V.

3.3 Techniques for measuring physical properties

3.3.1 Atomic Force microscopy

Atomic landscapes of material surfaces could be imaged in real space after the invention of Scanning Probe Microscope (SPM) in 1980s. SPM as well known includes two types: one is the Scanning Tunneling Microscope (STM), which helped the inventors, Binnig and Rohrer, to win the Nobel Prize in 1980s. Although the STM can image the surface near atomic scale, it is still limited in conducting materials. Several years later (1985), the atomic force microscope (AFM) was then invented, also by Binnig *et al*, to overcome this disadvantage. The introduction of the atomic force microscope (AFM) in 1986 opened the SPM field to insulating and semiconducting materials as well [9].

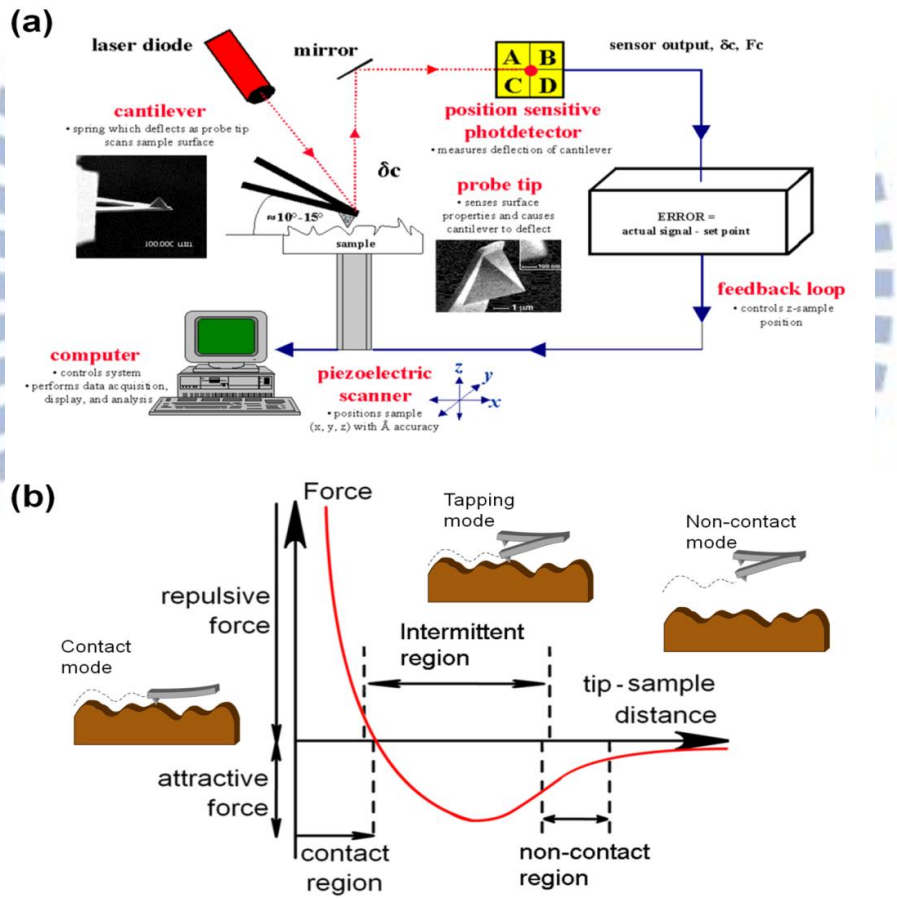

Figure 3.4 ***a)*** *The instrumental depiction for AFM operation. (copyright © nanodic.com)* ***b)*** *The correspondingly operative region of three typical modes of AFM in Lennard-Jones pair potential energy [16].*

The principle for operating AFM is to use the interactions between tip and sample

surface. The AFM instrument is composed of a cantilever with a very sharp tip, a laser diode, a photo-sensor, a piezoelectric scanner, and controller electronics as shown in **Figure 3.4 a)**. The AFM tip is usually made of micromachined silicon or silicon nitride. A laser emitted from the laser diode is bounced off the back of the cantilever onto a position sensitive photodiode detector. This detector records the deflections from the bending of cantilever during the tip is scanned over the sample. In order to prevent the surface damage while the tip scans, the piezoelectric scanner can control the distance between the sample stage and tip by the feedback mechanism manipulated by a computer.

According to the Lennard-Jones pair potential energy function described below (**Equation 3.2** and **Figure 3.4 b)**), when the tip continuously close to the sample surface, the interaction will first be attractive (Van der Waals force) and then become repulsive forces (Coulomb repulsive force) [16].

$$F(r) = -\frac{\partial E}{\partial r} = 24\varepsilon[2(\frac{\sigma^{12}}{r^{13}}) - (\frac{\sigma^{6}}{r^{7}})] \quad \textbf{(3.3)}$$

Attractive or repulsive forces resulting from interactions between the tip and the surface will cause a positive or negative bending of the cantilever. Therefore, three basic operation modes were developed to observe different types of surface. The first is contact mode: the direct contact has high atomic resolution by use the repulsive force; nevertheless, it also might cause the damage on surface. The force between the tip and the surface is kept constant during scanning by maintaining a constant deflection, and the distance is about 3Å. This kind of mode is not suitable for soft matters. The second is non-contact mode: this mode is measured by attractive force and non-destruction to surface. The cantilever is oscillated at a frequency slightly above its resonant frequency where the amplitude of oscillation is typically a few nanometers (<10 nm). The resonance frequency will be varied if the distance between sample and tip is changed. Hence, to maintain the oscillation amplitude or frequency, the tip-to-sample distance needs to be adjusted by feedback loop system. Measuring the variation of tip-to-sample distance at each (x,y) data point allows the scanning software to construct a topographic image of the sample surface. The advantage of this mode is that the tip never makes contact with the sample and therefore cannot disturb or destroy the sample, which is particularly important in biological applications. However, it also has poorer atomic resolution due to the perturbation in air. The last mode is the tapping mode: it is the most widely used mode recently and works similar to non-contact mode. The tapping mode is operated in the region of the competition between attractive and repulsive forces. The cantilever is oscillating close to its resonance frequency. A feedback loop system ensures that

the oscillation amplitude remains constant, such that a constant tip-sample interaction is maintained during scanning. Therefore, it has the largest oscillation amplitude (typically >20nm) to allow tip to "tap" on the sample surface. The advantages of the tapping mode are the elimination of a large part of permanent shearing forces and the causing of less damage to the sample surface, even with stiffer probes.

In this dissertation, the topography of the resulting films were studied by the commercial AFM instruments (Bruker Escope and Bruker Multimode). Tips used for imaging were Si cantilevers with an elastic constant of 2-4.4 N/m and a resonance frequency of 60~100 kHz.

3.3.2 Piezoresponse Force Microscopy

Piezoresponse force microscopy (PFM) is one variant of atomic force microscopy (AFM) that can image and manipulate the ferroelectric domains. The basic idea of Piezoresponse Force Microscopy (PFM) is based on the *"converse piezoelectric effect"*, which is a linear coupling between the electrical and mechanical properties of a material. The converse piezoelectric effect (CPE) means that a resultant strain due to the piezoelectric tensor will be induced in piezoelectric or ferroelectric material when an electric field is applied, which in turn leads to a physical deformation. This effect can be described by following equation: [10-11]

$$\varepsilon_{jk} = d_{ijk} E_i \qquad i, j, k = 1, 2, 3 \qquad \textbf{(3.4)}$$

Where ε_{jk} is the strain tensor, d_{ijk} is the piezoelectric tensor, and E_i is the electric field. In PFM, the electric source is AC voltage because a static or DC voltage cannot produce a obvious displacement, which beyond the detector limitation. Therefore, in order to separate this low level signal from random noise, a modulated voltage reference signal with a lock-in technique is needed. In this case, under the applied AC modulation voltage $V = V_0 \cos(\omega t)$, it results in sample surface vibration with the form $\Delta Z = \Delta Z_0 \cos(\omega t + \varphi)$, where ΔZ_0 is the vibration amplitude $\Delta Z_0 = d_{33} V_0$, and φ is phase ("$\varphi = 0^0$" means the sample domain polarization is oriented parallel to the applied electric field, and "$\varphi = 180^0$" oriented anti-parallel to the applied electric field). Such oscillation from the contact of tip and surface would be directly reflected in the amplitude and phase signal, and read out using a lock-in amplifier.

There are two typical PFM imaging modes for detecting ferroelectric domain, which is

described below.

3.3.2.1 Vertical PFM

In vertical PFM imaging, out-of-plane polarization is measured by recording the tip-deflection signal at the frequency of modulation. **Figure 3.5 a)** shows a schematically illustration of vertical PFM manipulation. If the polarization is parallel and aligned with the applied electric field, the piezo effect will be positive, and the sample will locally expand. If the local sample polarization is anti-parallel with the applied electric field, the sample will locally shrink. The similar behaviors can be observed if the applied electric field is reversed. This sign-dependent behavior means that the phase of the cantilever provides an indication of the polarization orientation of the sample when an oscillating voltage is applied to the sample.

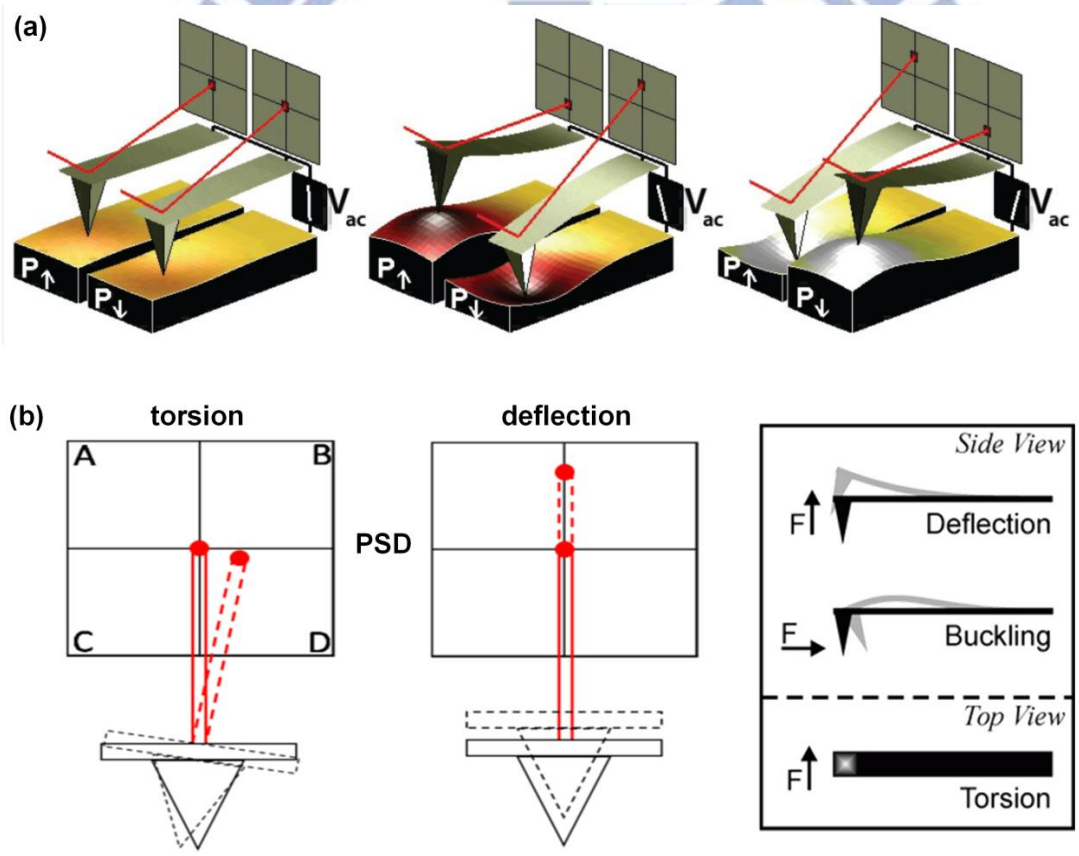

Figure 3.5 a) *Structural variations depend on the polarization sign in vertical PFM manipulations, which cause the deflection of laser signal in photodetector. (Figure courtesy of S. Jesse, ORNL.)* ***b)*** *Two types of distortion of cantilever in in-plane PFM manipulations: torsion and buckling. The torsion makes the laser signal a horizontal shift in photodiode, whereas the buckling will make a similar feature to deflection [16].*

3.3.2.2 Lateral PFM

In most of the real cases, the studied sample often contains non-zero lateral components in its piezoelectric tensor. In this case, the in-plane component of polarization is detected by lateral motion of the cantilever due to bias-induced surface shearing. For example, if the local polarization is oriented in the in-plane direction and perpendicular to the scan direction of tip (**Figure 3.5 b)**), the force will make *torsion* on the cantilever and thus lead to a transverse shift of deflection on the detector. Besides, the in-plane components still have another choice, which is along the scan direction of tip. This kind of in-plane components make the cantilever buckle along the scan direction, and the readout of buckling is very sensitive to the position of the laser beam on the back side of the cantilever: displacing the laser beam from the very end on top of the tip towards the middle of the cantilever results in an inversion of the readout signal. Thus, the buckling in lateral PFM is difficult to detect because the motion of signal is mainly along the longitudinal direction, which is easily confused with out-of-plane polarization in vertical PFM.

In this dissertation, lateral PFM equipped with heating stage is used to measure the rotation of ferroelectric domains in PZT thin films. The in-plane PFM images are also obtained in contact mode by Bruker Escope and Multimode instruments. Tips are conductive with coated Ti-Pt thin film, with an elastic constant of 4.5 N/m and a resonance frequency of 120~190 kHz. The scanning speed was set at 5 μm/s, ac excitation frequency was 10.5 kHz, and the ac amplitude was up to 7-10 Vpp.

3.4 Superconducting Quantum Interference Device Megnetometer

Superconducting quantum interference device magnetometer (SQUID) is the most sensitive device in the detection of magnetic flux, which was invented by R. C. Jaklevic, *et al* of Ford Research Labs in 1964 [12]. The basic principle behind the SQUID is based on the *Josephson effect* postulated by Josephson in 1962, which indicates a current across a thin insulating layer between two superconductors without any external electric field [13]. The device to reveal this phenomenon is called *Josephson junction*, made by J. Rowell and P. Anderson at Bell labs in 1963 [14].

As the scheme shown in **Figure 3.6**, the central element of SQUID is composed of two Josephson junctions in parallel, which is also called direct current (DC) SQUID. In the absence of external magnetic field, the input current splits into the two branches equally.

When a tiny magnetic field is applied, it will generate a screening current I_s due to the conservation of superconducting wave function and cancels out the net flux in the ring. The induced current I_S makes the one branch of current (I_A) equal to half the input current plus screening current $(I_A = I/2 + I_S)$, whereas the other branch of current becomes half the input current minus screening current $(I_A = I/2 - I_S)$. As soon as the current in either branch exceeds the critical current (I_C) of the Josephson junction, a voltage appears across the junction. When the magnetic field gradually increases, the screening current also increases. However, when the magnetic reaches achieve half the magnetic flux quantum, the screening current should change its direction for satisfying the flux quanta in a close loop. Finally, one can measure the variation of voltage across the junction as a function of total current through the device, and further a function of the applied magnetic.

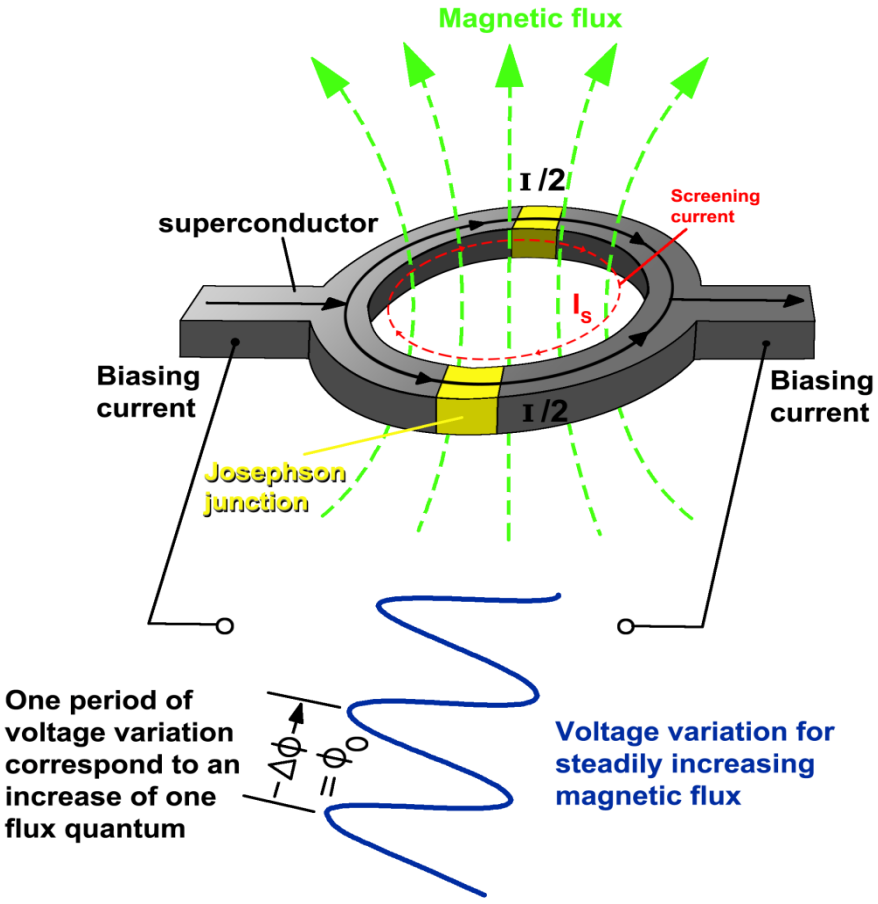

Figure 3.6 *Schematic representation of a Josephson device (or a simple SQUID magnetometer) interacted with a magnetic field. The change of magnetic flux will induce a variation in measured voltage. (Redrawn from the website http://hyperphysics.phy-astr.gsu.edu/hbase/solids/squid.html)*

In this dissertation, we adopt a commercially available Quantum Design MPMS-XL Superconducting Quantum Interference Device (SQUID) magnetometer to analyze the magnetic properties in nanostructure samples. The magnetometer contains a high-precision temperature control system that allows measurements with an accuracy of 0.01 K between 1.8 K and 350 K. A superconducting magnet provides magnetic fields up to 7 Tesla, with a field accuracy of 0.05 Gauss. The measuring approach is the no-over shoot mode, in which the magnetic field is changed monotonically from the initial field setting without overshooting the final value.

3.5 X-ray absorption spectroscopy

XAS and X-ray photoelectron spectroscopy (XPS) are the two most widely used core electron spectroscopies. The measurements of photo-absorption by excitation of a core-level electron into unoccupied states as a function of photon energy is called x-ray absorption spectroscopy. We can obtain information about the valence states and the local environments surrounding each element by XAS spectra. The advantages of XAS technique are that it can probe samples in a surface-sensitive (electron yield detection) mode or bulk-sensitive (transmission), which is of great importance for artificially made multilayer structures. **Figure 3.7** shows the principles of X-ray absorption spectroscopy, using a one-electron model for the case of *L* edge absorption in a *d* band transition metal. The absorption intensity from the initial state $|i\rangle$ can be calculated by summing all possible final states $|f\rangle$:

$$I(h\nu) = \sum_f \left|\langle f|T|i\rangle\right|^2 \delta\left(E_i - E_f - h\nu\right), \qquad \textbf{(3.5)}$$

where $h\nu$ is the photon energy of the x ray, T is the dipole transition operator. The 2*p* core-level XAS spectra of transition metal compounds well reflect the 3*d* electronic states in the 3*d* transition metal compounds including the symmetry and the crystal field splitting of the 3*d* orbitals. Thole *et al*. [17] performed the calculations of transition metal 2*p* XAS spectra of 3*d* transition-metal ions in a crystal field.

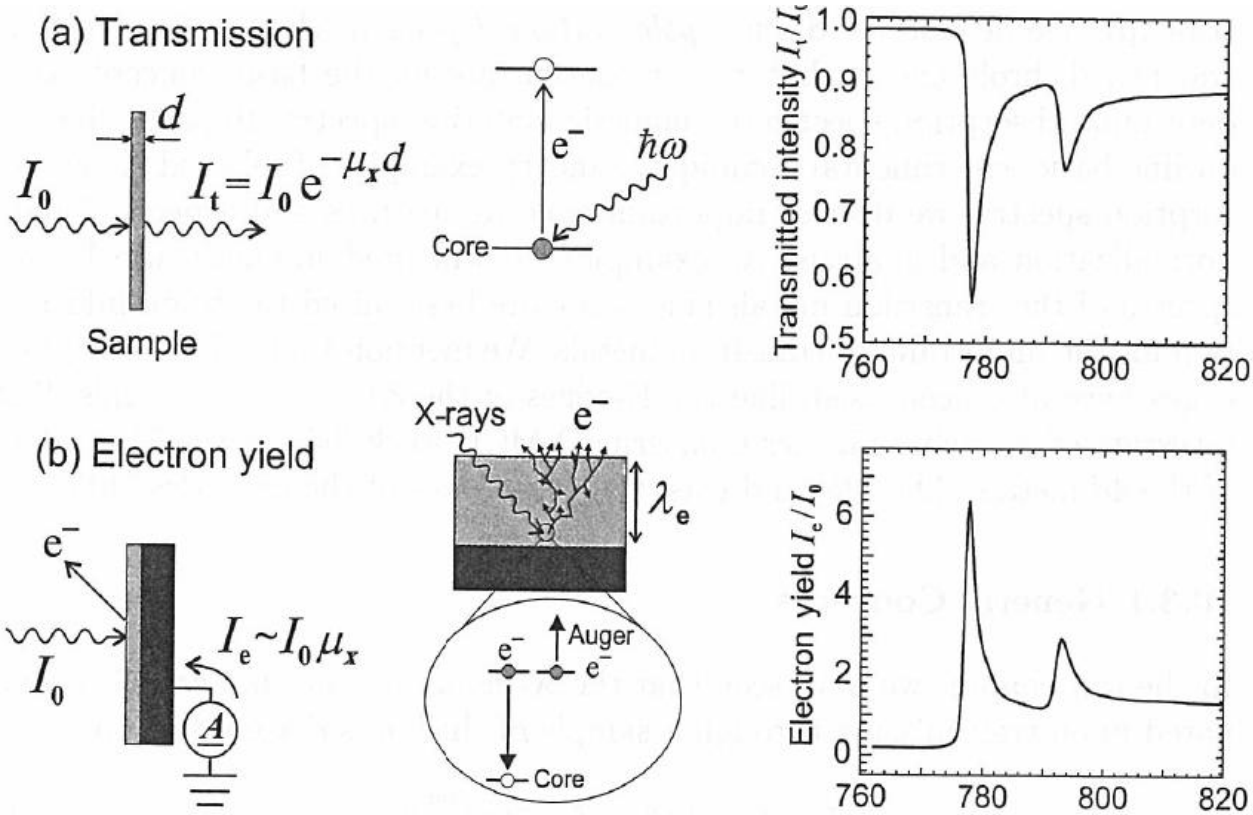

Figure 3.7: *Principles of X-ray absorption spectroscopy, using a one-electron model* **a)** *Transmission mode and while* **b)** *is the total electron yield mode [17,18].*

There are three measurement modes for XAS, the transmission-mode, the total-yield mode and Fluorescence mode. **(Figure 3.7 a)),** transition mode is the most direct measurement mode, in which the intensity of the x-ray is measure before and after the sample and the ratio of the transmitted x-rays is counted. Transmission-mode experiments are standard for hard x-rays, though for soft x-rays, they are difficult to perform because of the strong interaction of soft x-rays with the sample. The total-yeild method can be classified in two modes, the total-electron yield (TEY) shown in **(Figure 3.7 b))** and the total-fluorescence yield (TFY) modes presented in **Figure 3.8.** TEY and TFY denote measuring the current flow and the fluorescence of the sample radiated x-ray, respectively. TEY mode is surface sensitive while TFY mode is bulk sensitive and the probing depth of TEY and TFY modes is ~5 nm and ~100 nm, respectively. The TFY mode suffers from self-absorption because of its long probing depth. In the present work, TEY and TFY mode were employed.

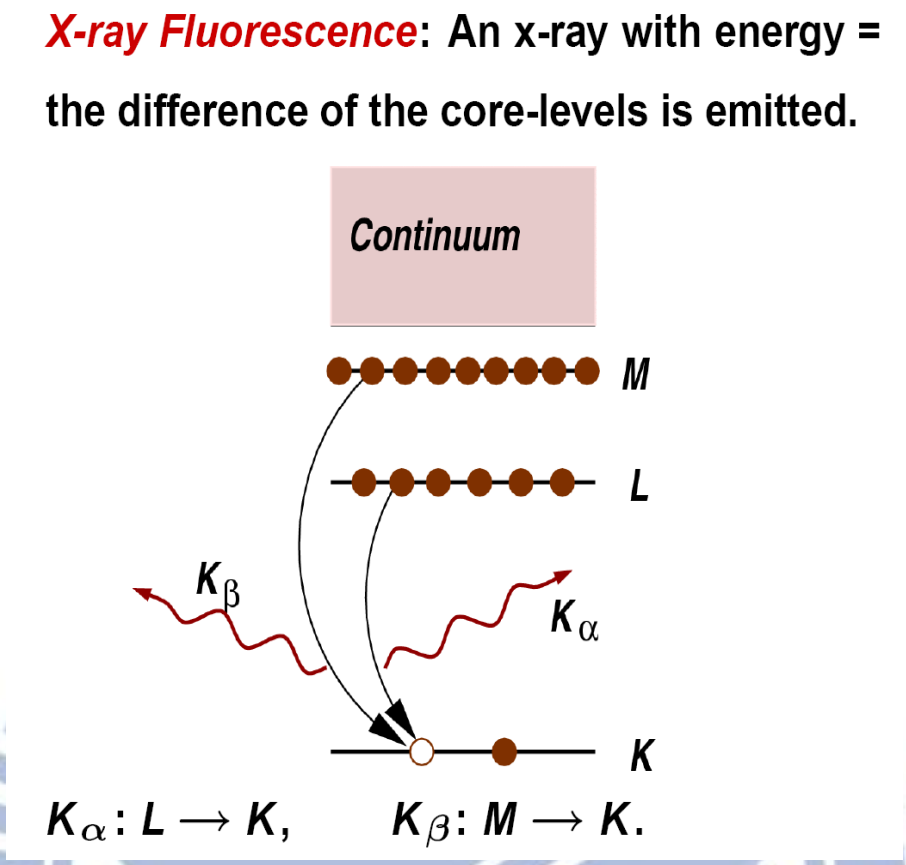

Figure 3.8: *Principles of X-ray absorption spectroscopy, using a one-electron model for Fluorescence mode [18].*

3.6 X-ray magnetic circular dichroism

As we have known that relativistic electrons in the storage ring are deflected by the bending magnets. Those electrons keep them in a closed circular orbit and emit highly intense beams of linearly polarized x-rays in the plane of the electron orbit. On the other words, they emit circularly elliptically polarized light out of the plane. Currently, a number of alternative sources for circularly polarized synchrotron radiation are under development in the world wide. The most notable ones are so-called insertion devices like helical and crossed undulator and wigglers [19,20]. Both of them are complex arrays of magnets with which the electrons in a storage ring are made to oscillate in two directions that are perpendicular to their propagation light direction and the result emitted circularly polarized light.

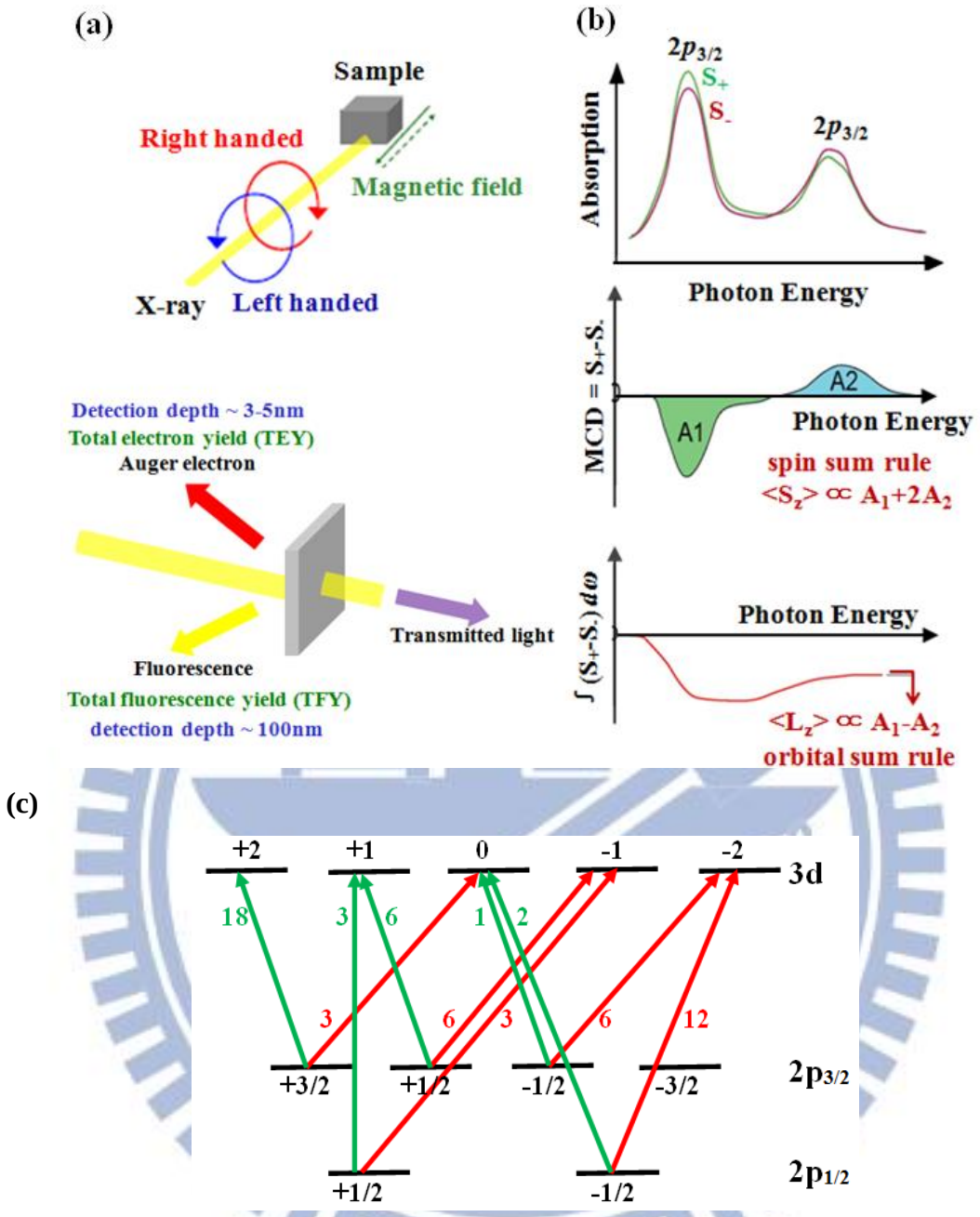

Figure 3.9: *Schematic diagram of x-ray magnetic circular dichroism (XMCD).* **a)** *Experimental set up for XMCD measurements.* **b)** *Circularly polarized x-ray absorption spectra.* **c)** *Transition probability of 2p → 3d absorption with circularly polarized x rays for less-than-half filled 3d electronic configuration [21].*

Figure 3.9 shows schematic diagram of XMCD. Using circularly polarized light in XAS, the absorption intensity depends on the helicity of the incident light. When right- and left-handed circularly-polarized x-rays are irradiated on a sample under applied magnetic fields, differences in the absorption intensity are observed because of differences of transition matrix elements (or selection rule). XMCD is defined as the difference of the absorption

spectra of parallel and antiparallel helicity of the x-rays light to the magnetization direction of a material. The line shape of XMCD spectra reveals electronic structure related to the magnetism of magnetic materials. XMCD is sensitive to magnetically active components and is an element specific measurement because of core-level excitation. In addition, we can estimate spin and orbital magnetic moments separately from integrated intensities of XAS and XMCD spectra by applying XMCD sum rules as described below. Therefore, XMCD is a powerful tool to investigate magnetic properties of materials. **Figure 3.9 c)** shows the transition probability of $2p \rightarrow 3d$ absorption with circularly polarized X rays. Transition probability is proportional to

$$3\left|\left\langle 2m_d \left| r_{\pm} \right| 1m_p \right\rangle\right|^2 = \left|\left\langle 2m_d \left| \frac{x \pm iy}{\sqrt{2}r} \right| 1m_p \right\rangle\right|^2 = \left|c^1\left(2m_d, 1m_p\right)\right|^2 \qquad \textbf{(3.6)}$$

where $c^1(2m_d, 1m_p)$ is the Gaunt coefficient and where m_d is the magnetic quantum number of the 3*d* states. The circular polarization is expressed by $r_{\pm}$, where r_+ and r_- have helicity 1 and -1, respectively. The selection rule is derived from that equation and the transition induced by circularly polarized light with helicity is change in the magnetic quantum number by ±1 while the spin moment is conserved. The final 2*p* hole is located at the $2p_{3/2}$ and $2p_{1/2}$ states, and two absorption edges related to the $2p_{3/2}$ to 3d and $2p_{1/2}$ to 3*d* transition, called L_3 and L_2, respectively. The $2p_{3/2}$ and $2p_{1/2}$ have four and two degenerated states, respectively. When we apply magnetic field on the magnetic material, the final state *d* orbitals are split according to the spin and are slightly affected by the magnetic quantum number. Thus, the final state for both spin directions can be classified as the states $|2, m_d\rangle$ state. For $2p_{3/2}$ and positive helicity, the transition probability ratios for each $|2, m_d\rangle$ are 18, 6 and 1. The transition probability ratios for $2p_{3/2}$ with opposite helicity are 3, 6 and 6 as shown in figure. Similarly, the transition probability ratios for $2p_{1/2}$ with positive and negative helicities are 3 and 2, and 3 and 12, respectively. The difference of the transition probabilities between positive and negative helicities provides the XMCD.

3.7 X- Ray photoemission spectroscopy

Photoemission spectroscopy (XPS) is a powerful experimental method which can directly observe the electronic structure of solids. **Figure 3.10** illustrates a schematic diagram of the principle of XPS. When a photon of sufficiently high energy impinges on a solid, an electron in a solid will be emitted as a photoelectron, according to the photoelectric effect. By

analyzing the kinetic energy of the photoelectron in the vacuum (E_{kin}^{v}), one can obtain XPS spectra as shown in **Figure 3.10**.

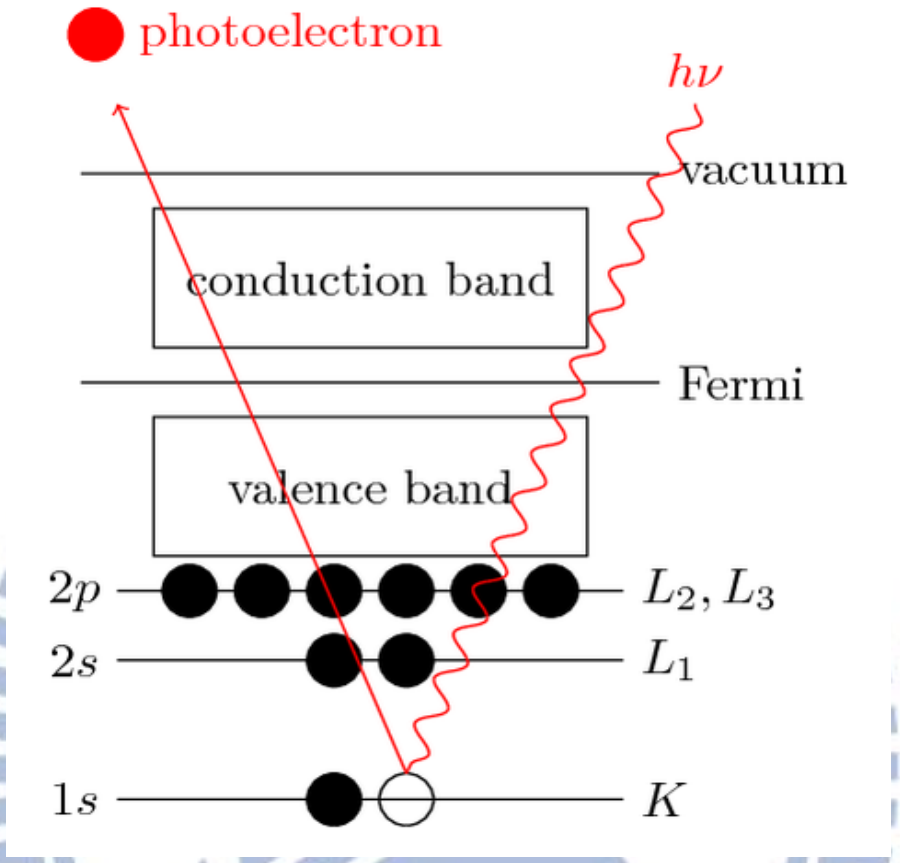

Figure 3.10: *Principle of X- Ray photoelectron spectroscopy [21]*

In the single-electron approximation method, the effect of electron correlation can be neglected and XPS spectra represented the density of states (DOS) of electronic bands structures. E_{kin}^{v} also provides information about the strength to bind a electron to a solid. According to the energy conservation law,

$$E_{kin}^{v} = \hbar\upsilon - E_B - \phi \qquad \textbf{(3.7)}$$

where $h\upsilon$ is the energy of the incident photon, E_B is the binding energy relative to the Fermi level E_F (chemical potential μ) and Φ is the work function of the solid. The work function is the energy required for an electron to moving from a solid through the surface and to reach the vacuum level (E_{vac}), that is,

$$\phi = E_{vac} - E_F \qquad \textbf{(3.8)}$$

Because one cannot obtain E_{kin}^{v} without measuring Φ but one can measure the kinetic energy of the photoelectron relative to E_F (E_{kin}) directly, it is convenient to use E_{kin}. Then we obtain

$$E_{kin} = \hbar\upsilon - E_B \qquad \textbf{(3.9)}$$

In the mean-field (Hartree-Fock) picture (one-electron approximation), E_B is equal to the energy of an electron inside the solid before it is emitted. Therefore, the energy distribution of the electrons in the solids can be directly mapped from the distribution of the kinetic energy of the photoelectrons emitted by monochromatic incident photons. **Figure 3.10** shows how the electronic DOS is mapped from the emitted photoelectrons.

In real materials, photoemission spectra are influenced by the entire electron system of the solid, in addition to the one-electron energy (frozen-orbital approximation). In the photoemission process, holes are produced by removing electrons from the solid surface and the surrounding electrons goes to screen the holes to lower the total energy of the system. Therefore, considering the entire electron system, the binding energy E_B is given by the energy difference between the *N*-electron initial state E_i^N and the ($N-1$) - electron final state E_f^{N-1} as $E_B = E_f^{N-1} - E_i^N$

In other hand, E_B is the energy of the hole produced by the photoemission process, including the relaxation energy of the total electron system. Hence, much information about the electron correlation is derived from the XPS.

3.8 Electronic transport analysis

Electrical measurements as a function of temperature and magnetic field allow for a variety of transport properties such as Hall electron density and electron mobility to be determined. From these it is often possible to draw other conclusions about the electron scattering and capture processes inside the samples. The basic measurement is a resistivity measurement as function of temperature (T) and/or magnetic field (**B**). However, for two-dimensional gas samples. It is very hard to determine or even assign a thickness to the conducting layer. The sheet resistance is analogous to the resistivity but for two dimensions.

$$R_s = R\frac{W}{l} \qquad \textbf{(3.10)}$$

Here R_s is the sheet resistance (unit is Ω/□ or Ohm-per-square, to distinguish from resistance which has the same basic unit but a different meaning), R the measured resistance and W & *l* the width and length respectively of the current path. Such measurements allow for the extraction of the (mobile) carrier density,

$$R_s = \frac{1}{ne\mu} \qquad \textbf{(3.11)}$$

where *n* is the two-dimensional carrier density, e the electric charge of an electron and μ the electron mobility. All transport measurements were done using a Physical property measurement system (PPMS), Quantum Design, USA with a DC measurement. In general, this resulted in a current of the order 1-100 μA. Two different measurement geometries, Hall-bar and Van-der-Pauw, were used.

3.9 Van-der-Pauw geometry

In the Van-der-Pauw geometry [22] the contact leads are directly wire bonded to the sample. The wire bonding process itself cracks the surface and makes contact to the deeper layers. The resistance is then measured among these four metal electrodes in different combinations. **Figure 3.11** shows the typical location and labeling in the Van-der-Pauw geometry. The sheet resistance is numerically extracted from **Equation 3.12**. The advantage of this geometry is that the shape and size of the sample can be arbitrary, as long as it is homogeneous, both structurally and electronically. The Hall resistance is obtained at the same time by measuring $\frac{V_{BD}}{I_{AC}}$

$$1 = \exp\left(-\frac{\pi}{R_S}\frac{V_{AB}}{I_{DC}}\right) + \exp\left(-\frac{\pi}{R_S}\frac{V_{AD}}{I_{BC}}\right) \qquad \textbf{(3.12)}$$

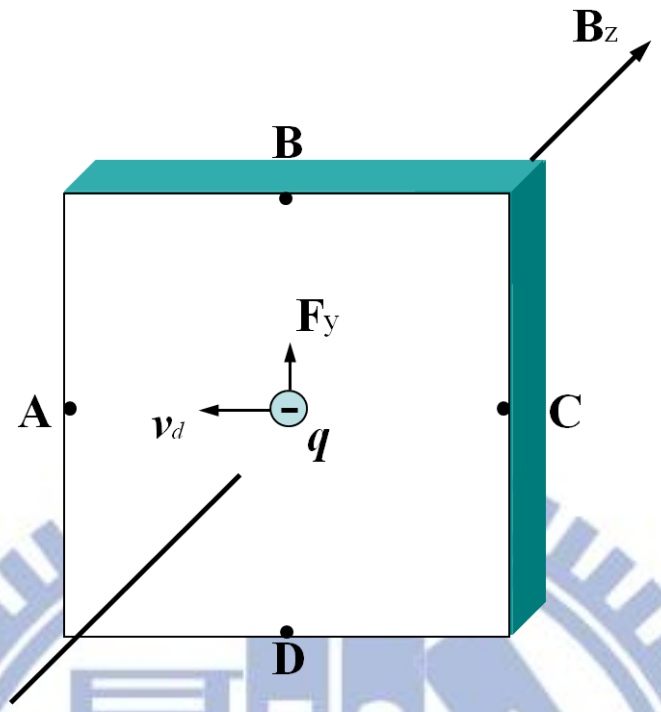

Figure 3.11: *Typical Van-der-Pauw geometry on a sample. Labels A to D indicated current and voltage contacts and was redrawn from Ref.[22].*

3.10 Treated substrate

As perovskite $SrTiO_3$ is composed of SrO- and TiO_2-alternative. The (100) surface can be terminated by either SrO- or TiO_2- domain. The surface physical and chemical properties must be greatly influenced by the surface morphology and the ratio of these two kinds of terminated domains. We can obtain the smooth TiO_2 plane by treating the $SrTiO_3$ (100) substrate with a buffered oxide Etch 6:1 (NH_4F–HF) solution. Because the HF etching removes Sr more efficiently than Ti, it seems that the etchant mostly attacks the Sr at the step edges, dissolving it and then removing Ti by lift-off, as shown in the processes as the following shown in **Figure 3.12.**

A $SrTiO_3$(100) substrate of 10x10x0.5 mm (Shinkosha Co., Japan) was first cleaned surface by using a 3-step sonication process in acetone, ethanol, DI water, and drying in a nitrogen stream. The second, the $SrTiO_3$ (100) was treated with a buffered oxide Etch 6:1 (NH_4F–HF) solution at room temperature for 7 minute. The treated $SrTiO_3$ was annealed in air at 1100^0C for 7 hour, and then cooling down to room temperature with cooling rate was 5^0C/m.

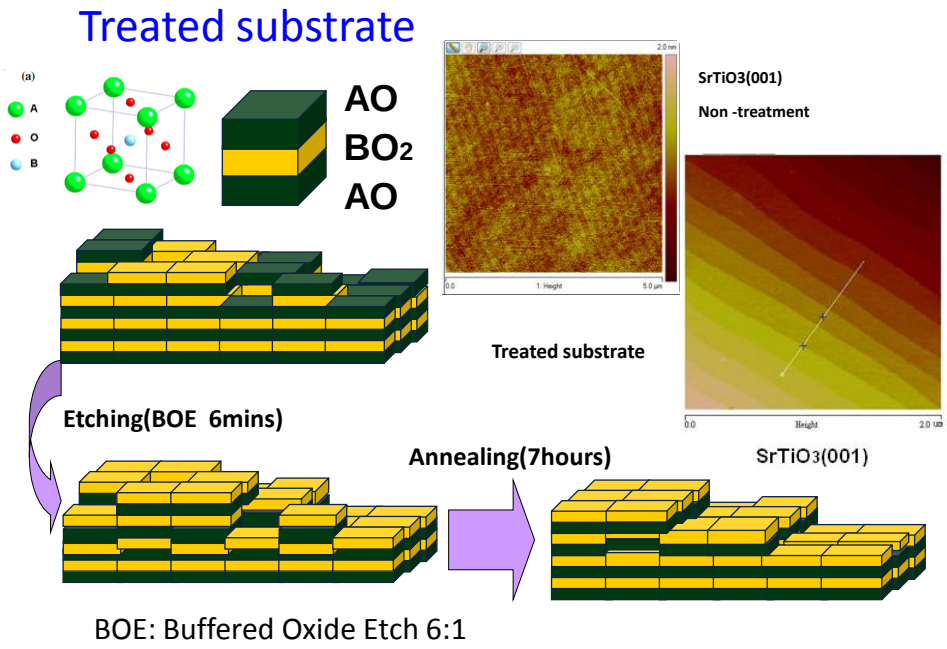

Figure 3.12 *Illustration of the substrate treatment processes to obtain the TiO_2- terminated on the surface of STO(100) substrate*

To conclude this chapeter, understanding the properties of a material system requires knowledge of the structure of the material, which is determined during the fabrication. All three parts, fabrication, characterization and functionality, require carefully paid attention and sophisticated techniques. It is this sequence - fabrication determines structure which in turn determines properties - that forms the basis of the research in this thesis. Pulsed laser deposition in combination with RHEED monitoring has become a mainstay of oxide thin film fabrication because of the tuneable growth kinetics and the ease of stoichiometric transfer. The use of single-terminated substrates allows for the growth of well- defined structures of complex oxides. Several techniques to characterize these structures, either available in-house or through collaborations with groups world-wide, have been discussed. Finally, techniques to measure the electrical and optical properties are necessary to be able to discuss the relation between these functional properties and the structural features.

References

[1] H. M. Smith, A. F. Turner, *Appl. Opt.* **1965**, *4*, 147.

[2] D. Dijkkamp, T. Venkatesan, X. D. Wu, S. A. Shareen, N. Jiswari, Y. H. Min- Lee, W. L. McLean, M.Croft, *Appl. Phys. Lett.* **1987**,*51*, 619.

[3] A. Ichimiya, P. I. Cohen, *Reflection High Energy Electron Diffraction*. Cambridge, UK, Cambridge University Press **2004**.

[4] D. B. Chrisey, G. K. Hubler, *Pulsed laser deposition of thin films*, New York, John Wiley and Sons **1994**, 55-85.

[5] D. Bauerle, *Laser processing and chemistry*, Berlin, Springer-Verlag **1996**, 3-62.

[6] D. B. Geohegan, *Laser Ablation: Mechanism and Application*, edited by Miller, J. C. and Haglund, R. F. Heidelberg, Springer **1991**, 28.

[7] J. Als-Nielsen, D. McMorrow, *Elements of Modern X-ray Physics*, Wiley **2001**; 1st edition, 107-195.

[8] B. Fultz, J. Howe, *Transmission electron microscopy and diffractometry of materials* Berlin; New York: Springer **2001**, 1-118.

[9] G. Binnig, C. F. Quate, Ch. Gerber, *Phys. Rev. Lett.* **1986**, *56*, 930.

[10] M. Alexe, A. Gruverman (Eds.), *Nanoscale Characterisation of Ferroelectric Materials. Scanning Probe Microscopy Approach*, Springer **2004**, 45-56.

[11] J. Tichý, J. Erhart, E. Kittinger, J. Přívratská, *Fundamentals of Piezoelectric Sensorics Mechanical*: *Dielectric, and Thermodynamical Properties of Piezoelectric Materials*, Springer; 1st edition **2010**, 1-53.

[12] R. C. Jaklevic, J. Lambe, A. H. Silver, J. E. Mercereau, *Phys. Rev. Lett.* **1964**, *12*, 159.

[13] B. D. Josephson, *Physics Lett.* **1962**,*1*, 251.

[14] P. W. Anderson, J. M. Rowell, *Phys. Rev. Lett.*, **1963**, *10*, 230.

[15] D. K. Bowen, B. K. Tanner, *High Resolution X-ray Diffractometry and Topography*, London ; Bristol, PA : Taylor & Francis **1998**, 50-170.

[16] J. E. Jones, *Proc. R. Soc. Lond. A* **1924**, *106*, 463.

[17] B. T. Thole, P. Carra, F. Sette, G. van der Laan, *Phys. Rev. Lett.* **1992**, *68*, 1943.

[18] J. Stohr et al., *Surf. Rev. Lett.* **1998**, *5*, 1297.

[19] S. Yamamoto, H. Kawata, H. Kitamura, M. Ando, N. Saki, N. Shiotani, *Phys. Rev. Lett.* **1988**, *62*, 2672.

[20] H. Onuki, N. Saito, T. Saito, *Appl. Phys. Lett.* **1988**, *52*, 173.

[21] Virendra Kumar Verma's Ph.D. thesis, Department of Physics, Faculty of Science & Graduate School of Science, the University of Tokyo

[22] L. J. Van der Pauw, *Philips Research Reports* **1958**, *13*, 1-9,

Chapter 4: Ferroelectric control of the conduction at the $LaAlO_3/SrTiO_3$ hetero-interface

4.1 Introduction

Complex oxide hetero-interfaces have emerged as one of the most exciting subjects in condensed-matter due to their unique physical properties and new possibilities for next-generation electronic devices [1, 2]. In the push for practical applications, it is desirable to have the ability to modulate the interface functionalities by external stimulus. In this study, we propose a generic approach by inserting a functional layer to the heterostructure to acquire the non-volatile control of the intriguing properties at oxide interfaces. The LAO/STO interface is served as a model system in which a highly mobile quasi-two dimensional electron gas (2DEG) forms between two band insulators [3,4] , exhibiting 2D superconductivity [5] and unusual magnetotransport properties [6]. Although a modulation of the carrier density and mobility of the LAO/STO interface was achieved by using electric field effect [7–9], it is essential to extend the control concepts to gain nonvolatile and reversible abilities for practical applications. Recently, the nonvolatile modification of the local conduction at the LAO/STO interface has been demonstrated by scanning probe techniques [10–12]. Several possible mechanisms have been proposed to explain this interesting behavior based on the electrostatic effects either attributed to induced ferroelectricity or surface charge [13,14]. In this study, we bring in a ferroelectric $Pb(Zr_{0.2}Ti_{0.8})O_3$ (PZT) layer nearby the LAO/STO interface. The ferroelectric polarization of PZT layer serves as a control parameter to modulate the 2DEG conducting behaviors. The as-grown polarization (P_{up} state) leads to charge depletion and consequently a low conduction. Switching the polarization direction (P_{down} state) results in a charge accumulation and enhances the conduction at the interface of LAO/STO. The origin of this modulation is attributed to a change in the electronic structure due to the ferroelectric polarization states, evidenced by x-ray photoelectron spectroscopy (XPS) and the cross-sectional scanning tunneling microscopy/spectroscopy (XSTM/S). Control of the conduction at this oxide interface suggests that the concept can be generalized for other oxide systems to design functional interfaces.

4.2. Experimental methods

4.2.1 Sample preparation

To realize the LAO/STO interface, a TiO_2–terminated STO (100) substrate were used for this study. An atomically smooth surface with clear unit cell (u.c.) – height steps was observed with atomic force microscopy (AFM). On the top of that LAO and PZT were grown by pulsed laser deposition with assisted high pressure RHEED. The substrate was heating to 850^0C and maintaining this temperature during the LAO growth at 2×10^{-5} Torr oxygen pressure. LAO thin films were grown successfully with the layer-by-layer growth mode as shown in **Figure 4.1** and the insert is the AFM image demonstrated that we can grow very high quality of LAO thin film on STO substrate.

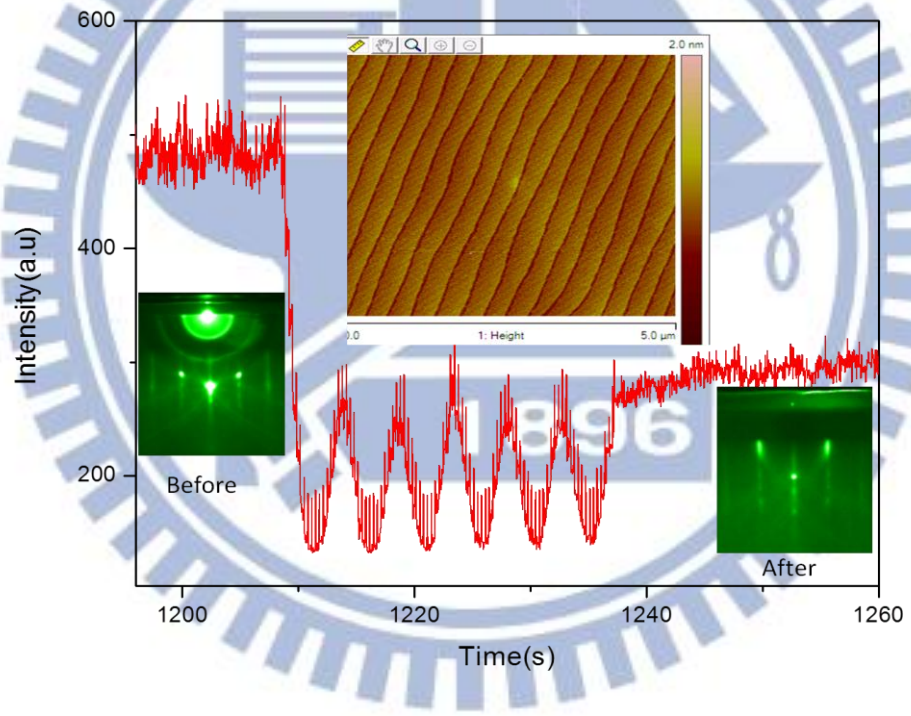

Figure 4.1 *RHEED oscillations for the growth control the LAO thickness (illustration for 6uc of LAO) by Laser MBE system. The insets show the RHEED patter at the beginning (before) and end (after) of the LAO growth (lover panel in the left and right) and also AFM image scanning for LAO 6uc on TiO_2- STO substrate (higher panel).*

After that, the samples were cooled down to 620^oC and oxygen pressure was tuned to be of 120 mTorr to start the growth of the PZT layer. After growth, the samples were annealed for 30mins and cooled down slowly to room temperature in an O_2 pressure of 600Torr.

4.2.2 Structural and electrical transport characterization

The x-ray diffraction techniques were employed to investigate the thin film structure. The θ-2θ scan and the asymmetry reciprocal space maps (RSMs) were performed using a synchrotron radiation source beamline BL-17A at the National Synchrotron Radiation Research Center (NSRRC) in Hsinchu, Taiwan. The incident beam was monochromated at 9.3KeV (~1.333Å) with Si (111) double crystal mirror and then focused by a toroidal focusing mirror to get higher intensity beam. Four sets of slits were used to gain the detection resolution, where two sets of slits were placed before samples to set beam size about 0.5 mm × 1 mm and the other two were placed after the sample (or before scintillation counter) to decrease background noises. These diffraction measurements were then plotted in the reciprocal lattice unit that is normalized to STO substrate (1 r.l.u.=$2\pi/a_{STO}$).

4.2.3 Transport measurement

In order to conduct the transport measurements, four square metallic (Au/Ti) electrodes (0.3 mm^2 size) connected to interface of LAO/STO were thermally evaporated on each of the PZT/LAO films by using IB Lithography. Then gold wires (0:002500 gauge) were manually bonded to the electrodes using silver paste. The samples were cooled by closed cycle refrigeration and the transport measurements were carried out in a PPMS (Quantum Design) system from the room temperature to 20K.

4.2.4 XSTM and XPS

For STM studies, the sample was cleaved in situ and measurements were performed from the cross-sectional geometry in an ultrahigh vacuum (UHV) chamber with a base pressure of ~ 5×10^{-11} Torr. In addition, scanning tunneling spectroscopy (STS) images were simultaneously acquired at ~ 100 K temperature. XPS spectra were collected at room temperature on a Thermo Scientific K-Alpha system, equipped with a monochromatized Al Kα x-ray source of 1486.6 eV. The C 1*s* signal at 284.6 eV was used as the energy reference to correct for charging. The standard deviation of the XPS peak position errors is about 16 meV, which is smaller than the step size of 50 meV used for the acquisition

4.3 Structural characterization

In order to realize this concept, the samples were prepared by pulsed laser deposition assisted with reflection high-energy electron diffraction (RHEED) (**Figure 4.2a)**). The details can be found in the method section. In order to ensure the quality of the samples, the crystallinity of the heterostructure was studied using x-ray diffraction techniques. The θ-2θ scan (**Figure 4.2b)**) and reciprocal space mapping (RSM, **Figure 4.2c)**) around the STO (103) diffraction peak of the typical heterostructure with 6 unit cells (u.c.) LAO and 20 nm PZT show that both PZT and LAO are grown epitaxially on the STO (001)-oriented substrates. In addition, 4-fold symmetry was also observed in STO, LAO, and PZT in the Φ-scan measurements, showing a cube-on-cube fashion (inset in **Figure 4.2c)**). By the scanning transmission electron microscope (STEM), the high-angle annular dark-field (HAADF) imaging of the heterostructure, **Figure 4.2d)**, firmly resolves the atomically sharp interfaces with the derived cube-on-cube epitaxial relationship, $[100]_{STO}(001)_{STO}\|[100]_{LAO}(001)_{LAO}\|[100]_{PZT}(001)_{PZT}$, nicely consistent with the X-ray results. Moreover, the ferroelectricity of the PZT layer on top of the interface was evidenced by the piezoresponse force microscopy (PFM) techniques. Only two contrasts can be observed in the mapping of piezoresponse signal. In **Figure 4.2e)**, the bright square corresponds to the downward-polarized (P_{down}) region, which was switched from upward-polarized (P_{up}) as-grown state by applying a DC bias of +8 V on the writing tip. Similarly, the small dark square inside the bright square was created by rewriting this region with a tip bias of -8 V. The phase difference of piezoresponse signal between upward- and downward-polarized states is 180°. As shown in **Figure 4.2f)**, the hysteresis behavior of the piezoresponse phase indicates the polarization of top ferroelectric PZT layers can be switched back and forth by an external bias.

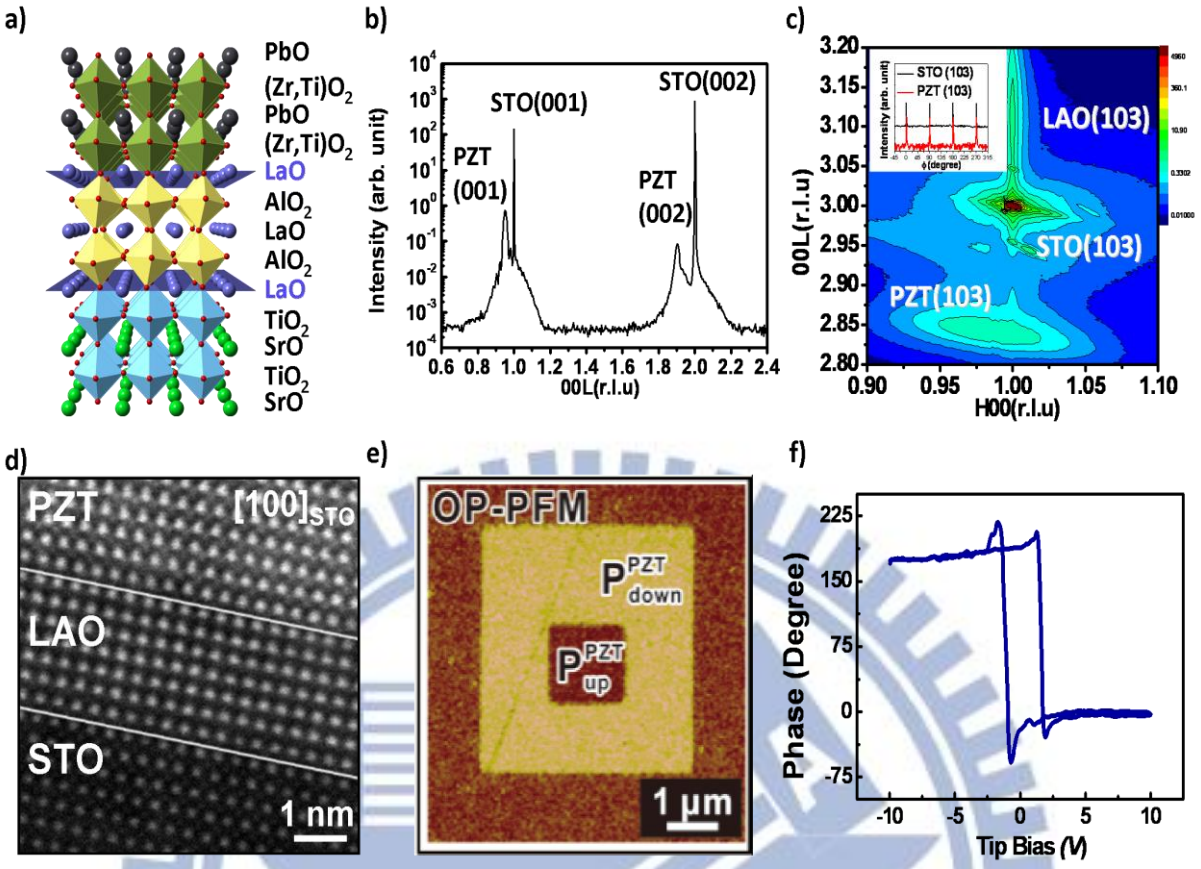

Figure 4.2 *The structural characterization;* **a)** *Grown and schematic model of the PZT/LAO/STO structure;* **b)** *XRD θ-2θ scans shows only the PZT (00L) peaks can be observed in the vicinity of STO peaks of the PZT/LAO/STO thin film;* **c)** *Off – normal Reciprocal space mapping (RSM) scan around the STO (103) peak. The LAO and PZT (103) peaks can be observed together with STO peak. The insert figure is the In -plane epitaxy revealed by Φ-scan of the thin film peaks are well aligned on our substrate;* **d)** *TEM investigation of the PZT20nm on top of LAO6uc/STO heterointerface, a high – resolution HAADF image showing an atomically sharp interface of both LAO and PZT films on TiO_2 –terminated STO substrate. The dimension of the scale bar is 1nm;* **e)** *Mechanically induced reversal of the ferroelectric polarization. The piezoresponse force microscopy (PFM) techniques shows that only two contrasts can be observed in the mapping of the piezoresponse signal and single – point PFM hysteresis loops of the PZT film on LAO/STO heterointerface in* **f).**

4.4 Transport measurements

In order to understand the influence of ferroelectricity on the LAO/STO interface experimentally, we firstly carried out electrical transport measurements on the heterostructure (**Figure 4.3a)**), in which the PZT layer with the spontaneous polarization P_{PZT} functions as the polarized dielectric slab to modulate the conduction of LAO/STO heterointerface. **Figure 4.3b)** shows the sheet resistance versus temperature (*R-T* curves) of the PZT/LAO/STO samples with various PZT layer thicknesses (0~40 nm), while the LAO thickness was fixed (6 u.c.). The R-T curves for these samples show that the sheet resistance at room temperature is low (~ 23 kΩ/sq) and decreases with temperature, showing the metallic behavior. For the samples with PZT on top, the ferroelectric effect sets in and the sheet resistance starts increasing with PZT thickness, showing the strong impact of the intrinsic polarization (P_{up}) of PZT on electron conduction at the interface. This is anticipated since the ferroelectric field effect provides one more degree of freedom to compensate the charge unbalance at the interface [15]. We also conducted transport measurements on the samples with different LAO thickness, while PZT thickness was kept constant (20 nm) (**Figure 4.3c)**). Several studies suggested a critical LAO thickness (4 u.c.) for the formation of 2DEG at this interface [7]. Under such circumstance, all the samples with LAO above a critical thickness behave like metal. The sheet resistance decreases when lowering the temperature and increases when the thickness of LAO is reduced. This resistance changes can be rationalized in the framework of polarity discontinuity, which leads to an abated built-in electric field when the LAO thickness is reduced. Based on the experimental results, we are able to estimate that the sheet resistance is increased by an order of magnitude when the LAO is decreased by 1 u.c. Moreover, the sheet resistance increases with the decreasing of gap thickness (*h*) is a qualitative agreement with our simulation result (shown in Supplemental **Figure C3**) which we also discuss details in theoretical support and discussion part.

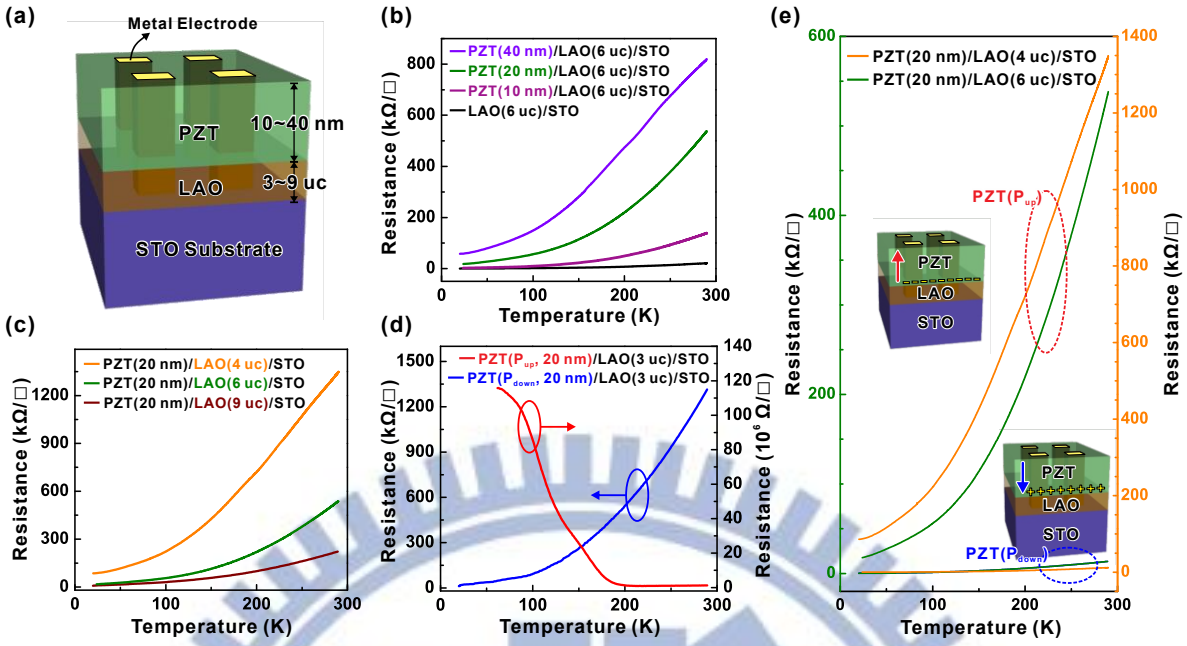

Figure 4.3 *Transport measurement of PZT/LAO/STO devices:* **a)** *Sketch of the samples and the contact configurations down to the LAO/STO interface by using the IB lithography method;* **b)** *Temperature dependence of the sheet resistance, Rs, of the PZT thickness dependence on n–type LAO/STO conducting interface;* **c)** *Influence of LAO thickness on the electronic properties of the PZT/LAO/STO devices while keeping the constant at 20nm of PZT on top of LAO/STO hetero-interface.* **d)** *Sheet resistance measured as a function of temperature for PZT 20nm/LAO 3uc/STO as grown with natural polarization (P_{up}) and after switching the polarization to down states (P_{down});* **e)** *Modulation of sheet resistance from high to low resistance states of two samples, PZT(20 nm)/LAO(6 uc)/STO and PZT(20 nm)/LAO(4 uc)/STO corresponding to natural polarization (P_{up}) and after switching (P_{down}), respectively.*

The transport measurements have provided a clear insight into the ferroelectric effect on the LAO/STO interface, and now a question is raised: can one modulate the interface conduction with the ferroelectricity? We have employed the scanning probe technique to switch the ferroelectric polarization of the samples. After switching ferroelectric polarization, bipolar-resistance behavior was observed in the PZT/LAO/STO devices. **Figure 4.3e)** shows the R-T curves of LAO (4 u.c.) and LAO (6 u.c.) after putting down PZT 20 nm with two different ferroelectric polarization directions on top of the 2DEG. The sheet resistance at the initial polarization state (P_{up}) is rather high. After flipping the polarization to an opposite direction (P_{down}), the sheet resistance became much lower. The sheet resistance modulating the conductivity at the LAO/STO interface with different polarization states of PZT can reach

more than two orders of magnitude difference for PZT (20 nm)/LAO (4 u.c.)/STO sample at room temperature. Another intriguing feature here is the switch of an insulating state to a conducting state. The PZT/LAO (3 u.c.)/STO typically shows insulating behavior. The switch of the polarization can change the transport behaviors from insulating to metallic, suggesting the nonvolatile control of metal-insulator transition with ferroelectricity (**Figure 4.3d)**). The transport measurements indicate that the ferroelectric field effects can not only modulate the conduction, and but also switch the conducting state and our results also can be switchable and repeatable as shown in **Figure 4.4**.

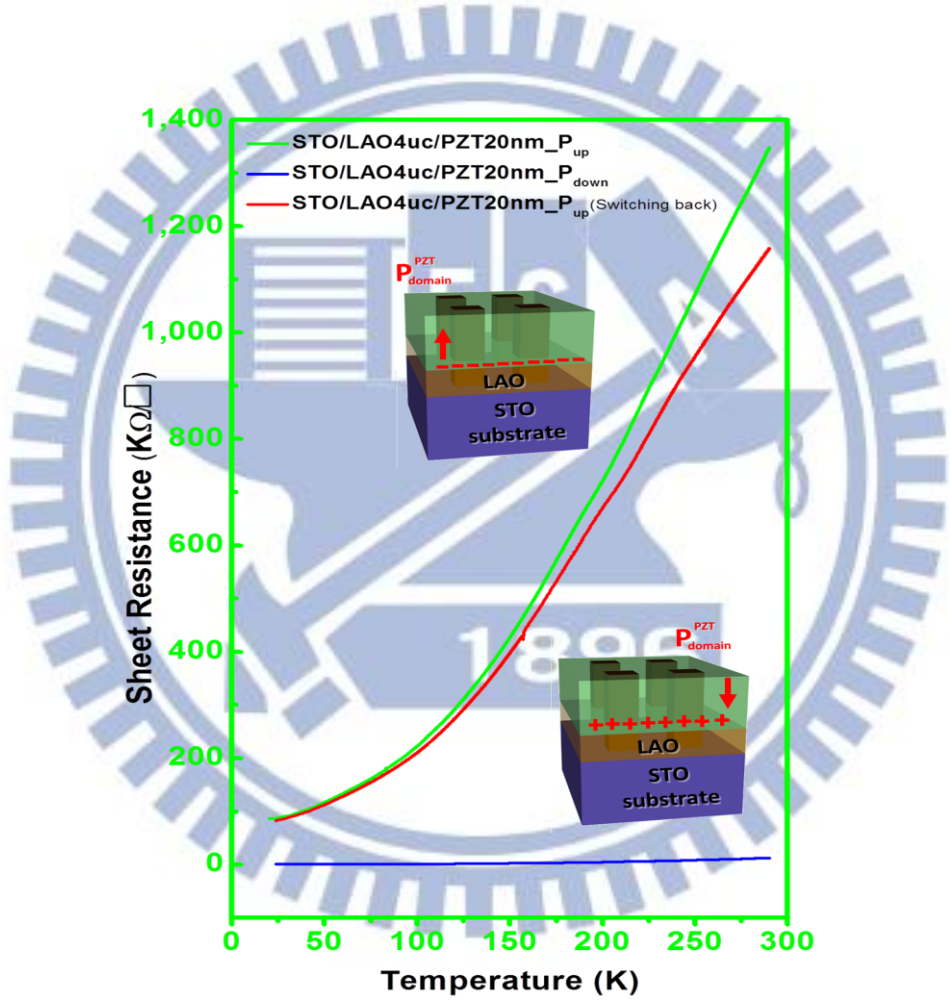

Figure 4.4 *The sheet resistance as a function of temperature measured for the as –grown device with nature polarization (upward -P_{up}) (green), Mechanically downward –switched the polarization (P_{down}- blue color) and reversal the polarization back to the original state (P_{up}- red color), then sheet resistance becomes high state again.*

4.5 X- Ray Photoemission Spectroscopy (XPS)

In order to understand the fundamental mechanism behind this intriguing behavior, it is crucial to investigate the ferroelectric manipulation of electronic structure at the LAO/STO heterointerface. Here, the ferroelectric-pattern assisted XPS was used to probe the reversible interfacial electrostatics and its affected electronic structures. In the ferroelectric PZT/LAO/STO heterointerface with a naturally upward PZT layer, the polarization was reversed by the scanning probe technique (probe voltage set to 8 V) to obtain a downward polarization area of about 1 mm^2 that is larger than x-ray beam size of about 400 μm^2. This ferroelectric-pattern assisted spectral technique makes us study the polarization reversal using the same sample. It implies that we do not have to compare the polarization states in two different samples and we can avoid all the discussions regarding sample quality and other differences. As depicted in **Figure 4.5a)**, positive (P_{down} state) and negative (P_{up} state) bound charge sheets at bottom PZT layer affected the conducting LAO/STO hetero-interface, leading to an accumulation or depletion of free electrons in STO layer. Consequently, in distinct ferroelectric patterns with reversed electric configuration, two interfacial capacitors having different electric fields inside were constructed separately in top sheet of positive bound charges and bottom sheet of negative mobile electrons. In previous studies, the binding energies of core-level photoelectrons emitted from the epitaxial thin films and substrate were particularly sensitive to probe the modulation of interfacial capacitor [16]. The schematics (**Figure 4.5a**) also shows the ferroelectric-pattern assisted XPS technique on PZT (3.5 nm)/LAO (4 u.c.)/STO heterointerface. The binding energy of the Sr core-level from buried layer thus decreases ($E_B^{Sr} - eV_{up}$) or increases ($E_B^{Sr} + eV_{up}$) depending on the downward and upward polarization directions, respectively, by comparing to the binding energy of the Sr core-level (E_B^{Sr}) from LAO/STO heterointerface. Evidently, the concept of the interface capacitor is also confirmed from the lack of change of the core-level emissions from the top PZT (Pb 4*f* core-level) and LAO (La 4*d* and Al 2*s* core-levels) layers. **Figure 4.5b)** shows the characteristic core-level photoelectron spectra in the ferroelectric PZT/LAO/STO and the conducting LAO/STO heterointerface samples. The binding energy of Sr $3d_{5/2}$ core-level shifts associated with the potential drops of the PZT-modulated LAO/STO interface capacitors were obtained at eV values of +0.15 eV (P_{up} state) and −0.1 eV (P_{down} state), and the core-level difference between Sr $3d_{5/2}$ and La $4d_{5/2}$ (ΔE_{CL}) were determined to be 31.15 eV (P_{up} state) and 30.90 eV (P_{down} state), respectively.

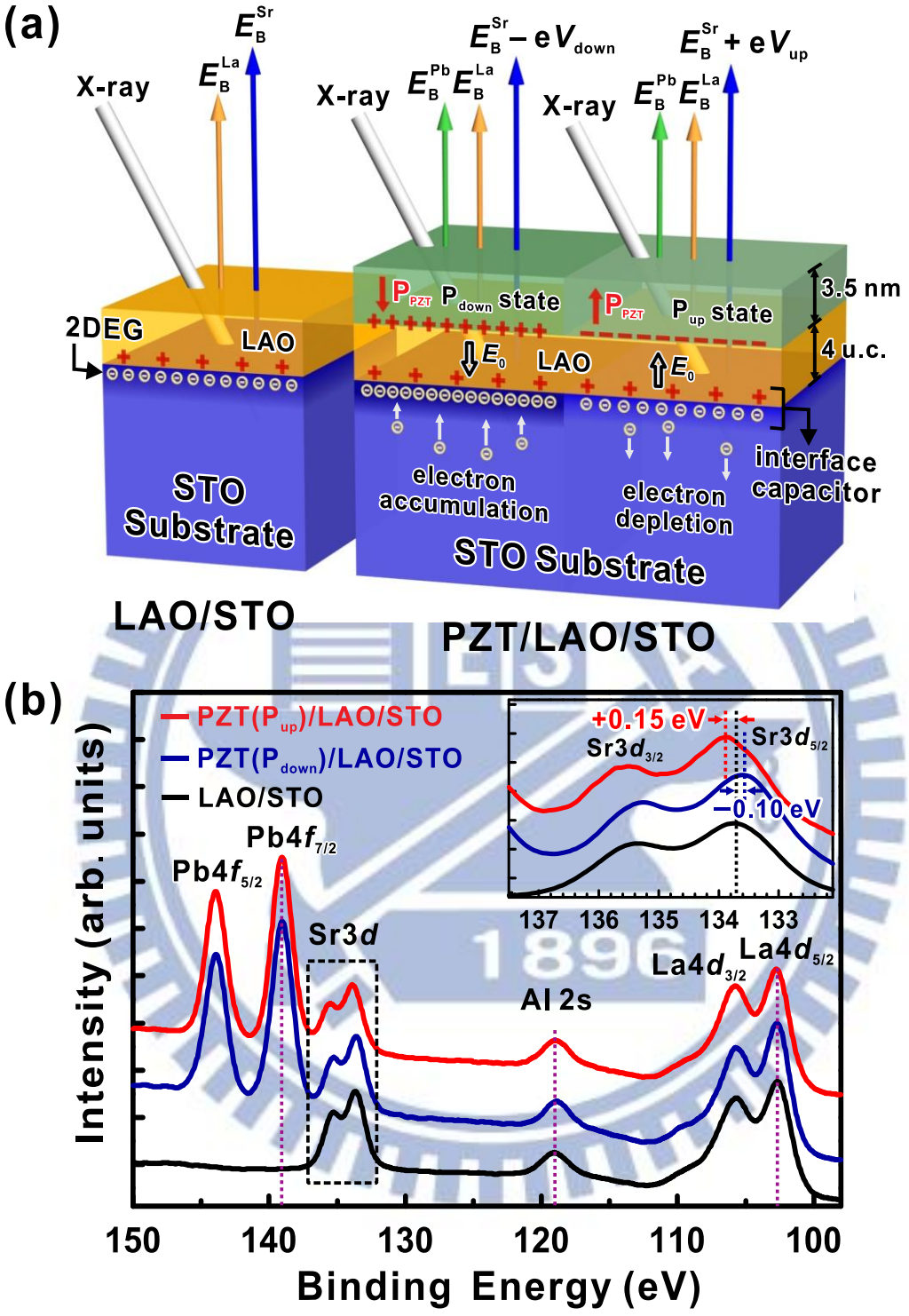

Figure 4.5 *X-ray Photoemission spectroscopy study on the upward / downward ferroelectric polarization PZT/LAO/STO and LAO/STO hetero-structure.* **a)** *Schematic illustration of the photoemission spectroscopy measurement on the upward (P_{up}) / downward (P_{down}) polarization of the PZT/LAO/STO, and the bare LAO/STO samples also included in the Figure. The Pb 4f, La 4d and Sr 3d (indicated by green, yellow and blue arrow) are captured from*

PZT, LAO and STO layers separately (indicated by green, yellow and blue block). **b)** *The XPS spectra taken from the PZT/LAO/STO and bare LAO/STO samples. The photoelectron peaks are aligned into the same energy level in the Pb4f and La4d (guided by red dashed line). But the Sr 3d core-level has significant binding energy downward shift from 0.15 to -0.1 eV when the P_{up} ferroelectric PZT switched to P_{down} (see inserted Figure).*

4.6 Cross – Sectional Scanning Tunneling Microscopy and Spectroscopy (XSTM/S)

The modulation of electronic structure of LAO/STO heterointerface by ferroelectric polarization is further elaborated by performing XSTM/S measurement on thick PZT top layer (20 nm) sample. The variations of the electronic structure across the heterointerface produce corresponding variations in the current-voltage behavior of STS measurements. Therefore, after keeping *in situ* cleaving sample in the STM chamber under a background pressure of less than $1x10^{-10}$ Torr and cooling it down to ~ 100 K, spatial-resolved STS based on XSTM image would reveal directly the electronic structure of the hetero-structures. **Figure 4.6a)** shows the XSTM image across the hetero-structured interface, and the color bars are used to indicate the positions where STS measurements were performed. The different regions of Nb-STO, STO, LAO, and PZT layers were identified from the tunneling current image which reveals specific electronic characteristics of each layer. **Figures 4.6b)** and **4.6c)** show the evolution of the electronic structures of LAO from the position near the STO side (N), the middle side of LAO (M), to the position away from STO (A) in the naturally P_{up} and poled P_{down} samples, respectively. In the STS results, to exclude the effects of surface and gap states in LAO and STO layers which disturbing band edge determination [17], the current offsets larger than 0.2 A at negative/positive sample biases are indicated as the energetic positions of the valence band maximum (VBM) and conduction band minimum (CBM). Therefore, the comparison of the energy shifts of the band edges can be referred to not only the value of the electric field in LAO but also the energetic shift across the interface from STO to LAO. As shown in **Figure 4.6b)** and **4.6c)**, the energy shift of the band edges in LAO is smaller for the P_{down}-state sample than that for the P_{up}-state sample, indicating that the electric field in LAO layer diminishes after the polarization of PZT is switched from the natural P_{up} state to the P_{down} state. Furthermore, according to the energy shifts between STO and LAO, as shown in **Figures 4.6d)** and **4.6e)**, the suppressed electric field in LAO corresponds to the increase of valence band

offset (VBO) value from ~0.5 eV (P_{up}) to ~1.0 eV (P_{down}) of LAO/STO electronic structure. To compare with the XPS measurements of heterojunction as shown above, we measured the energy difference between the characteristic core level and the VBM of each layer is a material constant, and the polarization switching induced Sr core-level shift is thus related directly to the VBO change of LAO/STO heterostructure. Therefore, the VBO variation to the LAO/STO modulated by a thin PZT layer (3.5 nm) is obtained by XPS of about 0.25 eV, which is smaller than that of LAO/STO capped with thick PZT (20 nm) of ~0.5 eV obtained by STS. In both ferroelectric-pattern assisted spectral results, we find that the presence of up- and down-polarized PZT layers would induce additional interface electrostatics and eventually lead to the VBO change of LAO/STO heterostructure. The change of VBO depends on the thickness of top-capped PZT layer, which is from 3.5 nm to 20 nm (with a wide polarization range from 11 $\mu C/cm^2$ to above 100 $\mu C/cm^2$ reported in defect-free films) [18–21], leading to an increase from 0.25 eV to 0.5 eV, and the response of VBO change on ferroelectric polarization switching is consistent (P_{up} PZT increases VBO value of LAO/STO and is contrary to P_{down} PZT).

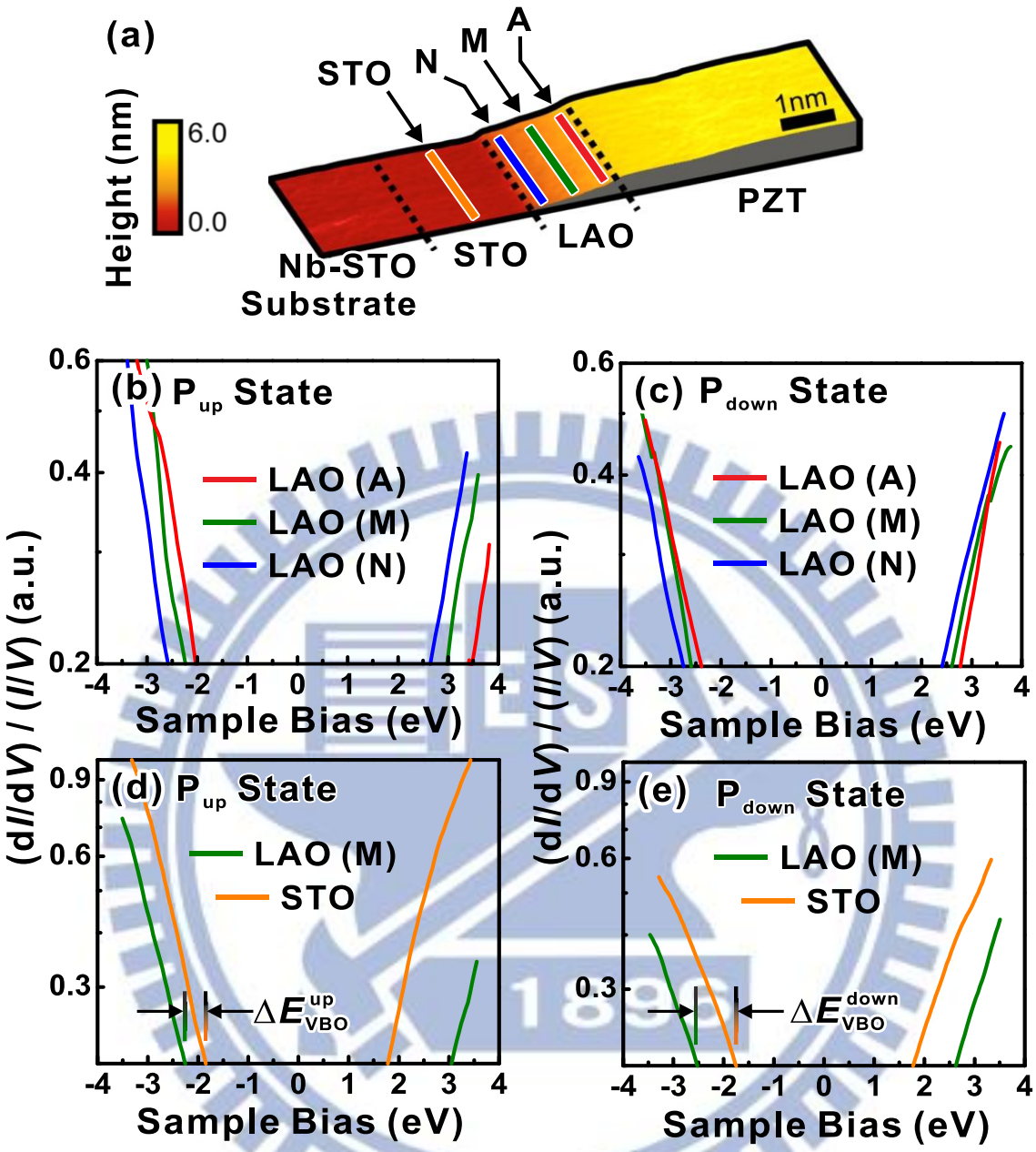

Figure 4.6 **a)** *A typical cross-sectional constant current STM image of the epitaxial PZT/LAO/STO hetero-structure. The spatial spectroscopic measurements on LAO surfaces of PZT/LAO/STO systems for the* **b)** *upward-polarized (P_{up}) and* **c)** *downward-polarized (P_{down}) situation in PZT films from the position near the STO side (N), the middle side of LAO (M), to the position away from STO (A). The average spatial spectroscopic measurements on LAO (green curve), and STO (orange curve) surfaces for the* **d)** *upward-polarized (P_{up}) and* **e)** *downward-polarized (P_{down}) situation in PZT films.*

4.7 Theoretical support and discussions

To exploring the phenomena of ferroelectric of PZT at the LAO/STO interface associated with its band structure, we studied the E_c band bending (invert electronic potential bending), bound and free charge concentration, and the electronic conductivity inside the effective length of STO layer under P_{up} and P_{down} states of PZT by using phase-field approach. Firstly, the static profiles of potential and electrons within STO layer in the absence of PZT polarization were obtained by solving the following coupled equations to steady state,

$$\nabla^2\psi = -\frac{\rho}{\varepsilon_0\varepsilon_r} = \frac{e_0 n}{\varepsilon_0\varepsilon_r} \quad \textbf{(4.1)}$$

$$\frac{\partial n}{\partial t} = -\nabla \bullet J = D\nabla^2 n - \mu\nabla \bullet \left(n\nabla\psi\right) \quad \textbf{(4.2)}$$

in which ψ is the electric potential, r is the charge density, e_0 is the unit charge, n is the electron concentration, ε_0 is the vacuum permittivity and ε_r is the dielectric constant of STO. D and μ stand for the diffusivity and mobility of electrons in STO respectively. It is seen that the band bending at the STO/LAO interface (without PZT layer on top) is about 0.3 eV, which causes electron accumulation at the interface (shown in **Figure 4.7a)**).

In the presence of PZT polarization, the bound charge induced by the polarization and electric potential drop at the PZT/LAO interface are estimated by introducing $\rho = -\nabla \bullet P$. At the PZT/LAO interface, where the polarization reduces to 0, a negative bound charge sheet is formed in the case of P_{up} polarization in PZT layer. Based on the Poisson equation,

$$\nabla^2\psi = \frac{\nabla \bullet P_i}{\varepsilon_0\varepsilon_r}, \quad \textbf{(4.3)}$$

The electric potential drop at the PZT/LAO interface due to the PZT P_{down} bound charge is calculated to be about −0.5 V. Since electric potential should be continuous throughout the heterostructure, the potential decrease through the STO and LAO should be equal to the potential drop at the PZT/LAO interface. In addition, the effective length within STO is about 0.8 nm while the thickness of the LAO layer is about 1.1 nm. The potential drop at the LAO/STO interface can be estimated by the following equation,

$$\Delta V_{total} = \Delta V_{STO/LAO} + \Delta V_{LAO} = \left(\frac{a_{STO}^{eff}}{a_{STO}^{eff} + a_{LAO}}\right)\Delta V_{total} + \left(\frac{a_{LAO}}{a_{STO}^{eff} + a_{LAO}}\right)\Delta V_{total} \quad \textbf{(4.4)}$$

in which $\Delta V_{STO/LAO}$ and ΔV_{LAO} stand for potential drop at the interface and inside LAO

respectively. a_{STO}^{eff} and a_{LAO} are the effective length within STO and thickness of LAO respectively. Therefore, in the case of P_{up} polarization in PZT layer, the potential decreases by 0.2 V at the LAO/STO interface, and thus interface E_C band bending decreases from −0.3 eV to −0.1 eV. On the contrary, when the PZT polarization is P_{down}, a positive sheet of bound charges is formed at the PZT/LAO interface, which increases the local potential at the PZT/LAO interface and leads to the increase of the E_C band bending at the LAO/STO interface from −0.3 eV to −0.5 eV (shown in **Figure 4.7a)**).

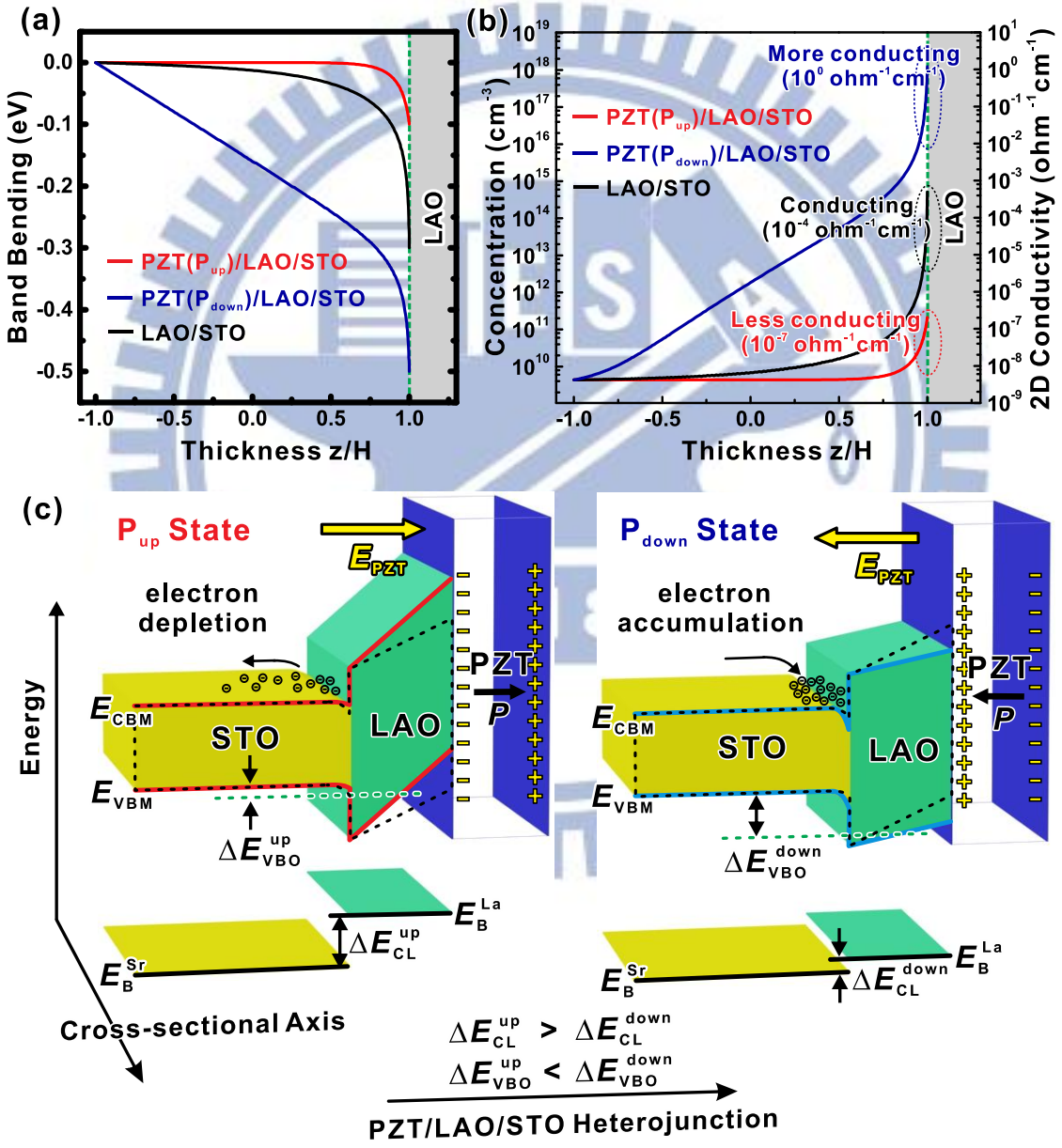

Figure 4.7 *E_c band bending* **a)**, *electron concentration and local electronic conductivity* **b)** *in STO layer in the presence of upward polarization, no polarization and downward polarization in PZT layer (z denotes the position in the STO layer, H is half of the layer thickness, so that*

z/H from -1 to +1 represents the entire layer). **c)** *Schematic band diagrams of a PZT/LAO/STO heterointerface derived from ferroelectric-pattern assisted XPS and XSTM/S measurements. The sheet of negative/positive bound charges at bottom PZT and its induced E-field (E_{PZT}) across the LAO layer would directly affect the mobile charges depletion/accumulation at the LAO/STO heterointerface, which are shown for both polarization states (P_{up} and P_{down}) of PZT layer. Decrease and increase potential buildups across LAO layer corresponded to different polarization states are indicated. Combining both XPS and STS spectroscopic results, the changes in valence band offset (ΔE_{VBO}) and core-level energetic separation (ΔE_{CL}) between LAO and STO layers are revealed, and construct a ferroelectricity modulated LAO/STO band structure model.*

Furthermore, the electron concentration and the electronic conductivity inside the effective length of STO layer have been calculated and summarized in **Figure 4.7b)**. Clearly, the polarization in PZT layer has a significant effect on the electron concentration and conductivity σ in the STO side of LAO/STO interface, where the electronic conductivity is calculated by $\sigma = ne_0\mu$. The electron concentration away from the LAO/STO interface region is ~10^9 cm^{-3}. When the ferroelectric polarization inside PZT layer is down (P_{down}), the electron accumulation significantly reaches up to 10^{18} cm^{-3} with band bending of ~0.5 eV in the vicinity of LAO/STO interface. Furthermore, the local conductivity is calculated to be ~10^0 $\Omega^{-1}cm^{-1}$, indicating that the interface becomes more conducting (**Figure 4.7b)**). The electron accumulation is strongly inhibited (~10^{11} cm^{-3}) when the polarization in PZT layer is P_{up}, with interface band bending of 0.1 eV. In this case the interface becomes less conducting with local conductivity of ~10^{-7} $\Omega^{-1}cm^{-1}$.

Based on the phase-field modeling results, which agree well with the experimental observations of ferroelectric-pattern assisted transport measurements, XPS and XSTS spectra, we display the mechanism of ferroelectric modulation of LAO/STO conductivity in **Figure 4.7c)**. In the case of naturally P_{up} state of capped PZT, because the PZT bottom has negative polarization charge sheet, the potential buildup in the polar LAO layer increases and the free electrons are repelled from the LAO/STO interface (electron depletion), where the interface band bending of STO side decreases with smaller VBO value and makes ΔE_{CL} larger. As the polarization switching to P_{down} state, the positive polarization charge sheet at PZT bottom makes the LAO potential buildup decreases and attracts more free electrons at the LAO/STO interface (electron accumulation), where the interface band bending of LAO side increases

with larger VBO value and smaller ΔE_{CL}. In addition, for the LAO/STO heterostructure with thinner LAO layer (3 u.c.), the variation of electric potential induced by E_{PZT} can be estimated to be about 1.0 eV, in which the thickness of the LAO layer is about 1.1 nm (3 u.c.) and the stray electric field in LAO layer is estimated to be about 10^9 V/m, as shown in the **Figure B1b**. This 1.0 eV potential variation is three times larger than the built-in potential variation (about 0.3 eV) from metal-insulator transition proposed in previous results [7,21–22]. Therefore, owing to a reversible polarization of top ferroelectric layer, the PZT/LAO/STO system is expected to be the one closest to having nonvolatile switching on/off characteristics at LAO/STO interface.

Moreover, in the calculation results, the change of band bending at the LAO/STO interface modulated by PZT layer from P_{up} state to P_{down} state is around 0.4 eV (**Figure 4.7a)**), which results in more conducting at the interface and having a conductivity ratio of about 10^7 (**Figure 4.7b)**). In the transport results shown in **Figure 4.3**, from PZT P_{up} state to P_{down} state, the conductivity ratio was experimentally obtained of about 10^3 in PZT (20 nm)/LAO (3 u.c.)/STO sample (**Figure 4.3d)**), which reveals PZT induced switching on/off capability at LAO/STO. However, based on the numerical calculation, a local conductivity ratio of 10^3 corresponds to a band bending change of 0.2 eV. This change value is smaller than the band offset shifts obtained by STM of about 0.5 eV, which is shown in **Figure 4.6** with the same PZT thickness of 20 nm. The differences in band edge shifts and conductivity ratio (from P_{up} to P_{down}) by comparing experimental and theoretical results can be attributed to the spatial resolution limit in XPS and XSTM measurements and the simplified bound/free charge modeling at PZT/LAO and LAO/STO interfaces. Here, the changes in band bending profile at the interface were evaluated by monitoring the changes in VBO. The variation of band bending value at the interface is supposed to be smaller than the VBO shift, due to the free carriers at the LAO/STO interface that would compensate polarization field effects. Additionally, in the theoretical calculation, the partially compensations at PZT/LAO and LAO/STO intetrfaces are set to zero to simplify the modeling. This makes the theoritical predications in the electric potential, the band bending, and the resistivity ratio larger than the experimental results.

4.8 Conclusion

In conclusion, we have demonstrated that the ferroelectric polarization can tune and modulate the conduction at the LAO/STO heterointerface. The XPS and XSTM/S results reveal the electrostatic predictions of the conducting state modulation, demonstrate the possibility of nonvolatile control, and provide compelling evidence in favor of ferroelectric doping at the conducting polar-nonpolar oxide heterointerface.

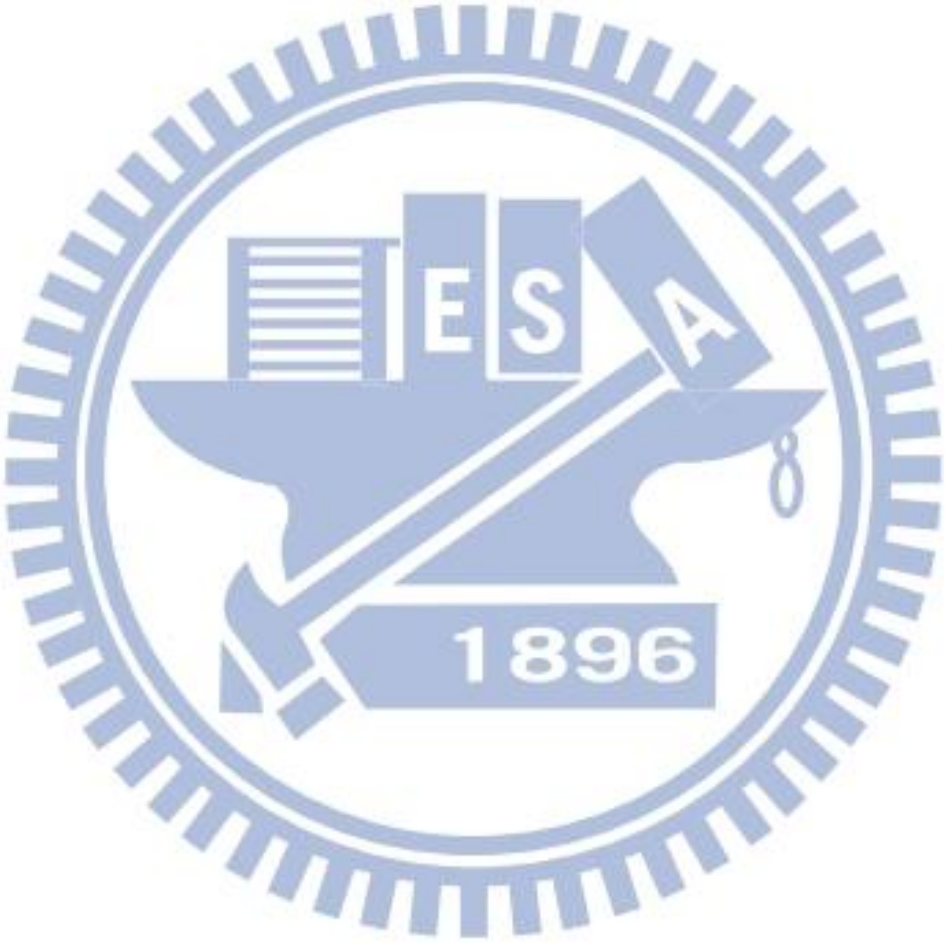

References

[1] H. Y. Hwang, Y. Iwasa, M. Kawasaki, B. Keimer, N. Nagaosa, Y. Tokura, *Nature Mater.* **2012**, *11*, 103–113.

[2] P. Zubko, S. Gariglio, M. Gabay, P. Ghosez, J. -M. Triscone, *Annual Rev. Condens. Matt. Phys.* **2011**, *2*, 141–165.

[3] A. Ohtomo, H. Y. Hwang, *Nature* **2004**, *427*, 423–426.

[4] N. Nakagawa, H. Y. Hwang, D. A. Muller, *Nature Mater.* **2006**, *5*, 204–209.

[5] N. Reyren, S. Thiel, A. D. Caviglia, L. F. Kourkoutis, G. Hammerl, C. Richter, C. W. Schneider, T. Koop, A. -S. Rüetschi, D. Jaccard, M. Gabay, D.A. Muller, J. -M. Triscone, J. Mannhart, *Science* **2007**, *317*, 1196–1199.

[6] A. Brinkman, M. Huijben, M. van Zalk, J. Huijben, U. Zeitler, J. C. Maan, W. G. van der Wiel, G. Rijnders, D. H. A. Blank, H. Hilgenkamp, *Nature Mater.* **2007**, *6*, 493–496.

[7] S. Thiel, G. Hammerl, A. Schmehl, C. W. Schneider, J. Mannhart, *Science* **2006**, *313*, 1942–1945.

[8] A. D. Caviglia, S. Gariglio, N. Reyren, N. Jaccard, T. Schneider, M. Gabay, S. Thiel, G. Hammerl, J. Mannhart, J. -M. Triscone, *Nature* **2008**, *456*, 624–627.

[9] G. Singh–Bhalla, C. Bell, J. Ravichandran, W. Siemons, Y. Hikita, S. Salahuddin, A. F. Hebard, H. Y. Hwang, R. Ramesh, *Nature Phys.* **2011**, *7*, 80–86.

[10] G. Cheng, P. F. Siles, F.Bi, C. Cen, D. F. Bogorin, C. W. Bark, C. M. Folkman, J. -W. Park, C. -B. Eom, G. Medeiros – Ribeiro, J. Levy, *Nature Nanotech.* **2011**, *6*, 343–347.

[11] Y. Xie, C. Bell, T. Yajima, Y. Hikita, H. Y. Hwang, *Nano Lett.* **2010**, *10*, 2588–2591.

[12] C. Cen, S. Thiel, G. Hammerl, C. W. Schneider, K. E. Andersen, C. S. Hellberg, J. Mannhart, J. Levy, *Nature Mater.* **2007**, *7*, 298–302.

[13] C. W. Bark, P. Sharma, Y. Wang, S. H. Baek, S. Lee, S. Ryu, C. M. Folkman, T. R. Paudel, A. Kumar, S. V. Kalinin, A. Sokolov, E. Y. Tsymbal, M. S. Rzchowski, A. Gruverman, C. B. Eom, *Nano Lett.* **2012**, *12*, 1765 -1771.

[14] F. Bi, D. F. Bogorin, C. Cen, C. W. Bark, J. -W. Park, C. -B. Eom, J. Levy, *Appl. Phys. Lett.* **2010**, *97*, 173110.

[15] P. Yu, W. Luo, D. Yi, J. X. Zhang, M. D. Rossell, C. -H. Yang, L. You, G. Singh–Bhalla, S. Y. Yang, Q. He, Q. M. Ramasse, R. Erni, L. W. Martin, Y. H. Chu, S. T. Pantelides, S. J. Pennycook, R. Ramesh, *Proceedings of the National Academy of Sciences of the United States of America* **2012**, *109*, 9710–9715.

[16] C. L. Wu, P. W. Lee, Y. C. Chen, L. Y. Chang, C. H. Chen, C. W. Liang, P. Yu, Q. He, R. Ramesh, Y. H. Chu, *Phys. Rev. B* **2011**, *83*, 020103-1-4 (R).

[17] B. C. Huang, Y. P. Chiu, P. C. Huang, W. C. Wang, V. T. Tra, J. C. Yang, Q. He, J. Y. Lin, C. S. Chang, Y. H. Chu, *Phys. Rev. Lett.* **2012**, *109*, 246807.

[18] V. Nagarajan, J. Junquera, J. Q. He, C. L. Jia, R. Waser, K. Lee, Y. K. Kim, S. Baik, T. Zhao, R. Ramesh, Ph. Ghosez, K. M. Rabe, *J. Appl. Phys.* **2006,** *100*, 051609.

[19] I. Vrejoiu, G. Le Rhun, L. Pintilie, D. Hesse, M. Alexe, U. Gösele, *Adv. Mater.* **2006**, *18*, 1657–1661.

[20] C. -L. Jia, V. Nagarajan, J. -Q. He, L. Houben, T. Zhao, R. Ramesh, K. Urban, R. Waser, *Nature Mater.* **2007**, *6*, 64–69.

[21] Y. Segal, J. H. Ngai, J. W. Reiner, F. J. Walker, C. H. Ahn, *Phys. Rev. B* **2009**, *80*, 4–7.

[22] J. W. Park, D. F. Bogorin, C. Cen, D. A. Felker, Y. Zhang, C. T. Nelson, C. W. Bark, C. M. Folkman, X. Q. Pan, M. S. Rzchowski, J. Levy, C. B. Eom, *Nature Commun.* **2010**, *1*, 94.

Chapter 5: Termination Control of Charge Transfer in $YBa_2Cu_3O_{7-x}$/ $La_{0.7}Ca_{0.3}MnO_3$ heterostructures

5.1. Introduction

Heterointerfaces between strongly correlated electron systems hold promise for the creation of new multifunctional properties that could not be realized by single-phase bulk materials [1]. The interplay of lattice, orbital, charge, and spin degrees of freedom at the interface has resulted in a number of exciting discoveries, including the observation of a 2-D electron gas-like behavior at $LaAlO_3$-$SrTiO_3$ (STO) interfaces [2, 3], the emergence of ferromagnetism in a superconducting material at the $YBa_2Cu_3O_{7-x}/La_{0.7}Ca_{0.3}MnO_3$ interface [4,5], and an induced ferromagnetic state in a heterointerface between $BiFeO_3$ and $La_{0.7}Sr_{0.3}MnO_3$ layers [6,7]. The $YBa_2Cu_3O_{7-x}/La_{0.7}Ca_{0.3}MnO_3$ interface has been intensively studied for the proximity effect of the ferromagnets (F)/superconductors (S) heterostructure [4,5,8,9,10]. Previous work has concluded that the Cooper pairs of the superconductor may enter the ferromagnet (i.e., proximity effect) and the spin of the ferromagnet may enter the superconductor in this F/S heterostructure. The competition between the ferromagnetic order and the superconducting order eventually results in suppression of both transition temperatures [11,12,13,14]. These effects are of topical interest for potential application in superconductive and magnetoresistant memory devices. Surprisingly, one key question has yet to be addressed in this prominent $YBa_2Cu_3O_{7-x}/La_{0.7}Ca_{0.3}MnO_3$ system: does termination type play an important role in determining the superconducting and magnetic properties? In this work, we managed to control two different terminations for $YBa_2Cu_3O_{7-x}/La_{0.7}Ca_{0.3}MnO_3$ interfaces. Samples with each termination type show distinct superconductivity and magnetism properties together with different valence states of Mn. Unexpectedly, atomically precise control of this interface enabled us to identify a new mechanism of charge transfer in the $YBa_2Cu_3O_{7-x}/La_{0.7}Ca_{0.3}MnO_3$ hetrostructures. This charge transfer mechanism is vital to the physical properties of the $YBa_2Cu_3O_{7-x}/La_{0.7}Ca_{0.3}MnO_3$ hetrostructures.

5.1.1 Review on Proximity Effects in LCMO/YBCO Heterostructures

Some of experimental and theoretical studies have been published on LCMO/YBCO heterostructures. However, a limited section of them is mainly discussed here in order to introduce some key concepts that are used later in this work to explain our model.

First of all, P. Fulde, R.A. Ferrell, A.I. Larkin and Y.N. Ovchinnikov presented a theory

for a superconductor in the presence of a strong, spatially homogeneous magnetic exchange field **H** [15,16]. Their model is based on the Bardeen – Cooper – Schrieffer (BCS) theory [17], where the electrons are form so-called Cooper pairs. These quasi-particles consist of two electrons which are spin singlets and have equal energy E_F (Fermi energy), but posses opposite momentum $\left(k_F^{\uparrow} = -k_F^{\downarrow}\right)$. Therefore, the total momentum of the Cooper pair vanishes: $\left(k_{Cooper} = k_F^{\uparrow} + k_F^{\downarrow} = 0\right)$.

The Zeeman splitting ΔE_{ex} of the energies corresponding to the spin down and spin up electron states has been exhibited under the presence of a ferromagnetic exchange field, **H.** Subsequently, the properties of the Cooper pairs become modified: Although, electrons remained the same energy E_F, but the momentum of the spin up electron is just $k_{1/2\Delta E_{ex}}$, while the one of the spin down electron is increased by $k_{1/2\Delta E_{ex}}$. Since the momentums of electron directions are opposite, the Cooper pairs obtain a finite momentum given by $k_{Cooper} = 2k_{1/2\Delta E_{ex}}$. Due to this momentum, the superconducting order parameter becomes spatially modulated on a length scale of $\frac{2\pi}{k_{Cooper}}$. Thus, spatially inhomogeneous states can be expected in LCMO/YBCO heterostructures.

Second, Z. Radovi´c et al. predicted an oscillatory dependence of the superconducting transition temperature T_{sc} on the ferromagnetic layer of thickness d_{FM} [18, 19]. In that case, the characteristic length scale over which the superconducting order parameter decays into that of the ferromagnet is given by

$$\xi_{FM} = \sqrt{\frac{4\hbar D_{FM}}{\Delta E_{ex}}} \qquad \textbf{(5.1)}$$

where D_{FM} is the diffusion coefficient in the ferromagnet and ΔE_{ex} the exchange energy of the ferromagnet (Zeeman splitting of the spin up and spin down conduction band's energies due to the magnetic exchange field **H**). Because the exchange energy favours one of the spin orientations, it acts as a pair breaker for the spin singlet of the Cooper pairs and reduces the value of ξ_{FM}. In a normal metal, where there is no such exchange energy, the corresponding length scale over which the superconducting order parameter decays is provided by

$$\xi_N = \sqrt{\frac{\hbar D_N}{2\pi k_B T}} \qquad \textbf{(5.2)}$$

where D_N is the diffusion coefficient in the normal metal.

In the theoretical study of Z. Radovi´c et al., the superconducting order parameter is also assumed to be depressed on the superconductor side of the interface. For the bulk superconductor, this characteristic length scale is given by

$$\xi_{sc0} = \sqrt{\frac{\hbar D_{sc}}{2\pi k_B T_{sc0}}} \qquad \textbf{(5.3)}$$

where D_{sc} is the diffusion coefficient in the superconductor and T_{sc0} is the transition temperature. Since the T_{sc0} will be reduced in a thin layer in proximity to ferromagnetism, Z. Radovi´c et al. used a corresponding length scale ξ_{sc} which depends on the reduced transition temperature T_{sc}^{red} :

$$\xi_{sc} = \sqrt{\frac{\hbar D_{sc}}{2\pi k_B T_{sc}^{red}}} \qquad \textbf{(5.4)}$$

The value of ξ_{sc} is thus larger than that of ξ_{sc0}. It gives a lower limit below which no superconductivity occurs: T_{sc}^{red} vanishes if the thickness of the superconductor d_{sc} is smaller than twice the length ξ_{sc} over which the superconducting order parameter changes $\left(d_{sc} < 2\xi_{sc}\right)$. In the opposite case, T_{sc}^{red} is finite. If T_{sc}^{red} is finite and the ferromagnetic layer thickness is of the same order as the coherence length of the superconducting order parameter in the ferromagnetic layer $\left(d_{FM} / \xi_{FM} \approx 1\right)$, an oscillatory behaviour of T_{sc}^{red} is expected in superconductor / ferromagnet / superconductor heterostructures: In the limit of $d_{FM} < \xi_{FM}$, the phase of the superconducting order parameter remains the same in the two superconducting layers. In this limit, the exchange energy ΔE_{ex} acting on the superconductor increases with increasing d_{FM}. Therefore, T_{sc}^{red} decreases with increasing d_{FM}. If d_{FM} is about the same as ξ_{FM}, it becomes more favourable for the superconducting order parameter to introduce a π-phase shift from one superconducting layer to the next one. This reduces the pair-breaking effect of the exchange energy ΔE_{ex} on the superconducting order parameter. Therefore, T_{sc}^{red} is enhanced even though the thickness of the ferromagnetic layer has been increased. With further increase in d_{FM}, T_{sc}^{red} will again be reduced, as the phase of the superconducting order parameter changes over a length scale of ξ_{FM}. This oscillatory behaviour of T_{sc}^{red} as a function of d_{FM} has been confirmed in several experiments on LCMO/YBCO heterostructures based on conventional, non-oxide materials [20, 21, 22].

Third, I. Baladi´e and A.I. Buzdin had carried out more rigorous calculations considering the thermodynamic properties of ferromagnet / superconductor / ferromagnet nanostructures as a function of thickness of the ferromagnetic layer d_{FM} and the interface transparency [23]. They assumed the superconducting layer thickness d_{sc} to be smaller than the superconducting coherence length ξ_{sc} and assumed the dirty limit for all layers in order to use the Usadel's equations [19] same as that used by Z. Radovi´c et al. in Ref. [18]. For the limit of a high interface transparency, they calculated T_{sc}^{red} as

$$T_{sc}^{red} = T_{sc0}\left(1-\frac{\pi}{2\tau T_{sc0}}\right) \qquad \textbf{(5.5)}$$

where τ is the magnetic scattering time $\tau \propto 1/\Delta E_{ex}$ which reduces T_{sc}. If the influence of magnetism on the superconductivity is weak, i. e. if $1/\tau T_{sc0} \ll 1$, the superconducting condensation energy can be approximated as

$$E_{cond} = -\gamma_0\left(\frac{T_{sc}^{red}-T}{T_{sc0}}\right) \qquad \textbf{(5.6)}$$

where γ_0 is a constant. The parameter γ_0 is specified in [23]. Here, it is not of particular interest.

In addition, the theoretical calculations, F.S. Bergeret, A.F. Volkov and K.B. Efetov explained the surprisingly high conductance observed in metallic ferromagnets in proximity to a superconductor in the superconducting state [24] with a spin-triplet contribution to the superconducting order parameter. They assumed a small value of the anomalous quasi-classical Green's function (low interface transparency) in order to linearise the Usadel's equations. They showed that an inhomogeneity in the magnetisation at an interface can induce such a triplet component of the superconducting order parameter that corresponds to Cooper pairs with parallel electron spins [25,26,27]. The penetration depth of this triplet component into the ferromagnetic layer is actually much larger than the one of the singlet one ξ_{FM}:

$$\xi_{FM}^{\uparrow\uparrow} = \sqrt{\frac{\hbar D_{FM}}{2\pi k_B T}} > \sqrt{\frac{4\hbar D_{FM}}{\Delta E_{ex}}} = \xi_{FM} \qquad \textbf{(5.7)}$$

The penetration depth of the singlets component of a normal metal and the length $\xi_{FM}^{\uparrow\uparrow}$ are of the same order (see **Equation 5.2**). Following the idea of a triplet component of the superconducting order parameter, they calculated the influence of the conduction electrons on the magnetization of the ferromagnet and on the magnetic moment induced in the superconductor. In Ref. [26] they used a simple mean field approximation model, where they assume the ferromagnetic exchange energy ΔE_{ex} to be smaller than the Fermi energy and a

low interface transparency. They concluded that the magnetization in the ferromagnet can be reduced and that a magnetic moment aligned antiparallel to the one in the ferromagnet can be induced in the superconductor over the length scale of the superconducting coherence length ξ_{sc} [26,27]. In an extremely simplified picture, one can imagine Cooper pair singlets of which one of the electrons penetrates into the ferromagnetic layer, while the second one is more localized in the superconductor. The electron in the ferromagnet will align its spin along the local magnetic field. Subsequently, the spin of the second electron has to bealigned antiparallel, in order to sustain the singlet state of the Cooper pair (see **Figure 5.1**). F.S. Bergeret, A.F. Volkov and K.B. Efetov called this effect the inverse proximity effect because there is a magnetic moment induced in the superconductor, which is antiparallelly aligned to the ferromagnetic moment.

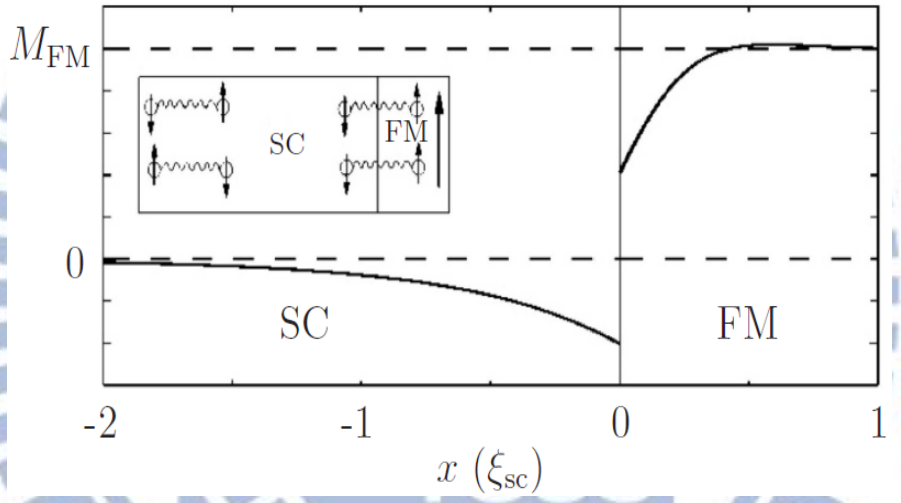

Figure 5.1 *Inverse proximity effect: One electron of a Cooper pair which takes a place mainly in the ferromagnet aligns its spin parallel to the ferromagnetic moment. However, the second one of the same Cooper pair aligns its spin antiparallel to conserve the Cooper pair's singlet state. This figure was taken from [26].*

Moreover, Z. Sefrioui and co-workers reported a new proximity effect [28]. They observed by transport (resistance) and by SQUID measurements that superconductivity survives even in 3.5 nm thick YBCO layers that are adjacent to a ferromagnetic layer. These are considerably thinner superconducting layers than achievable with conventional superconductors. They also observed that T_{sc} changes with varying ferromagnetic layer thickness in heterostructures with a ferromagnetic layer thickness of up to 100 nm. Moreover, the former observation can be explained by the short superconducting coherence length in the superconducting YBCO of 0.1 – 0.3 nm (along the c-axis), while the latter remains subject to

speculations. According to the theory of Z.Radovi´c et al. [18], the interaction between the superconducting and ferromagnetic layers should only be possible if the ferromagnetic layer is thinner than two times the decay length of the superconducting order parameter into the ferromagnet $\left(d_{FM} < 2\xi_{FM}\right)$. T_{sc} should then only be dependent on the thickness of the ferromagnetic layers. The length scale observation is special landmark to study superconductivity, since the exchange energy in LCMO is very large (estimate about 3 eV [29]) and therefore ξ_{FM} small. Z. Sefrioui and co–workers proposed that a reduced magnetic moment in the LCMO layers and a high interface transparency are the main reasons for the unusually large value of ξ_{FM}. A different explanation which has not been discussed by Z. Sefrioui and co-workers would be a triplet component of the T_{sc} as described by F.S.Bergeret, A.F.Volkov and K.B.Efetov [25]: The value of $\xi_{FM}^{\uparrow\uparrow}$ can be considerably larger than the one of ξ_{FM} because the ferromagnetic exchange coupling in the ferromagnetic layers does not give rise to a pair breaking of a triplet.

V.Pe˜na et al. (2005): V.Pe˜na and co-workers measured an unconventional giant magnetoresistance effect in LCMO/YBCO/ LCMO trilayers in the superconducting state [30]. If the magnetic moments were in the layer plane and the temperature was close to T_{sc}, they found a maximum magnetoresistance $\Delta R/R = \left(R_{\max} - R_{\min}\right)/R_{\min}$ of LCMO up to 1600%, which was decreasing exponentially when getting closer to T_{sc}. The only precondition for this effect was a working temperature below T_{sc}. The most important difference compared to a conventional CMR effect was, that they measured the highest resistance for an antiparallel alignment of the magnetic moments in the LCMO layers and the lowest one for a parallel alignment. This is opposite to the systems with conventional superconductors that are discussed by I.Baladi´e and A.I.Buzdin in Ref. [31]. The effect observed by V.Pe˜na and co-workers occurred in heterostructures with a YBCO layer thickness of up to 30 nm, which is considerably larger than the fraction of a nanometer of the superconducting coherence length ξ_{sc} in YBCO along the c-axis. This is opposite to the assumption made by I.Baladi´e and A.I.Buzdin, where the thickness of the superconducting layer was smaller than ξ_{sc}. It seems therefore, that there is an additional length scale which has to be considered in order to explain the observed physical phenomena. They gave an explanation without focusing on an additional length scale. They argued with the injection of spin-polarised carriers into the YBCO layer: In case of an antiparallel alignment, the injected charge carriers find a high

potential barrier to leave the superconductor at the interface to the second ferromagnetic layer and therefore accumulate in the YBCO layer. The superconducting current density can subsequently be reduced by the accumulated spins. In a parallel case, this spin accumulation does not take place and the resistance through the layers remains very low. An alternative explanation could be the formation of a spin density wave in the YBCO layer that is similar to the one which can be induced by the applying an external magnetic field in underdoped $La_{2-x}Sr_xCuO_4$ single crystals [32,33,34]. Such a spin density wave may couple the ferromagnetic layers through longer distances than superconductivity.

5.1.2 Review the charge transfer in YBCO/ LCMO Heterostructures

The studies on YBCO/ LCMO heterostructures have been findings that LCMO is a half-metal with a fully spin polarized conduction band and thus ideally suited for an efficient spin injection into adjacent materials, while YBCO is a superconductor with a complex d-wave symmetry order parameter and a very high transition temperature. YBCO/ LCMO heterostructures were thus expected to be suitable candidates for colossal magnetoresistance at high temperature superconducting devices [35]. Additionally, it had become technically possible to grow YBCO and LCMO heteroepitaxially on top of each other [36,37,38]. The interesting is that the two competition ordered parameters of YBCO and LCMO have a similar energy scale, which may lead to new, proximity-induced physics and charge transfer at the interfaces. A sizeable number of studies on YBCO/ LCMO heterostructures which used different techniques will briefly debate here. The other relevant studies are introduced.

T. Holden et al. (2004): T. Holden and co–workers reported that even the normal state electronic properties of YBCO/ LCMO superlattices exhibit an unusual dependence on the layer thickness [39]. They investigated the electronic properties of YBCO/ LCMO superlattices with spectral ellipsometry and observed that the metallic response is reduced for superlattices with a layer thickness of less than 16 nm in the far infrared range (100 – 700 cm^{-1}). The plasma frequency $\omega_p^2 = \frac{4\pi n}{m^*}$, which is proportional to the ratio of the free carrier concentration n to their effective mass m^*, and is given in **Table 5.1** (at 10 K, 100 K, and 300 K). The value of ω_p^2 is proportional to the free-carrier spectral weight, which is the dominant contribution to the area under the σ_1 curve in the far-infrared region. The value of ω_p^2 has been decreased more than an order of magnitude when the layer thickness is reduced from

60:60 nm to 8:6 nm. However, even the 8:6 nm SL, despite its very low ω_p^2 and the correspondingly low density of the superconducting condensate, exhibits a superconducting transition in the resistivity at T_c = 60 K. At the same time this SL still exhibits a Curie temperature at T_{mag} = 120 K. A significant suppression of ω_p^2 is evident already for the 16:16 nm SL. This effect is most pronounced at 300 K, i.e., above the CMR transition at T_{mag} = 215 K where the LCMO layers are known to remain in the insulating state. The apparent increase in conductivity below 200 K has coincidence with the FM transition and thus with the well-known metal-insulator transition in the LCMO layers that is at the heart of the CMR effect. This finding suggests that the metallicity of the YBCO layers has already been entirely suppressed for the 16:16 nm SL whereas the LCMO layers still exhibit metallic behavior below the FM transition. But the holes concentration was reduced considerably, when the YBCO and the LCMO layers were equally thick. Interestingly, in this paper, authors could not observe this reduction of the metallic response if they used samples that are paramagnetic metals, like $LaNiO_3$ or insulators like $PrBa_2Cu_3O_7$ instead of LCMO.

However, the long range proximity effect and charge transfer may be clear here but the hole contributions from both YBCO and LCMO and the separation of individual contributions need more investigation.

N.Haberkorn et al. (2004): N.Haberkorn and co-workers observed an exchange bias in YBCO/ LCMO superlattices grown on MgO at low temperatures, if the samples were cooled in an applied magnetic field of 1T [40]. They attributed this effect to a thin layer of interface in its vicinity which is ordered antiferromagnetically. They expected this layer to be located along with the LCMO layers and consisting of antiferromagnetically ordered Mn-ions, because they measured a reduced net magnetic moment of the LCMO layers as compared to the bulk value and that was resulted from the fact that H_{coerc} did not obey the inverse proportionality to the film thickness commonly expected for thin magnetic films. The antiferromagnetic layers could arise due to interdiffusion of Mn- or Cu-cations, due to stress or due to a different oxygen concentration at the interfaces. Antiferromagnetism is by orders of magnitude less sensitive to changes in the direction of applied magnetic field than ferromagnetism. An antiferromagnetic layer at the interfaces could therefore induce an easy direction for the adjacent moments in the ferromagnetic ordered centre of the LCMO layers and lead to the observed exchange bias.

TABLE I. Physical parameters for representative SL's and Films grown by laser ablation.

$[d_{YBCO}:d_{LCMO}]$	T_c (K)	T_{mag} (K)	ω_p^2 (10 K) (eV^2)	Γ(10 K) (eV^2)	ω_p^2 (100 K) (meV)	Γ(100 K) (meV)	ω_p^2 (300 K)	Γ(300 K)
[8:6 nm]×20	60	120	0.035	49	0.029	49	0.024	50
[5:5 nm]×40	60	120	0.026	31	0.025	28	0.025	21
[16:16 nm]×10	73	215	0.36	26	0.29	33	0.11	32
[60:60 nm]×5	85	245	0.63	22	0.55	33	0.37	66
[60:15 nm]×5	86	160	1.44	27	1.41	49	1.14	79
[30:15 nm]×5	80	165	0.80	27	0.84	43	0.7	65
[13:5 nm]×20	56	115	0.44	29	0.43	38	0.36	66
[8:3 nm]×20	60	120	0.55	34	0.55	43	0.46	54
[15:30 nm]×5		195	0.39	44	0.22	44	0.12	38
[15:60 nm]×5		240	1.03	42	0.80	43	0.064	21
$[d_{YBCO}:d_{LNO}]$								
[5:5 nm]×20	33		1.15	69	1.10	72	1.04	76
[10:10 nm]×20	70		1.19	57	1.21	60	1.07	72
$[d_{YBCO}:d_{PBCO}]$								
[10:10 nm]×20	85		0.36	12	0.57	31	0.49	48
Pure Materials								
YBCO	90		0.93	19	1.22	42	1.03	75
LCMO		245	1.08	37	0.61	37	0.03	10
LNO			0.99	103	0.95	98	1.04	111
Ru-1212		145	0.30	28	0.28	32	0.24	53

Table 5.1 *Physical parameters for representative SL's and films grown by laser ablation (taken from [39])*

Finally, **S.J. Pennycook et al. (2006)**, in this work, observed lack of uniformity in the oxidation state of Mn in the samples [41]. According to the phase diagram of LCMO, an inhomogeneous magnetization in different layers is reflected. The decreasing trend measured by electron energy loss spectroscopy (EELS) in the average Mn 3d band occupation (again, the Mn average valence goes from +3.3 for a YBCO thickness of one unit cell to around +3.5 for a YBCO thickness around 10 unit cells) is consistent with an increasing charge transfer from LCMO to YBCO as the YBCO layer thickness increases. Simultaneously, the saturation magnetization in these $[YBCO_{n\ u.c.}/LCMO_{15u.c.}]_{100nm}$ samples decreases when the YBCO layer thickness is increased (saturation is reached for YBCO layer of thicknesses around 5 unit cells), which could also be as consequence of the transfer of electrons into the YBCO interface layers. It is worth noting here that, although charge transfer phenomena will modify the superconducting properties over distances within 3 unit cells from the interface, superconductiviy in superlattices is suppressed over a much longer length scales compared to samples with non magnetic spacers (YBCO/PBCO superlattices) which is related to long range charge transfer effect. On the other hand, the modification of the magnetic properties of LCMO resulting from the electron transfer can have a direct impact on proximity phenomena. The oxidation state of Mn (+3.5) renders the LCMO at the vicinity of a critical point, where ferromagnetic and antiferromagnetic phases coexist. LCMO layers will be magnetically inhomogeneous, as reflected by the decreased saturation magnetization. The presence of

antiferromagnetic regions might provide an explanation for the long range proximity effect, which on theoretical grounds is not expected in YBCO/LCMO heterostructures.

Most of studies have focused on the superlattices, because it is the model that can switch the terminations at interfaces, and enhance the interactions or coupling between ferromagnetism and superconducting, however, no one has really shown the terminations control to understand the physics behind. In this work, we have presented an ideal tool to understand the physics behind creating two different interfaces of LCMO/YBCO.

5.2 Models and Experimental method

5.2.1 Models and Epitaxial design of the interfaces

Both YBCO and LCMO have ABO_3 perovskite related structures. Two possible atomic stacking sequences can be formed along the (001)-oriented heterostuctures: a) $La_{0.7}Ca_{0.3}O–MnO_2–BaO–CuO_2$ (MnO_2-terminated interface) and b) $MnO_2–La_{0.7}Ca_{0.3}O–CuO_2–BaO$ ($La_{0.7}Ca_{0.3}O$–terminated interface). Realizing this interface design requires atomically precise interface control which can be achieved by designing the LCMO layers with well-defined atomic terminations using reflection high-energy electron diffraction (RHEED) assisted pulsed laser deposition. The clear intensity of the oscillations indicated a layer–by–layer growth mode with the unit cell precision during the growth of the LCMO, YBCO and $SrRuO_3$ (SRO) layers. The SRO layer was inserted to switch termination of the LCMO layer [42]. Two distinct interfaces can be fabricated based on the control of the LCMO termination layer. The details of the heterostructure growth can be found in **Figure 5.2a)** and **5.2b). T**he schematics of the MnO_2–terminated and $La_{0.7}Ca_{0.3}O$–terminated interfaces (i.e., the interfacial control of a heterostructure built with two perovskites stacked along the (001) direction) are shown. We deposited $YBCO_d$/LCMO on different interfaces with a constant LCMO layer thickness of n=25 unit cells (u.c.) (corresponding to 10nm). The thickness d of YBCO layer, however, varied from 2nm to 100nm. In this chapter of thesis, "MnO_2-terminated" corresponds to the $STO/LCMO_{10nm}/YBCO_d$ structure (black in the online data) while "$La_{0.7}Ca_{0.3}O$-terminated" corresponds to the following $STO/SRO_{1.5u.c.}/LCMO_{10nm}/YBCO_d$ structure (red in the online data).

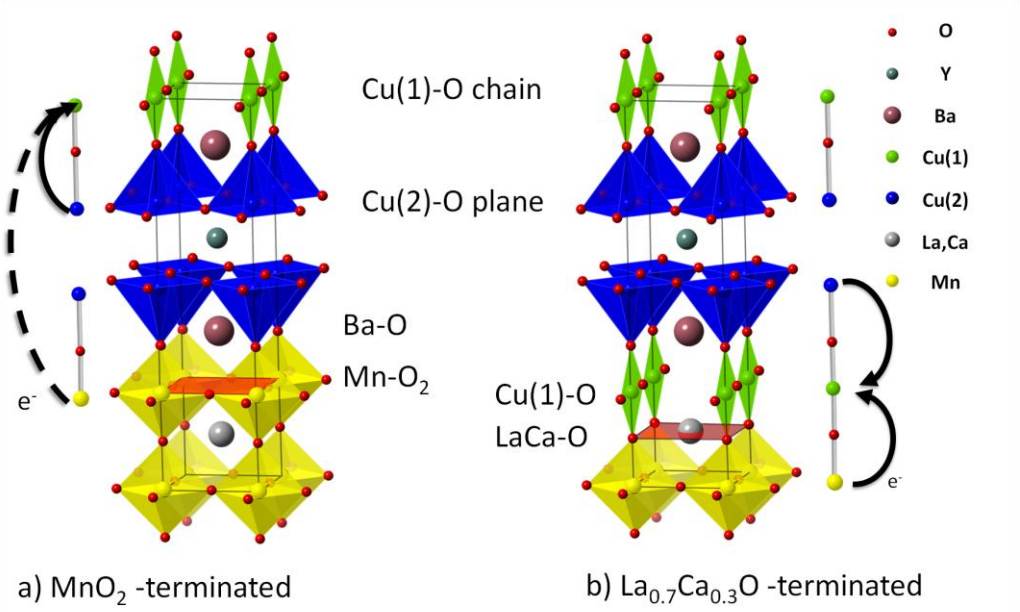

Figure 5.2 *Epitaxial design of heterointerfaces: Schematic of the interfacial control of LCMO/YBCO$_d$ with different interfaces;* **a)** *in the MnO$_2$-terminated interface (La$_{0.7}$Ca$_{0.3}$O–MnO$_2$–BaO–CuO$_2$) the charges are very difficult to transfer because the CuO chain is very far from the interface (indicated by a dashed line) while* **b)** *switches into the La$_{0.7}$Ca$_{0.3}$O-terminated (MnO$_2$–La$_{0.7}$Ca$_{0.3}$O–CuO$_2$–BaO) interface by using SRO; electrons transfer easily from LCMO to YBCO because of the CuO chain at the interface (indicated by solid lines).*

5.2.2 Experimental details

5.2.2.1 Sample preparation

$YBa_2Cu_3O_{7-x}$/$La_{0.7}Ca_{0.3}MnO_3$ (YBCO/LCMO) hetrostructures were prepared on 5x5 mm^2(100)-oriented $SrTiO_3$ (STO) single crystal. We used *in-situ* reflection high-energy electron diffraction (RHEED) to monitor layer growth. The LCMO and YBCO layers were deposited at respective growth temperatures of 700^{o}C and 750^{o}C, and oxygen pressures of 80 mTorr and 150 mTorr. To switch the (La,Ca-O) termination at the interface, a buffer layer of SRO (1.5u.c.) was deposited between the substrate and the LCMO layer. For MnO2-terminated interface, we used uniform single termination of TiO_2. The TiO_2 terminated STO (100) surfaces were obtained by chemical treatment with an HF-NH_4F buffer solution. The growth processes and the switching of terminations at different interfaces of YBCO/LCMO are demonstrated on **Figure 5.3** Inset of **Figure 5.3 a)** and **b)** (on top) show the *in-situ* RHEED patterns and TiO_2 terminated surface of STO (100).

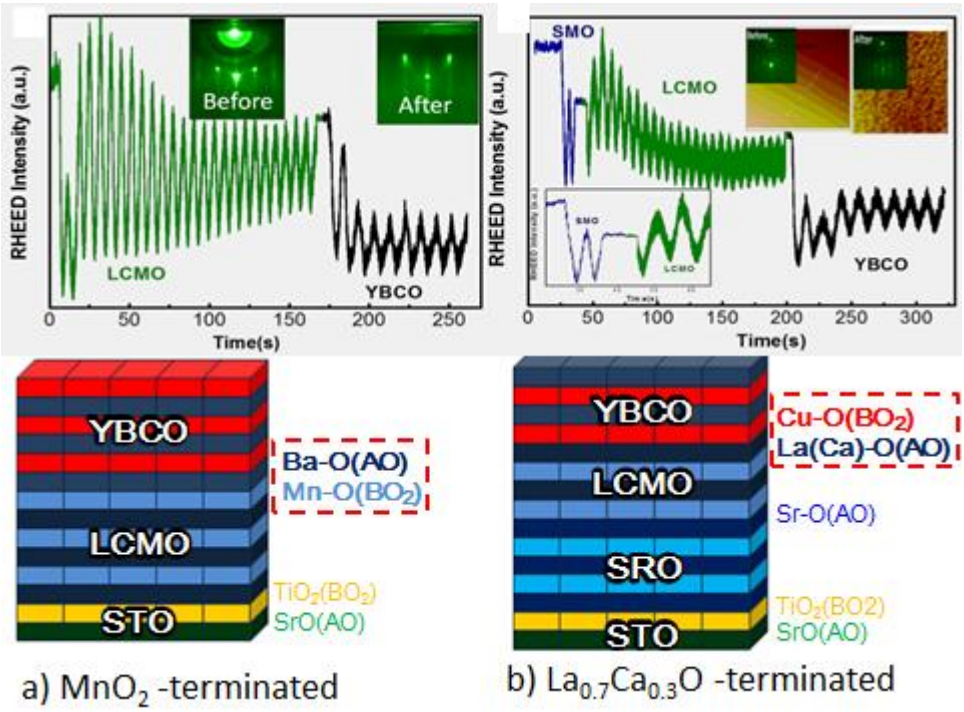

Figure 5.3 *Interface control "Growth model": Layer–by –layer growth is monitored by RHEED,* **a)** *the MnO_2-terminated interface corresponds to the STO/$LCMO_{10nm}$/$YBCO_d$ structure while* **b)** *the $La_{0.7}Ca_{0.3}O$-terminated interface has the following STO/SRO_{1nm}/$LCMO_{10nm}$/$YBCO_d$ structure.*

Following layer deposition, full oxygenation was achieved by annealing the film at 550°C in an oxygen atmosphere of 700Torr for an hour followed by slow cooling to room temperature.

5.2.2.2 XAS and XMCD

XAS and XMCD are the most appropriate techniques by using an extremely sensitive local probe to study the valence and spin characters as well as the orbital contribution to the magnetic moment. The XAS and XMCD spectra of the Mn-$L_{2,3}$ edge and the XAS of the O *K*-edge were recorded using the Dragon and 20A beamlines of National Synchrotron Radiation Research Center (NSRRC) in Taiwan with respective energy resolutions of 0.2 eV, and 0.3 eV. The sharp peaks at 640.1eV of the Mn-L_3 edge of single crystalline MnO, and at 934.7 eV and 531 eV of the Cu-L_3 edge and the O *K*-edge of single crystalline Cu_2O were measured simultaneously in a separate chamber for energy calibration, which enabled us to achieve accuracy better than 0.05 eV for relative energy alignment. Both the XMCD spectra

of the Mn-$L_{2,3}$ edge were measured under a magnetic field of 1T at the temperature 30K with approximately 80% circularly polarized light. The magnetic field direction makes an angle of 30° with respect to the Poynting vector of the soft x-rays. The spectra were recorded using the total electron yield (TEY) method (by measuring the sample drain current) under an ultrahigh chamber (UHV) with a base pressure of $1x10^{-9}$ mbar.

The polarized O *K*-edge XAS spectra were carried out by the synchrotron linear polarized light with **E**//ab in normal incidence on the sample and the signals were detected in the total x-ray fluorescent yield (FY) mode and sample current mode. The probing depth of FY detection is about in the order of 200 nm and several nano meters for FY and sample current modes, respectively. The base pressure in the UHV chamber was about 10^{-9}Torr. The resolution of the spectra was controlled by the spherical grating monochromator and was estimated to be better than 0.22eV. As a routine procedure, following pre-edge background subtraction, the spectra were normalized using the incident beam intensity, keeping the energy range between 580-620 eV for the O *K*-edge spectra.

Mn *K*-edge XAS spectra were recorded in a fluorescence mode with a Lyttle detector at BL17c1 beamline of NSRRC. A double Si(111)-crystal monochromator was used for energy selection with a resolution ΔE/E better than 2×10^{-4}. Higher harmonics were eliminated by detuning the double crystal Si(111) monochromator. X-ray energy was calibrated by the known Mn *K*-edge absorption of Mn foil.

5.3 Results and Discussions

5.3.1 Transport measurement

Transport measurements were performed from 2K to room temperature by the standard four-probe method. **Figure 5.4** shows the resistivity $\rho(T)$ of LCMO/$YBCO_d$ with the $La_{0.7}Ca_{0.3}O$-terminated interface and the MnO_2-terminated interface. Intriguingly, the $La_{0.7}Ca_{0.3}O$-terminated samples always show a higher value of ρ than that of the MnO_2-terminated samples. With YBCO thickness being 6nm as shown in **Figure 5.3a)**, the $La_{0.7}Ca_{0.3}O$-terminated sample is insulating while the MnO_2-terminated sample is superconducting with a transition temperature T_c=30K. With increasing YBCO thickness, both the MnO_2- and $La_{0.7}Ca_{0.3}O$-terminated samples show the superconducting state as in **Figure 5.4b)** and **5.4c)**. As in the case of ρ**,** the $La_{0.7}Ca_{0.3}O$-terminated samples always have a higher T_c. However, as displayed in **Figure 5.4d)**) which shows T_c as a function of YBCO

thickness for both types of terminations, the difference of T_c between the MnO_2- and the $La_{0.7}Ca_{0.3}O$-terminated samples decreases as the YBCO thickness increases. This is what one would expect, since for thicker YBCO layers, the interfacial to YBCO volume ratio is low and the contribution from the LCMO/$YBCO_d$ interfaces and hence the difference in T_c becomes negligible (**Figure 5.4d)**). It is also evident from **Figure 5.4d)** that the suppression of T_c in the $La_{0.7}Ca_{0.3}O$-terminated samples is more pronounced than in the MnO_2-terminated samples, indicating the enhanced interaction between superconductivity and magnetism in the former. Since the T_c suppression is primarily due to the F/S proximity effect and charge transfer at the interface [4,5,9,10,11], our data clearly demonstrate that controlling the interfaces is crucial to the effective manipulation of the superconducting state and physical properties at the heterostructure of LCMO/YBCO interfaces.

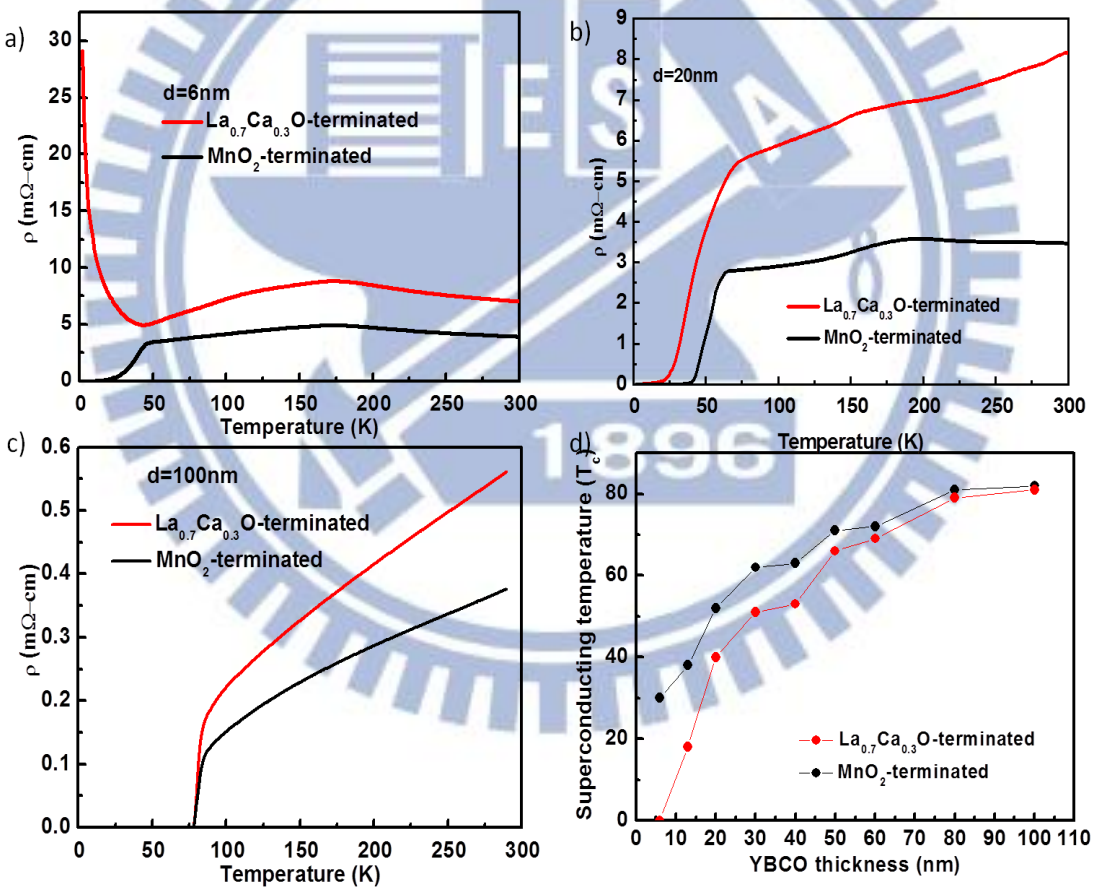

Figure 5.4 *(color online) Transport properties of LCMO/$YBCO_d$ with different interfaces: Resistivity vs. temperature of LCMO/$YBCO_d$* ***a)*** *d=6nm,* **b)** *d=20nm,* **c)** *d=100nm, and* **d)** *Superconducting temperature, T_c, as a function of YBCO thickness for both the MnO_2- and $La_{0.7}Ca_{0.3}O$-terminated interfaces.*

5.3.2 Magnetic properties

In addition to differences in T_c, different terminations also lead to different magnetic properties in these heterostructures. **Figure 5.5a)** shows $M(T)$ of LCMO/$YBCO_d$ with different terminations, while the thickness of the YBCO layers is maintained at d= 30nm. For both samples, the Curie temperature of LCMO is around 170K. However, the $La_{0.7}Ca_{0.3}O$-terminated sample clearly has a smaller degree of magnetization. The inset of **Figure 5.5a)** shows $M(H)$ hysteresis loops of the STO/LCMO/$YBCO_{30nm}$ and STO/SRO/LCMO/$YBCO_{30nm}$ samples, which were measured at T = 100 K above superconducting temperature,T_c, to avoid any possible complication from the superconducting state. The magnetic hysteresis was recorded with the magnetic field oriented perpendicularly to the sample surface, i.e., in the out-of-plane configuration. The $La_{0.7}Ca_{0.3}O$-terminated sample demonstrates further depressed magnetization compared to the MnO_2–terminated sample. Previous investigations of LCMO/$YBCO_d$ bilayers [43] have shown that the magnetic moment of LCMO is affected by the YBCO layer and its thickness. **Figure 5.5b)** shows that magnetization decreases as YBCO thickness increases. The decrease in magnetization in similar superlattice samples has been related to long range proximity effects [12,44,45]. Together with T_c suppression, the decreased magnetization is regarded as resulting from F/S competition. The long-range proximatity effect (~100 nm) has been a long-standing puzzle. In our system, the decreased T_c of YBCO with decreasing YBCO thickness and the decreased magnetization of LCMO with increasing YBCO thickness both qualitatively fit into the proximity scenario. However, the F/S competition context does not provide an immediate picture of the functionality for different terminations. Moreover, it is particularly disturbing that the $La_{0.7}Ca_{0.3}O$-termination simultaneously results in both lower T_c and reduced magnetization. According to the F/S competition scenario, larger FM fluctuations should be associated with stronger superconductivity. Thus, the present observations could not be reconciled solely with the proximate scenario and new mechanisms other than the F/S proximity effect must be considered.

Figure 5.2 clearly illustrates the charge transfer model at the two different interfaces. In pure YBCO, the hole doping in the CuO_2 planes is achieved via CuO chains, which are electron-takers. Hole doping in the CuO_2 planes can be achieved by intercalating oxygen into the CuO chains. For the heterostructures, charge transfer from LCMO to YBCO occurs with

both terminations. Particularly, in $La_{0.7}Ca_{0.3}O$-terminated samples (shown in **Figure 5.2b)**), the CuO chains are closer to the MnO planes and the transfer of electrons from the MnO planes to the CuO chains is relatively easier (as indicated by the black solid arrow). Consequently, fewer electrons in the CuO planes were transferred to the CuO chains (or the holes in the CuO planes are "filled" by electrons transferred from the MnO planes). On the other hand, with the MnO_2-terminated interface (**Figure 5.2a)**), the CuO chains are far from the MnO planes. Therefore, the tendency of electron transfer from the MnO planes to the CuO chains is weaker (as indicated by the black dashed arrow). By the same token, there are relatively more holes in the CuO_2 planes in the MnO-terminated samples. This charge transfer model explains the observed properties of superconductivity and magnetism in these heterostructures. Without atomically precise interface control, this charge transfer mechanism could be difficult to identify. The number of Mn ions is fixed (LCMO 10nm for both interfaces) in both sample types. As the thickness of the YBCO increases, it takes more electrons from LCMO. The magnetization of LCMO thus decreases as the YBCO layer thickness increases. However, when the YBCO layer becomes very thick, this charge transfer effect obviously diminishes (as does the proximate effect). Therefore, the T_c of the samples with a thicker YBCO layer reverts to that of bulk YBCO. The difference in T_c for these two types of interfaces also becomes smaller as the thickness of the YBCO layers increase (**Figure 5.4b)**). Furthermore, **Figure 5.5b)** shows the expected leveling of the magnetization reduction with increasing YBCO thickness.

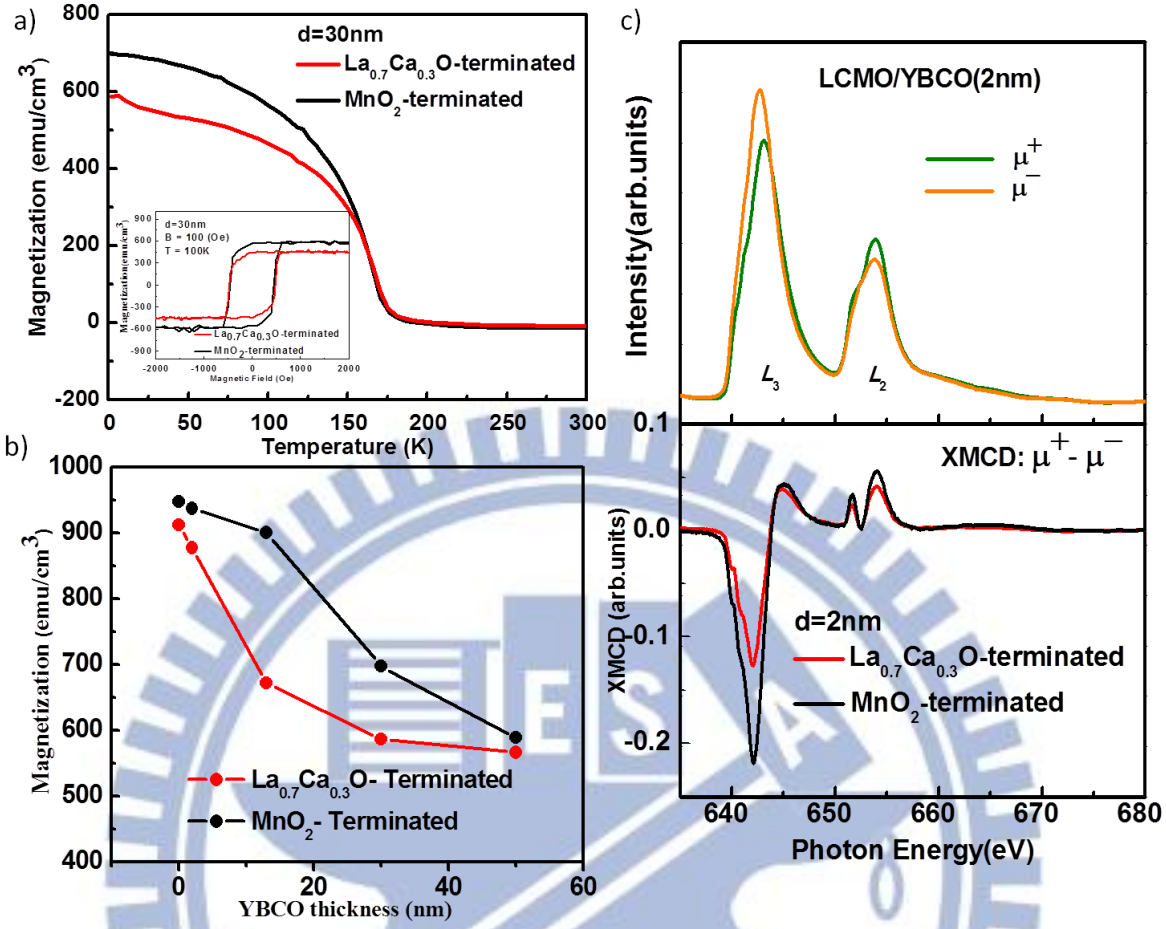

Figure 5.5 *(color online)* **a)** *Temperature dependence of the field cooled magnetization measured in H = 100Oe out-of-plane; Inset shows the M-H loops of* $LCMO/YBCO_d$ *with different interfaces recorded at 100K and with H applied out-of-plane along [100]STO directions.* **b)** *Low- temperature magnetization as a function of YBCO layer thickness for the two different interfaces.* **c)** *Mn* $L_{2,3}$ *–edge spectra of the YBCO (2nm)/LCMO (10nm) bilayer with different interfacial terminations taken with circularly polarized x-rays at T=30K. The photon spin was aligned parallel* (μ^+, *green) or antiparallel* (μ^-, *orange) to the 1 T magnetic field. The field was applied along the surface normally; Mn-*$L_{2,3}$ *XMCD signal with the* $La_{0.7}Ca_{0.3}O$*-terminated interface (red line) and the* MnO_2*-terminated interface (black line) for* $LCMO/YBCO_d$ *are shown in lower panel.*

5.3.3 X-Ray absorption spectra (XAS): Evidence of Charge transfer at interfaces

Macroscopic measurements suggest different T_c and magnetic moments for the heterostructures with distinct interfaces. To confirm the magnetization of the different interfacial terminations measured by the Superconducting Quantum Interference Device (SQUID), we recorded the Mn $L_{2,3}$ -edge X-ray absorption (XAS) spectra and X-ray magnetic circular dichroism (XMCD) with the photon helicity aligned parallel μ^+ (green line) and anti-parallel μ^- (orange line) to the magnetic field. As shown in **Figure 5.5c)**, the XMCD spectra of LCMO/$YBCO_{2nm}$ of the MnO_2- and the $La_{0.7}Ca_{0.3}O$-terminated samples display the differences between the XAS spectra obtained by the two types of helicities. The magnetic moment of Mn in the $La_{0.7}Ca_{0.3}O$-terminated sample was found to be smaller than that in the MnO_2-terminated one. The further suppression of the magnetization in the $La_{0.7}Ca_{0.3}O$-terminated sample was thus consistently confirmed by both XMCD and SQUID measurements. According to the present model, this is attributed to the change of the Mn^{4+} to Mn^{3+}ratio. For the thicker YBCO layer, the charge transfer from the LCMO to the YBCO layer produces more Mn^{4+} ions, thus causing the reduction of Mn magnetization, as shown in **Figure 5.5b)**.

Motivated by these observed changes to the magnetic properties with various interface terminations, we used XAS spectra at the Mn *K*-edge to determine the valence state of Mn for the MnO_2- and $La_{0.7}Ca_{0.3}O$- terminated samples as shown in **Figure 5.6a)**. The valence state of Mn for the different terminated samples with the reference samples $La_{1-x}Ca_xMnO_3$(x = 0, 0.3, 0.6 and 1) and standard samples Mn_2O_3 (Mn^{3+}), and MnO_2 (Mn^{4+}) is shown in **Figure 5.6b)**. The Mn valence state vs. thickness of the YBCO layers for the two distinct surface termiantions is shown in **Figure 5.6c)**. The $La_{0.7}Ca_{0.3}O$ -terminated samples apparently have higher Mn valence states than those found in the MnO_2-terminated samples. Moreover, the Mn valence state increases with YBCO thickness in either termination case. This positive correlation clearly indicates the charge transfer across the interface between the two materials. We also studied the Mn *L*-edge XAS of the LCMO/$YBCO_d$ (d=2nm, 6nm, and 8nm) with the various interfaces. The observed results strongly support the conclusions from Mn *K*-edge XAS (See **Figure 5.12**).

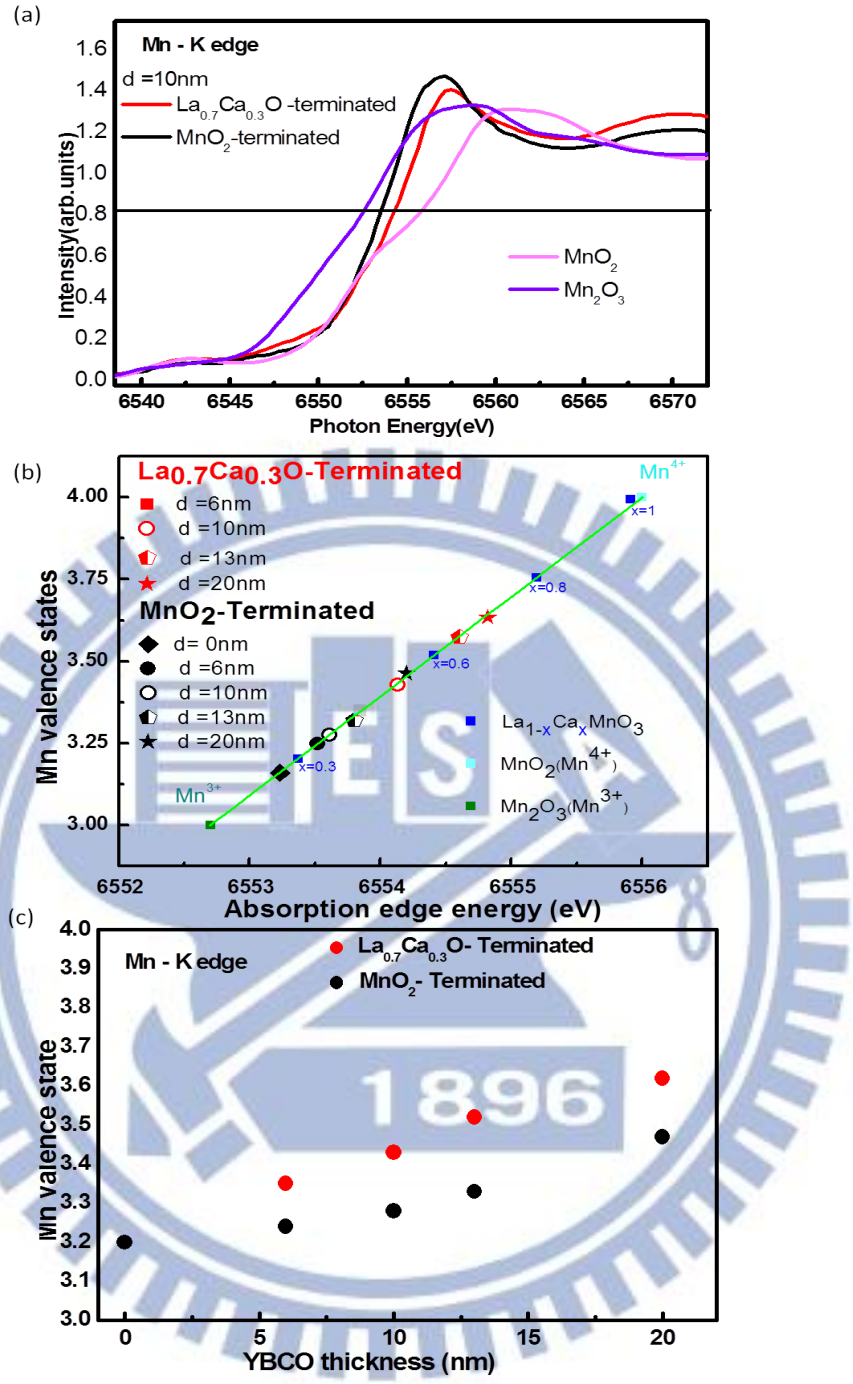

Figure 5.6 *(color online)* **a)** *Mn K -edge XAS spectra LCMO/YBCO$_d$ with different interfaces at thickness of YBCO is d =10nm and plot together with the Mn_2O_3 (Mn^{3+}) and MnO_2 (Mn^{4+}) standard samples spectra, taken in fluorescence yield mode.* **b)** *Mn valence states vs absorption edge energy (eV) of the MnO_2-terminated (black symbols) and $La_{0.7}Ca_{0.3}O$-terminated (red symbols) samples; $La_{1-x}Ca_xMnO_3$ (where x =0, 0.3, 0.6, and 1) was used as the reference data, combined with the Mn_2O_3 (Mn^{3+}) and MnO_2 (Mn^{4+}) standard samples to determine the Mn valence state.* **c)** *Mn valence states as a function of YBCO thickness on the different interfaces.*

5.3.4 O K edge XAS:

As we have known that the number of holes in the CuO_2 planes can be directly probed by O *K*-edge XAS, thus can also be examined to check the validity of our charge transfer scenario.

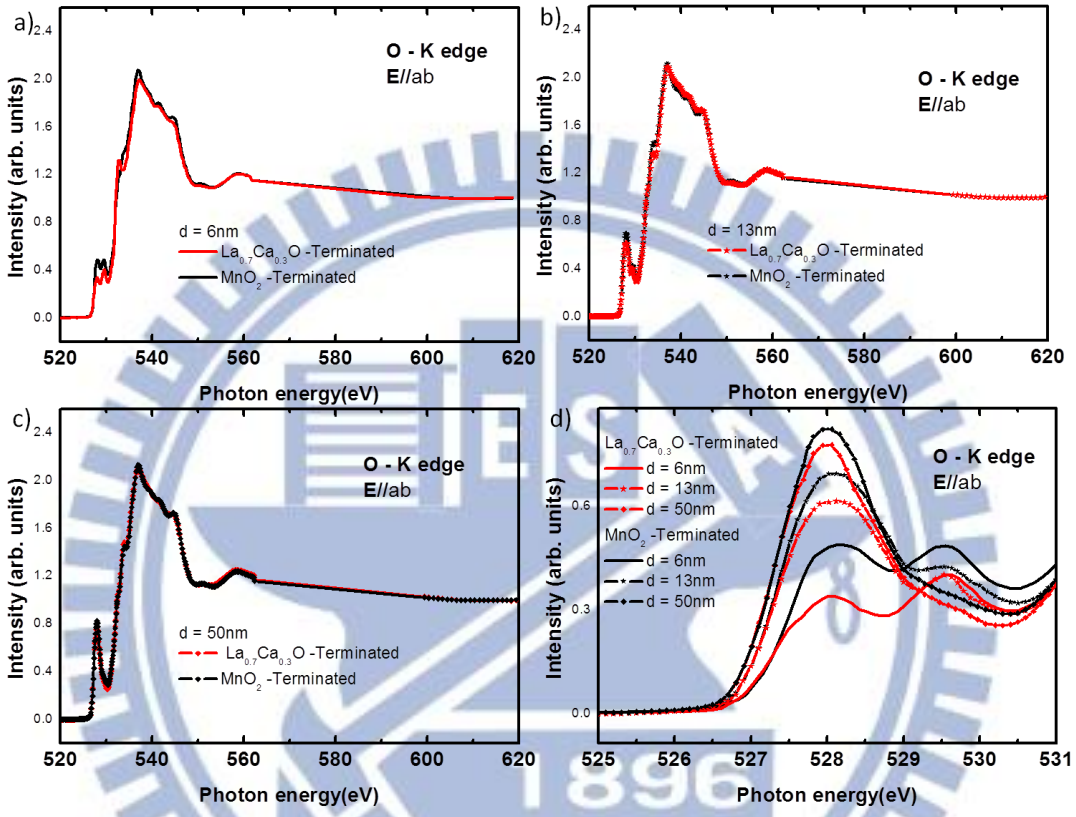

Figure 5.7 *(color online)* **a) - *c)*** *O K -edge XAS spectra LCMO/YBCO$_d$ with different interfaces vary thickness of YBCO is d =6nm, 13nm, and 50nm.* **d)** *Comparison of O K- edges XAS spectra LCMO/YBCO$_d$ with different interfaces with YBCO thicknesses of 13nm, 20nm and 50nm, taken in sample current mode.*

Full of O K -edge XAS spectra LCMO/YBCO$_d$ with different interfaces vary thickness of YBCO is d =6nm, 13nm, and 50nm after normalizations were shown in **Figure 5.7 a)-c)**. **Figure 5.7 d)** shows the polarized O *K*-edge spectra of the MnO_2- and $La_{0.7}Ca_{0.3}O$-terminated samples in the sample current mode with **E**//*ab*. In this way, the O *K*-edge XAS probes the O $2p_{x,y}$ hole states. In the present case, we mainly focus on the peak at 528eV of the photon energy, which is ascribed to the CuO_2 plane holes or the (Zhang-Rice singlets). The spectral weight of this peak is directly proportional to the hole number in the CuO_2 planes. Our results

clearly show the oxygen peak at 528eV increases with YBCO thickness. The enhancement of the oxygen peak for increased YBCO layer thickness signals higher holes concentrations and hence the T_c increases. XAS reveals that, given an identical YBCO thickness, the 528 eV peak in MnO_2-terminated samples is always larger than that found in the $La_{0.7}Ca_{0.3}O$-terminated samples. These results are consistent with higher values of T_c in the MnO_2-terminated samples. Furthermore, O *K*-edge XAS demonstrates the increase in hole numbers with increasing YBCO thickness, which certainly contributes to T_c enhancement. Evidently, the O *K*-edge XAS results fully supports the existence of the proposed charge transfer mechanism.

To confirm this, we also checked O K edge by fluorescence yield mode, the results are consistent with our sample current ones which means that we successfully separate the oxygen contribution of YBCO from LCMO and STO susbtrate in **Figure 5.8**.

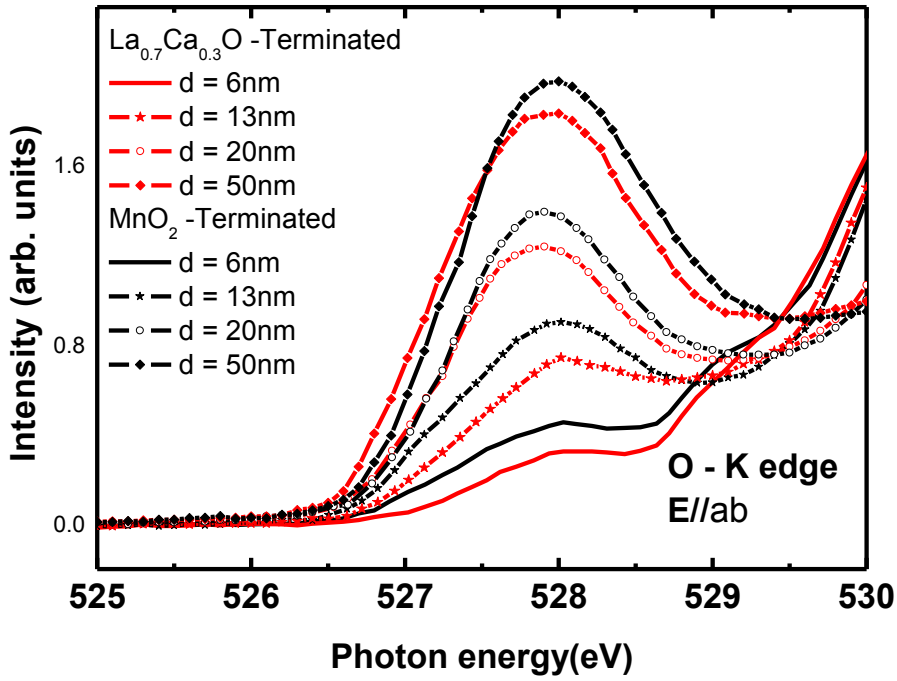

Figure 5.8 *(color online) Comparison of O K- edges XAS spectra LCMO/YBCO$_d$ with different interfaces with YBCO thicknesses of 13nm, 20nm and 50nm, taken in Fluorescence yield mode.*

5.3.5 Normalization of the X-Ray absorption spectra (XAS) (O K -edge)

X-ray absorption data reduction typically begins with fitting a first- or second-order polynomial to the pre-edge portion of the data. A first-order polynomial is often appropriate for transmission data, while a higher-order polynomial may be required if there is more curvature to the background, for example in fluorescence data collected using an energy

resolving detector. The pre-edge polynomial is extrapolated throughout the entire energy range of the data to give 'pre – edge subtracted' data. The pre-edge subtracted data typically are fit with a spline background function of some sort over the EXAFS, i.e. the post-edge region. The appropriate scaling factor is determined by setting an absorbance to 1.0. Often the value of the spline background function at the absorption-edge energy is used to set the scaling factor, although some authors define the maximum in the absorption coefficient near the edge as 1.0.

However, to determine the contribution of oxygen from YBCO in the complex oxide interfaces of YBCO/LCMO/STO with MnO_2-terminated interface and $La_{0.7}Ca_{0.3}O$-terminated interface, we have performed O *K*-edge measurements on three reference samples STO, LCMO, and YBCO by fluorescence mode. After verifying where does the contribution of YBCO in the complex oxide interfaces come from and how to separate the contribution of YBCO with others, we just focus on the peak location at 528eV, corresponding to Oxygen in YBCO, and the intensity of O-*K* edge as a function of photon energy is shown in **Figure 5.9**

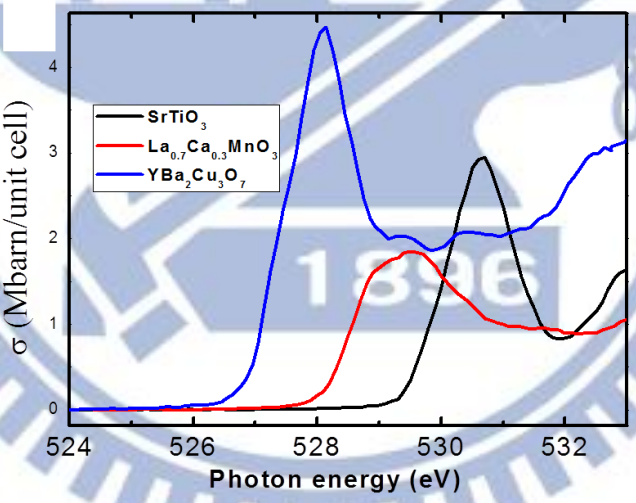

Figure 5.9 *The O K –edge XAS spectra illustrate the contribution of oxygen in different layers of structures: Enlarged peaks of oxygen in STO, LCMO and YBCO located at 531eV, 529.3eV and 527.8 eV, respectively.*

From **Figure 5.9** The O-*K* edge spectrum clearly shows oxygen contribution from YBCO (blue line) at photon energy corresponding to 528 eV.

In our experiments, to avoid the confusion pertaining to the probing depth of YBCO in fluorescence mode, as it is so large that it may cause its contributions from LCMO layer and Zang Rice band in YBCO, we have used the sample current mode with O - K edge with the surface sensitive **E**//ab. The two schematic structures of the multilayer and the intensity of

O-*K* edge as a function of photon energy are shown in **Figure 5.10 a-c)**. where the cover box dash line indicated the probing depth of the sample current mode can probe in our samples.

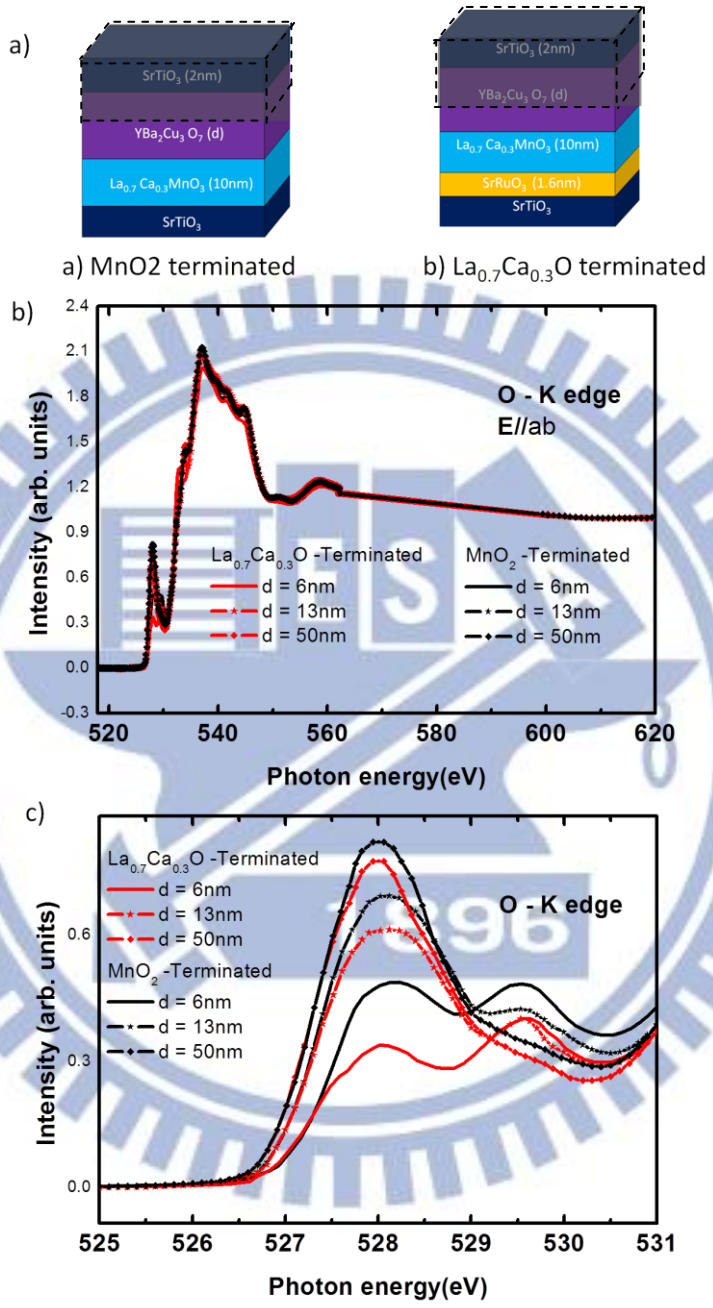

Figure 5.10 *The procedure to normalize the O K –edge XAS spectra:* **a)** *The structures with two different interfaces of LCMO/YBCO indicating the thickness and number of oxygen in one unit cell of each layer, in subscript and parenthesis, respectively for sample current mode.* **b)** *and* **c)** *the spectra after normalization and showing that the contribution of oxygen in our samples is very clear and can be separated from LCMO and STO.*

More difficulties and complicated, the X- ray absorption spectra (XAS) spectra are measured in florescence mode with **E**//ab and detection depth of florescence mode is around 250 nm for YBCO/LCMO with different interfaces. The spectra from the structure MnO_2-terminated interface (left) and LaCaO-terminated interface (right), similar like **Figure 5.10 a),** however, we have been normalized by the total number of oxygen in the multilayer with those present in STO substrate by probing depth up to maximum of 250nm of two different structures. So the total number of oxygen determined from XAS is listed in **Table 5.2**.

Layers		The number of oxygen in MnO2-terminated sample	The number of oxygen in LaCaO-terminated sample	comments
STO(3) capping (2nm)		15	15	1uc ~ 0.4nm
YBCO (7)	d =13nm	82.73	82.73	1uc ~1.17nm
	d =20nm	119.66	119.66	
	d =50nm	299.15	299.15	
LCMO(3) (10nm)		76.92	76.92	1uc ~ 0.39nm
SRO(3) (d1=1.67nm)		0	4.5	1uc ~ 1.1nm
STO(3) substrate can be penetrated by X-Ray (d2)	d2	1312.5	1300.125	d =13nm
	d2	1260	1247.625	d =20nm
	d2	1035	1022.625	d =50nm
Total numbers of oxygen	d =13nm	1487.15	1479.275	
	d =20nm	1471.58	1463.705	
	d =50nm	1426.07	1413.395	

Table 5.2 *Total number of oxygen with different thicknesses of YBCO of two different terminated interfaces.*

Here, the penetration depth of x-ray is assumed to be around 250nm. Based on our results shown in **Figure 5.10 b)** and **5.10 c)**, if the thickness of thin film of LCMO and YBCO is around 300nm, we cannot see any oxygen contribution from STO substrate, so the total thickness to which x-ray can penetrate from the top layer (STO capping layer) to the STO substrate should be around 250nm. In our experiment, we the thickness of STO capping layer,

LCMO are kept constant, (and also thickness of SRO layer, to switch the polarity at the LaCaO-terminated is maintained constant). So, the thickness to which the X-ray can penetrate through STO substrate, depends on the thickness of YBCO layer and can be calculated using the following the equation:

250 nm = $d_{STOcap} + d_{YBCO} + d_{LCMO} + d_{SRO} + d_{STO}$

Therefore $d_{STO} = 250\ nm - (d_{STOcap} + d_{YBCO} + d_{LCMO} + d_{SRO})$

Where, 250nm is the probing depth of the X-ray, d_{STOcap} is the thickness of STO capping layer, d_{YBCO} is the thickness of YBCO layer, d_{STO} is the thickness of STO substrate layer to which X-ray can penetrate, and d_{SRO} (=1.65nm) is the thickness of SRO layer to switch the termination at $La_{0.7}Ca_{0.3}O$- terminated interface.

5.3.6 Determination the Mn valence state:

The x- ray absorption spectra (XAS) are measured in sample current mode. The spectra from the structure MnO_2-terminated interface (left) and LaCaO-terminated interface (right), in **Figure 5.10 a).** Our spectra have been normalized by subtracting the background energy (pre-edge energy) to be zero and post-edge energy around photon energy of 600eV to be one of two different structures as shown in **Figure 5.10 b)** and **c)**.

Normalizing the Mn K and Mn L –edges are similar to that of O K –edge for sample current mode, However after normalization, we need to determine the valence state of Mn.

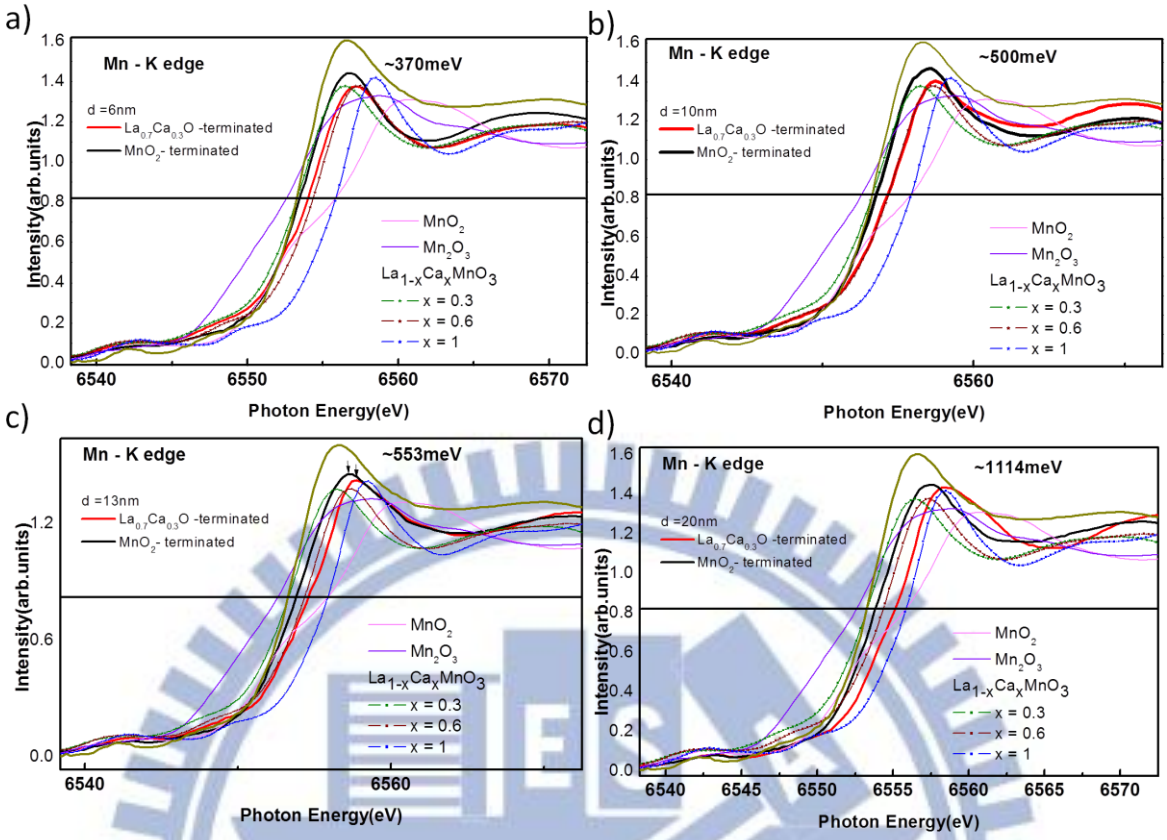

Figure 5.11 *Mn K -edge XAS spectra for LCMO/YBCO$_d$ with different interfaces at thickness of YBCO being 6nm, 10nm, 13nm, 20nm and are plotted together with spectra for the Mn_2O_3 (Mn^{3+}) and MnO_2 (Mn^{4+}) standard samples and reference samples , taken in fluorescence yield mode to demonstrate how to determine the valence state of Mn.*

The **Figure 5.11 a) - d)** show Mn K –edge XAS spectra with different interfaces at thickness of YBCO being 6nm, 10nm, 13nm, 20nm, respectively and are plotted together with spectra of the Mn_2O_3 (Mn^{3+}) and MnO_2 (Mn^{4+}) standard samples and reference samples of $La_{1-x}Ca_xMnO_3$ (x= 0.3, 1) and also our LCMO sample. We have drawn the standard line (that in the present case cuts the y-axis at 0.8) where, the spectra representing the MnO_2 (Mn^{4+}) and $La_{1-x}Ca_xMnO_3$ (x= 1) met together and the same line intersects with the spectra of the Mn_2O_3 (Mn^{3+}) and MnO_2 (Mn^{4+}) standard samples. This essentially indicates that the valence states of Mn^{3+} and Mn^{4+}, hence the valence state of our samples are defined by pointing out the spectra on the standard line by using the linear fit as shown in **Figure 5.6 b).** To confirm our experiment about the charge transfer and valence state, we also double checked with Mn L –edge, our results strongly support and are consistent with our Mn K –edge spectra as discussed.

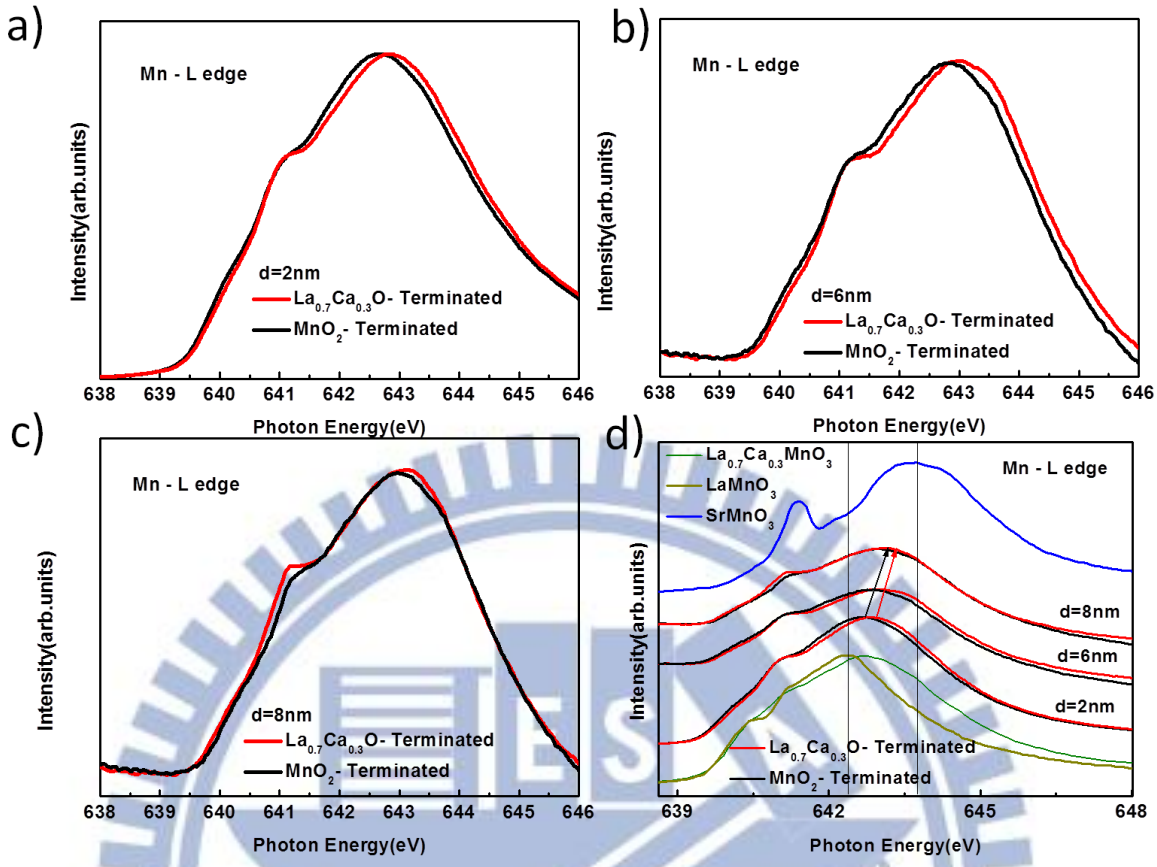

Figure 5.12 ***a)-c)*** *Mn-$L_{2,3}$ edge XAS spectra for LCMO/YBCO$_d$ with different interfaces with YBCO thicknesses of 2nm, 6nm and 8nm;* ***d)*** *Comparison of Mn L- edges XAS spectra LCMO/YBCO$_d$ with different interfaces with YBCO thicknesses of 2nm, 6nm and 8nm, and showing clearly the energy shifts after putting the YBCO thicker, taken in total electron yield mode.*

The TEY signal was used to probe the electronic and magnetic structure of the MnO_2 layers at the interface for the low electron escape depth (a few nanometers), and contributions from deeper layers are exponentially decreased. **Figure 5.12** shows the XAS spectra of the Mn-$L_{2,3}$ edge of the YBCO/LCMO heterostructures with a fixed LCMO thickness of 10nm and YBCO thicknesses of 2nm, 6nm and 8nm. The energy difference of the Mn L_3-edge absorption peak between the two interfacial terminations increases with the increment of the YBCO layer thickness, with energy differences of around 90 meV, 300 meV, and 400 meV corresponding respectively to YBCO thicknesses of 2nm, 6nm and 8nm. We also noticed the spectral shifts of the Mn L_3-edge moving towards higher energy for both terminated interfaces which indicates an increase in the oxidation state of the Mn ions. The spectral shifts are larger in the $La_{0.7}Ca_{0.3}O$-terminated interface than in the MnO_2-terminated one. The increase of

Mn^{4+} with YBCO thickness clearly reveals that the charge transfer across the interface between two terminations with different work functions, hence the magnetization decreases as the valence state of Mn (Mn^{4+}) increases, which is also consistent with our Mn-*K* edge data.

Finally, to rule out the effects of the SRO layer, we also tried using the SrMnO (SMO) buffer layer to switch the termination rather than SRO, and identical results were observed. Therefore, all the observed effects presented here are apparently not due to the SRO buffer layer.

5.4 Conclusion

To conclude this topic, this finding would have been impossible without an atomically precise interface control. We have shown that the interfaces control has played prominent role on affecting the magnetic and electronic properties of F/S heterostructures charge transfer at both interfaces in STO/LCMO/$YBCO_d$ and STO/SRO/LCMO/$YBCO_d$ structures. The charge transfer is stronger at the $La_{0.7}Ca_{0.3}O$-terminated interface than at the MnO_2-terminated interface. This mechanism is responsible for the larger number of holes in the CuO_2 planes in the $La_{0.7}Ca_{0.3}O$-terminated samples and hence high Tc. All the observations of superconductivity, magnetism, and XAS concur with the newly discovered charge transfer in this YBCO/LCMO system.

References

[1] H. Y. Hwang, Y. Iwasa, M. Kawasaki, B. Keimer, N. Nagaosa, Y. Tokura, *Nature Mater*. **2012**, 11, 103–13.

[2] A. Ohtomo, H. Y. Hwang, *Nature* **2004**, 427, 423–6.

[3] J. Biscaras, N. Bergeal, A. Kushwaha,; T. Wolf, A. Rastogi, R. C. Budhani, J. Lesueur, *Nature Comm*. **2010**, 1, 89.

[4] J. Chakhalian, J.W. Freeland, H,-U. Habermeier, G. Cristiani, G. Khaliullin, M. van Veenendaal, B. Keimer, *Science*. **2007**, 318, 1114–1117.

[5] J. Chakhalian, J.W. Freeland, G. Srajer, J. Strempfer, G. Khaliullin, J.C. Cezar, T. Charlton, R. Dalgliesh, C. Bernhard, G. Cristiani, H.-U. Harbermeier, B. Keimer, *Nature Phys*. **2006**, 2, 244–248.

[6] Y.-H. Chu, L.W. Martin, M.B. Holcomb, M. Gajek, S.-J. Han, Q. He, N. Balke, C.-H. Yang, D. Lee, W. Hu, Q. Zhan, P.,-L. Yang, A. Fraile-Rodriguez, A. Scholl, S.X. Wang, R. Ramesh, *Nature Mater*. **2008**, 7, 478–82.

[7] P. Yu, Y.-H. Chu, R. Ramesh, *Materials Today*. **2012**, 15, 320–327.

[8] C. A. R. Sa de Melo, *Phys. Rev. Lett*. **1997**, 79, 8–11.

[9] V. Peña, *Phys. Rev. B.* **2006**, 73, 104513.

[10] J. Stahn, J. Chakhalian, Ch. Niedermayer, J. Hoppler, T. Gutberlet, J. Voigt, F. Treubel, H.-U. Habermeier, G. Cristiani, B. Keimer, C. Bernhard, *Phys. Rev. B.* **2005**, 71, 140509.

[11] S. Soltan, J. Albrecht, H.-U. Habermeier, *Phys. Rev. B.* **2004**, 70, 144517.

[12] Z. Sefrioui, D. Arias, V. Pena, J.E. Villeegas, M. Varela, P. Prieto, C. Leon, J.L. Martinez, J. Santamaria, *Phys. Rev. B.* **2003**, 67, 214511.

[13] E. Dagotto, *Science*. **2007**, 318, 1076–1077.

[14] J. Hoppler, J. Stahn, Ch. Niedermayer, V.K. Malik, H. Bouyanfif, A.J. Drew, M. Rossle, A. Buzdin, G. Cristiani, H.U. Habermeier, B. Keimer, C. Bernhard, *Nature Mater*. **2009**, 8, 315–9.

[15] P.Fulde and R.A.Ferrell, *Physical Review* **1964**, 135, A550.

[16] A. I. Larkin and Y.N.Ovchinnikov, *Soviet Physics Journal for Experimental and Theoretical Physics* **1965**, 20, 762.

[17] J.Bardeen, L.N.Cooper and J.R. Schrieffer, *The Physical Review* **1957**, 108, 1175.

[18] Z.Radovi´c, M. Ledvij, L.Dobrosavljevi´c-Gurji´c, A.I.Buzdin and J.R.Clem, *Physical Review B* **1991**, 44, 759.

[19] K.D.Usadel, *Physical Review Letters* **1970**, 25, 507.

[20] L.V.Mercaldo, C.Attanasio, C.Coccorese, L.Maritato, S.L.Prischepa and M. Salvato,

Physical Review B **1996**, 53, 14040.

[21] Th.M¨uhge, N.N.Garif'yanov, Yu.V.Goryunov, G.G.Khaliullin, L.R.Tagirov, K.Westerholt, I.A.Garifullin and H. Zabel, *Physical Review Letters* **1996**, 77, 1857.

[22] J.S. Jiang, D.Davidovi´c, D.H.Reich and C.L.Chien, Physical Review B 1996, 54, 6119.

[23] I.Baladi´e and A.I.Buzdin, *Physical Review B* **2003**, 67, 014523.

[24] M.Giroud, H.Courtois, K.Hasselbach, D.Mailly and B.Pannetier, *Physical Review B* **1998**, 58, R11872.

[25] F.S.Bergeret, A.F.Volkov and K.B.Efetov, *Physical Review Letters* **2001**, 86, 4096.

[26] F.S.Bergeret, A.F.Volkov and K.B.Efetov, *Physical Review B* **2004**, 69, 174504.

[27] F.S.Bergeret, A.F.Volkov and K.B.Efetov, *Reviews of Modern Physics* **2005**, 77, 1321.

[28] Z. Sefrioui, D.Arias, V.Pe˜na, J.E.Villegas, M.Varela, P.Prieto, C. Le´on, J.L.Martinez and J. Santamaria, *Physical Review B* **2003**, 67, 214511.

[29] W.E.Pickett and D.J. Singh, *Physical Review B* **1996**, 53, 1146.

[30] V.Pe˜na, Z. Sefrioui, D.Arias, C. Le´on, J. Santamaria, J.L.Martinez, S.G.E. Velthuis and A.Hoffmann, *Phys. Rev. Lett.* **2005**, 94, 057002.

[31] I.Baladi´e and A.I.Buzdin, *Physical Review B* **2003**, 67, 014523.

[32] B. Lake, H.M.Rønnow, N.B.Christensen, G.Aeppli, K. Lefmann, D.F.McMorrow, P.Vorderwisch, P. Smeibidl, N.Mangkorntong, T. Sasagawa, M.Nohara, H.Takagi and T.E.Mason, *Nature* **2002**, 415, 299.

[33] B. Lake, K. Lefmann, N.B.Christensen, G.Aeppli, D.F.McMorrow, H.M.Rønnow, P.Vorderwisch, P. Smeibidl, N.Mangkorntong, T. Sasagawa, M.Nohara and H.Takagi, *Nature Materials* **2005**, 4, 658.

[34] J.Chang, A.P. Schnyder, R.Gilardi, H.M.Rønnow, S.Pailhes, N.B.Christensen, Ch.Niedermayer, D.F.McMorrow, A.Hiess, A. Stunault, M.Enderle, B. Lake, O. Sobolev, N.Momono, M.Oda, M. Ido, C.Mudry and J.Mesot, *Physical Review Letters* **2007**, 98, 077004.

[35] A.M.Goldman, V.Vas'ko, P.Kraus, K.Nikolaev and V.A. Larkin, *Journal of Magnetism and Magnetic Materials* **1999**, 200, 69.

[36] G. Jakob, V.V.Moshchalkov and Y.Bruynseraede, Applied Physics Letters 1995 66, 2564.

[37] V.A.Vas'ko, V.A. Larkin, P.A.Kraus, K.R.Nikolaev, D.E.Grupp, C.A.Nordman and A.M.Goldman, *Physical Review Letters* **1997**, 78, 1134.

[38] H.-U.Habermeier and G.Cristiani, *Journal of Superconductivity: Incorporating Novel Magnetism* **2002**, 15, 425.

[39] T.Holden, H.-U.Habermeier, G.Cristiani, A.Golnik, A.Boris, A.Pimenov, J.Huml´ıˇcek,

O.I. Lebedev, G.Van Tendeloo, B.Keimer and C.Bernhard, *Physical Review B* **2004**, 69, 064505.

[40] N.Haberkorn, J.Guimpel, M. Sirena, L.B. Steren, W. Saldarriaga, E.Baca and M.E.G´omez, *Applied Physics Letters* **2004**, 84, 3927.

[41] S.J. Pennycook et al. PACS: 68.37.Lp, 74.78.Fk, 74.78.-w, 79.20.Uv, 68.65.Cd.

[42] P. Yu, W. Luo, D. Yi, J.X. Zhang, M.D. Rossell, C.-H. Yang, L. Luo, G. Singh-Bhalla, S.Y. Yang, Q. He, Q.M. Ramasse, R. Erni, L.W. Martin, Y.-H. Chu, S.T. Pantelides, S.J. Pennycook, R. Ramesh, *Proceedings of the National Academy of Sciences of the United States of America*. **2012**, 109, 9710–9715.

[43] H.-U. Habermeier, *Journal of Physics: Conference Series*. **2008**, 108, 012039.

[44] J. Salafranca, S. Okamoto, *Phys. Rev. Lett*. **2010**, 105, 1–4.

[45] C. B. Cai, L. Peng, B. Holzapfel, X.M. Xie, Z.Y. Liu, Y.M. Lu, C.Z. Chen, *Supercond. Sci. Technol.*. **2010**, 23, 034010.

Chapter 6: Summary

In this dissertation, we have tried to unveil the functional of the control the interaction in the complex oxides interfaces, whether they applied to study the two dimensional electron gas (2DEG) of LAO/STO interface or coupling between the ferromagnetism and superconducting in LCMO/YBCO system. As we have known that interfaces have emerged as focal points of current condensed matter physics. In strongly correlated oxides, heterointerfaces provide a powerful route to create and manipulate the charge, spin, orbital, and lattice degrees of freedom, suggesting new possibilities for next generation devices and creating a huge playground to discover new emergent phenomena.

The appearance of controlling the conductivity in LAO/STO interface by ferroelectric of PZT has provided potentiality to improve the quality of devices and enhance physical functionalities or create additional functionalities for future devices. One of the famous ferroelectric materials is PZT, which is widely studied recently. The other is the high mobility of 2DEG in LAO/STO interface. Therefore, PZT and LAO/STO have been chosen for investigating the ferroelectric control of the conduction at the LAO/STO heterointerface. Our structure PZT/LAO/STO shows that both PZT and LAO are grown epitaxially on STO(100) - oriented substrates and revealed clearly that we are successful in placing the ferroelectric of PZT on top of 2DEG of LAO/STO interface. In addition, our transport measurement with the ferroelectric effect sets in and the sheet resistance starts increasing with PZT thickness showing the strong impact of the intrinsic polarization (P_{up}) of the PZT on electron conduction at the interface. Moreover, by increasing the thickness of LAO, while thickness of PZT was kept constant (20nm), we also realized that the sheet resistance decreases when lowering the temperature and increases when the thickness of LAO is reduced. Based on our results, we can estimate that the resistance is increased by an order of magnitude when the LAO thickness is cut down to 1uc. The most important thing is that the sheet resistance can be modulated the conductivity at LAO/STO interface by not only the polarization (PZT thickness dependence) but also the different polarization states of PZT (P_{up} –state and P_{down} –state). Especially, another intriguing feature here is the switch of an insulating state to a conducting state. Beside that our XPS and XSTM results provide more evidence about the band bending at LAO/STO interface under the control of the polarization states of PZT. The energy shift of the band edges in LAO is smaller for the P_{down} –state sample than that for the P_{up} –state sample which indicates that the electric field in LAO layer diminishes after the polarization of the PZT is switched from the natural P_{up} –state to the P_{down} –state. Additionally, in the

theoretical calculation is constistent with our experimental results.

In order to search for new types of oxide interfaces, we explored the ferromagnetic $La_{2/3}Ca_{1/3}MnO_3$/superconducting $YBa_2Cu_3O_{7-x}$ heterostructures of two distinct interfaces with atomically precise interface control to study the coupling between these two functional layers and identified a new mechanism of charge transfer in the $YBa_2Cu_3O_{7-x}/La_{0.7}Ca_{0.3}MnO_3$ (YBCO/LCMO) hetrostructures.

From our transport data, the depression of T_c indicates the enhanced interaction between superconductivity and magnetism. Based on our transport results we can conclude that controlling the interfaces is very crucial to manipulate the superconducting and other physical properties at the heterostructure of YBCO/LCMO interfaces. In addition to different T_c, different terminations also lead to different magnetic properties in these heterostructures. In our system, both the decreased T_c of YBCO with decreasing YBCO thickness and the decreased magnetization of LCMO with increasing YBCO thickness both qualitatively fit into the proximate scenario. To explain our results, we illustrate the charge transfer model at two different interfaces: $La_{0.7}Ca_{0.3}O$-terminated interface model, CuO chains are closer to MnO planes and the transfer of electrons from the MnO planes to CuO chains is relatively easier. On the other hand, with the MnO_2-terminated interface model, CuO chains are far from MnO planes. Therefore, the electron transfer from MnO planes to CuO chains is weaker. According to the present models, this is due to the change of the Mn^{4+} to Mn^{3+} ratio. For the thicker YBCO layer, the charges transfer from LCMO to YBCO layer leads to more Mn^{4+} ions, and thus the reduction of Mn magnetization. The same YBCO thickness, the 528 eV peak O *K*-edge XAS demonstrates the increase in the number of holes with increasing YBCO thickness, which certainly contribute to the enhancement of T_c.

The present work on the second topic highlights new development of multifunctional device applications of interfaces between the ferromagnetism and superconducting in $YBa_2Cu_3O_{7-x}/La_{0.67}Ca_{0.33}MnO_3$ and deeper understanding of underlying physics in which only shows on the terminations control such as the interaction, frustration, charge, orbital, and spin degrees of freedom, proximate effect, is critical to the superconductivity, magnetism. The above-mentioned conclusions disclose a reason for control the interaction in complex oxides interfaces. The oxide interfaces show a lot of possibilities in either promoting the usability of functionalities or creating different connectivity of structures for artificially designing new interaction mechanisms. Hence, fully understanding the physics behind these oxides interfaces systems is a critical issue for further applications.

Supporting Materials

Appendix B. Electric field in LAO calculations

By E. A. Eliseev, Prof. A. N. Morozovska

Institute of Problems of Material Sciences and Institute of Physics, National Academy of Science of Ukraine, Kiev, Ukraine

Equations of state relate electrical displacement **D** and electric field **E** in the LAO dielectric gap as

$$\mathbf{D}_g = \varepsilon_0 \varepsilon_g \mathbf{E}_g , \qquad \textbf{(B.1)}$$

In PZT the electric displacement is:

$$\mathbf{D}_f = \varepsilon_0 \mathbf{E}_f + \mathbf{P} \approx \varepsilon_0 \hat{\varepsilon}_{ij}^f \mathbf{E}_f + \mathbf{P}_S(x,z). \qquad \textbf{(B.2)}$$

Here $\mathbf{P}(x,z)$ is polarization vector, $\mathbf{P}_S(x,z) = \left(0,0,\mathrm{P}_3(x,z)\right)$ is spontaneous polarization vector.

Electrostatic quasi-stationary Maxwell equation rot **E**=0 should be valid in the actual frequency range, giving one the opportunity to introduce the potential φ of quasi-stationary electric field, $\mathbf{E}_{g,f}(x,z,t) = -\nabla\varphi_{g,f}(x,z,t)$. Inside the dielectric gap potential φ satisfies Laplace's equation. For STO we regard the Debye approximation validity. Along with and Eqs.(B.1)-(B.2) leads to

$$\left(\frac{\partial^2}{\partial z^2} + \frac{\partial^2}{\partial x^2}\right)\varphi_S - \frac{\varphi_S}{R_d^2} = 0, \qquad \text{for} \quad -\infty < z < 0, \quad \text{(STO)} \qquad \textbf{(B.3a)}$$

$$\left(\frac{\partial^2}{\partial z^2} + \frac{\partial^2}{\partial x^2}\right)\varphi_g = 0 , \qquad \text{for} \quad 0 < z < h , \quad \text{(LAO)} \qquad \textbf{(B.3b)}$$

$$\left(\varepsilon_{33}^f \frac{\partial^2}{\partial z^2} + \varepsilon_{11}^f \frac{\partial^2}{\partial x^2}\right)\varphi_f = 0, \qquad \text{for} \quad h < z < L. \quad \text{(PZT)} \qquad \textbf{(B.3c)}$$

In Eq.(B.3) we used that $\mathrm{div}\mathbf{P}_S(x) = 0$ for uncharged 180-degree domain structure. Eqs.(B.3) should be supplemented with the boundary conditions of zero potentials at $z << -R_d$ and $z = L$, continuous potential and normal component of displacement on the boundaries between semiconductor STO, dielectric gap LAO and ferroelectric PZT, namely

$$\varphi_S\left(x, z << -R_d\right) \to 0, \qquad \textbf{(B.4a)}$$

$$\varphi_S(x,0)=\varphi_g(x,0),\qquad D_{gn}(x,0)=-\varepsilon_g\frac{\partial\varphi_g(x,0)}{\partial z}=\sigma(x,0),\qquad \textbf{(B.4b)}$$

$$\varphi_g(x,h)=\varphi_f(x,h),\qquad \textbf{(B.4c)}$$

$$D_{fn}-D_{gn}=-\varepsilon_{33}^f\frac{\partial\varphi_f(x,h)}{\partial z}+\frac{P_3(x,h)}{\varepsilon_0}+\varepsilon_g\frac{\partial\varphi_g(x,h)}{\partial z}=0,\qquad \textbf{(B.4d)}$$

$$\varphi_f(z=L)=0.\qquad \textbf{(B.4e)}$$

Keeping in mind that the effective gap $h+R_d\approx H$ can be introduced in order to obtain an approximate analytical solution[S1, S2], the stray and depolarization electric field in LAO and PZT layers correspondingly have the form:

$$E_{g3}(x,0<z<h)=\int_{-\infty}^{+\infty}dk_x\frac{\exp(-ik_x x)}{2\pi\varepsilon_0}\times\frac{\gamma\tanh(k_x L/\gamma)\cosh(k_x z)\widetilde{P}_3(k_x)}{\varepsilon_{33}^f\sinh(k_x H)+\gamma\varepsilon_g\tanh(k_x L/\gamma)\cosh(k_x H)}.$$

(B.5)

$$E_{f3}(x,z>h)=\int_{-\infty}^{+\infty}dk_x\frac{\exp(-ik_x x)}{2\pi\varepsilon_0}\times\frac{-\widetilde{P}_3(k_x)\tanh(k_x H)\cosh(k_x(L+H-z)/\gamma)}{\varepsilon_{33}^f\cosh(k_x L/\gamma)\tanh(k_x H)+\gamma\varepsilon_g\sinh(k_x L/\gamma)}.$$

(B.6)

Here $\gamma=\sqrt{\varepsilon_{33}^f/\varepsilon_{11}^f}$ is the dielectric anisotropy factor, $\widetilde{P}_S(k_x)$ is the Fourier image of $P_S(x)$ over coordinates *x* Periodic domain structure of conventional rectangular shape and period *a* can be expanded in Fourier series as

$$P_3(x)\approx\sum_{m=0}^{\infty}P_m\sin(k_m x),\qquad P_m\approx\frac{4}{(2m+1)\pi},\qquad k_m=\frac{2\pi}{a}(2m+1).\qquad \textbf{(B.8a)}$$

Corresponding Fourier image is

$$\widetilde{P}_3(k_x)\propto\sum_m\frac{P_m}{2i}\left(\delta(k_x-k_m)-\delta(k_x+k_m)\right)\qquad \textbf{(B.8b)}$$

The stray field is:

$$E_3(x,0<z<h)=\sum_m\frac{P_m}{\varepsilon_0}\frac{\gamma\tanh(k_m L/\gamma)\cosh(k_m z)\sin(k_m x)}{\varepsilon_{33}^f\sinh(k_m H)+\gamma\varepsilon_g\tanh(k_m L/\gamma)\cosh(k_m H)}\qquad \textbf{(B.9)}$$

The stray field (B.9) causes redistribution of the free charge density in accordance Boltzmann

statistics, $p(x,z) \approx p_0 \exp\left(-\frac{e\varphi(x,z)}{k_B T}\right)$ and $n(x,z) \approx n_0 \exp\left(\frac{e\varphi(x,z)}{k_B T}\right)$, where the potential $\varphi(x,z) = -\int_{-\infty}^{z} E_3(x,z')dz' \approx \int_{-R_d}^{z} E_3(x,z')dz'$ is

$$\varphi(x,z) = \sum_m \frac{P_m}{\varepsilon_0} \frac{-\gamma \sin(k_m x)\tanh(k_m L/\gamma)(\sinh(k_m R_d)+\sinh(k_m z))/k_m}{\varepsilon_{33}^f \sinh(k_m H)+\gamma\varepsilon_g \tanh(k_m L/\gamma)\cosh(k_m H)} \quad \textbf{(B.10)}$$

Spatial x-distributions of polarization in the stripe 180-degree domain structure, stray depolarizing field $E_3(x,z)$ existing in LAO layer and STO surface charge $\rho_S(x)$ are shown in **Figures B1**. One can see from the figures that the spontaneous polarization direction in PZT can indeed modulate the surface charge density $\rho_S(x)$ in STO via the stray field $E_3(x,z)$ existing in LAO layer. Polarization distribution has conventional rectangular shape (**Figure B1a** and **b**). Charge and field x-profiles shape and amplitude strongly depend on the period of domain structure *a* in PZT. Appeared that for the case $a >> L$ and the stray field weakly depends on the position z in LAO and thus remains strong enough at the LAO/STO interface $z = 0$ (**Figure B1c**). For the case $a << L$ and the stray field strongly depends on the position z in LAO and essentially decreases at the LAO/STO interface $z = 0$ (**Figure B1d**). Thus the total charge density accumulated in STO is much smaller for the case $a << L$ than the one at $a > L$ (compare **Figure B1f** and **e**).

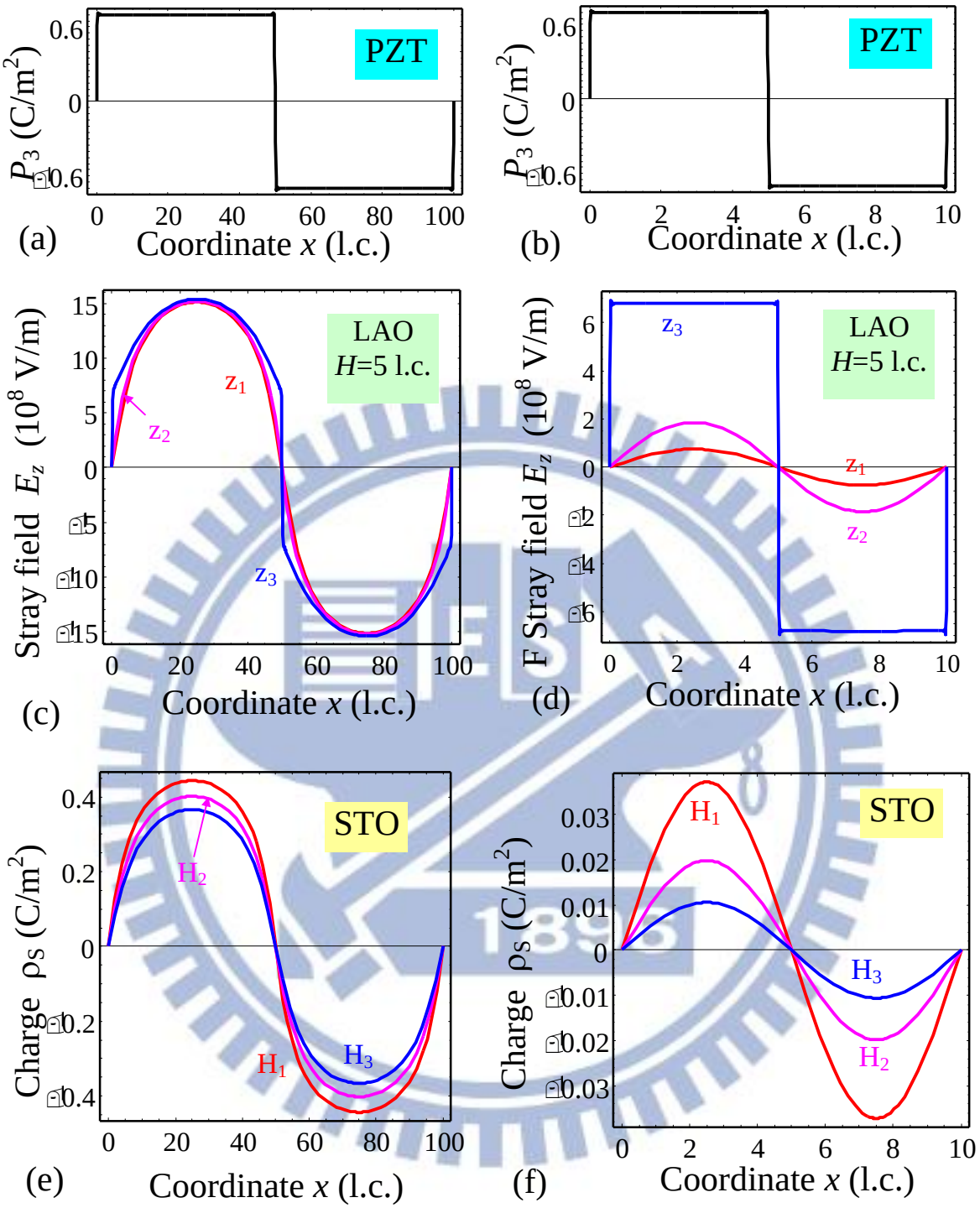

Figure B1. X-profile of PZT spontaneous polarization in the stripe 180-degree domain structure **(a, b)**, stray depolarizing field $E_3(x,z)$ existing in LAO layer **(c, d)** and "sheet" charge $\rho_S(x)$ located in the vicinity of STO surface **(e,f)**. PZT thickness L=50 l.c., LAO thickness H_1=4, H_2=5, H_3=6 l.c., depth z_1=0, z_2=0.5H, z_3=H, domain structure period a=100 l.c. (a, c, e) and a=10 l.c. (b,d, f). Abbreviation l.c. stands for lattice constant units.

References:

S1. E. A. Eliseev, A. N. Morozovska, S. V. Kalinin, Y. Li, J. Shen, M. D. Glinchuk, L. Q. Chen, V. Gopalan, *J. Appl. Phys.* **2009,** *106*, 084102.

S2. E. A. Eliseev, A. N. Morozovska, G. S. Svechnikov, E. L. Rumyantsev, E. I. Shishkin, V. Y. Shur, S. V. Kalinin, *Phys. Rev. B* **2008,** *78*, 245409.

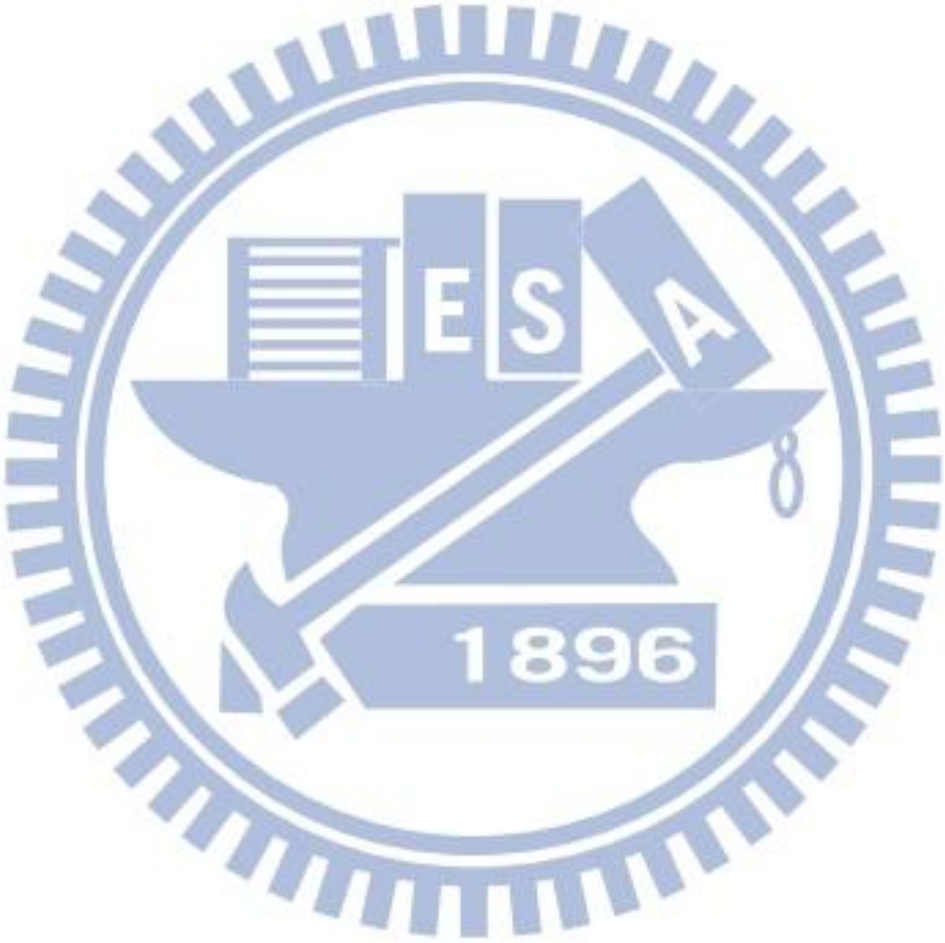

Appendix C. Phase-Field Modeling of Ferroelectric Modulation at LAO/STO Interface

By Y. Cao, Prof. L. Q. Chen

Department of Materials Science and Engineering, Pennsylvania State University, University Park, Pennsylvania, 16802, USA

We introduce the phase-field approach with the band structure theory to study the effect of PZT ferroelectricity on the electronic conductivity at LAO/STO interface in a STO/LAO/PZT heterostructure. We consider n-type STO layer and LAO dielectric layer topped by a ferroelectric PZT (Zr-rich) with out of plane polarization. The schematic band diagram of the STO/LAO/PZT heterostructure is plotted in **Figure C1a**. It is seen that the band bending at the STO/LAO interface is about 0.3eV, which causes electron accumulation at the interface. The steady state profile of potential and electrons in the absence of ferroelectric polarization from PZT layer are obtained by solving the following coupled equations to steady state, which are plotted in **Figure C1b** and **c**.

$$\nabla^2\psi = -\frac{\rho}{\varepsilon_0\varepsilon_r} = \frac{e_0 n}{\varepsilon_0\varepsilon_r} \qquad \textbf{(C.1)}$$

$$\frac{\partial n}{\partial t} = -\nabla \bullet J = D\nabla^2 n - \mu\nabla \bullet \left(n\nabla\psi\right) \qquad \textbf{(C.2)}$$

in which ψ is the electric potential, ρ is the charge density, e_0 is the unit charge, n is the electron concentration, ε_0 is the vacuum permittivity and ε_r is the dielectric constant of STO. D and μ stand for the diffusivity and mobility of electrons in STO respectively.

In order to study the effect of polarization on the local conductivity, we assume PZT in single tetragonal domain structure with out of plane polarization. No defects are considered in the PZT layer. The polarization modulated STO/LAO band diagrams are schematically displayed in **Figure C2a** and **b**. The polarization induced bound charges are introduced through $\rho = -\nabla \bullet P$. At the LAO/PZT interface the polarization reduces to 0. Therefore a sheet of negative bound charge is formed at the LAO/PZT interface in the case of upward polarization P_{up}. (**Figure C2c**) Based on the Poisson equation,

$$\nabla^2\psi = \frac{\nabla \bullet P_i}{\varepsilon_0\varepsilon_r} \qquad \textbf{(C.3)}$$

The electric potential drop at the LAO/PZT interface due to the negative polarization bound charge is calculated to be around -0.5V (**Figure C2d**). Since electric potential should be

continuous throughout the heterostructure, the potential decrease through the STO and LAO should be equal to the potential drop at the LAO/PZT interface. In addition, the effective length within STO is about 0.8nm while the thickness of the LAO layer is about 1.1nm. Therefore we estimate the potential drop in at the STO/LAO interface from the following equation,

$$\Delta V_{total} = \Delta V_{STO/LAO} + \Delta V_{LAO} = \left(\frac{a_{STO}^{eff}}{a_{STO}^{eff} + a_{LAO}} \right) \Delta V_{total} + \left(\frac{a_{LAO}}{a_{STO}^{eff} + a_{LAO}} \right) \Delta V_{total} \quad \textbf{(C.4)}$$

in which $\Delta V_{STO/LAO}$ and ΔV_{LAO} stand for potential drop at the interface and inside LAO respectively. a_{STO}^{eff} and a_{LAO} are the effective length within STO and thickness of LAO respectively. From **Equation (C.4)** the potential decreases by 0.2V at the STO/LAO interface, and interface band bending decreases from 0.3V to 0.1V. As a consequence, the free electrons are depleted from the LAO/STO interface and the electronic conductivity decreases. On the other hand, when the polarization is pointing downward inside the PZT layer, a positive sheet of bound charges is formed at the LAO/PZT interface (**Figure C2e**), which increases the local potential at the LAO/PZT interface and the band bending at the STO/LAO interface (**Figure C2f**). As a consequence electrons are attracted to the STO/LAO interface and the local electronic conductivity increases.

The electric potential bending, the electron concentration and the electronic conductivity inside the effective length of STO layer have been calculated and compared in **Figure C3**. The electronic conductivity is calculated to be $\sigma = ne_0\mu$. It is clearly seen that the polarization in PZT layer has a significant effect on the electron concentration and conductivity in the STO/LAO interface. The electron concentration away from the STO/LAO interface region is ~10^9cm^{-3}. When the ferroelectric polarization inside PZT layer is downward pointing, the electron accumulation significantly reaches up to 10^{18}cm^{-3} with band bending of ~0.5V in the vicinity of STO/LAO interface. And the local conductivity is calculated to be ~10^0 $\Omega^{-1}cm^{-1}$, indicating that the interface becomes more conducting (**Figure C3c**). The electron accumulation is strongly inhibited (~10^{11}cm^{-3}) when the polarization in PZT layer is pointing upward, with interface band bending of 0.1V. In this case the interface becomes less conducting of local conductivity of $\sim 10^{-7}\,\Omega^{-1}cm^{-1}$.

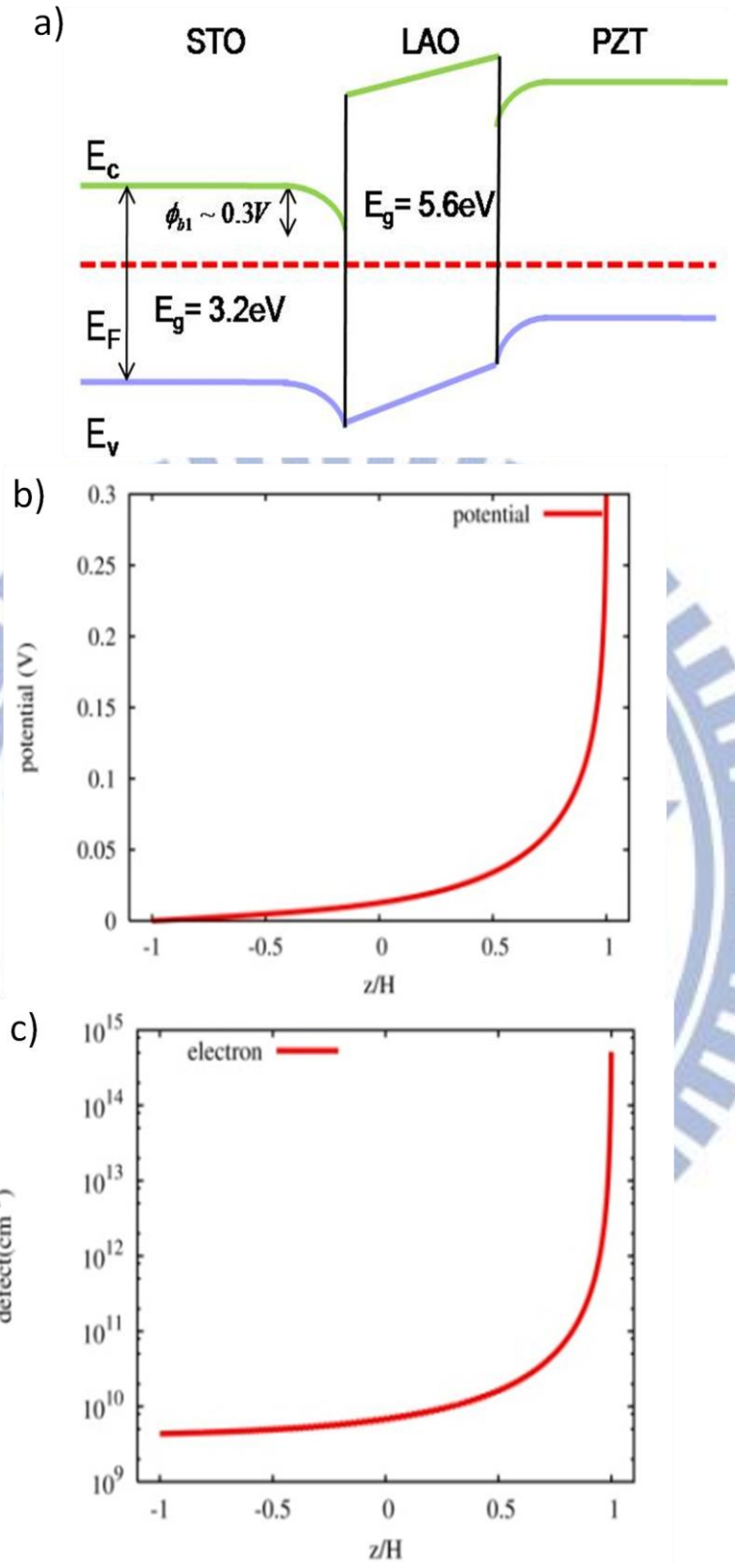

Figure C1. *(a) Schematic band diagram of STO/LAO/PZT heterojunction; (b) the electric potential distribution in the absence of polarization; (c) the electron concentration in the absence of polarization (z denotes the position in the STO layer, H is half of the layer thickness, so that z/H from -1 to +1 represents the entire layer)*

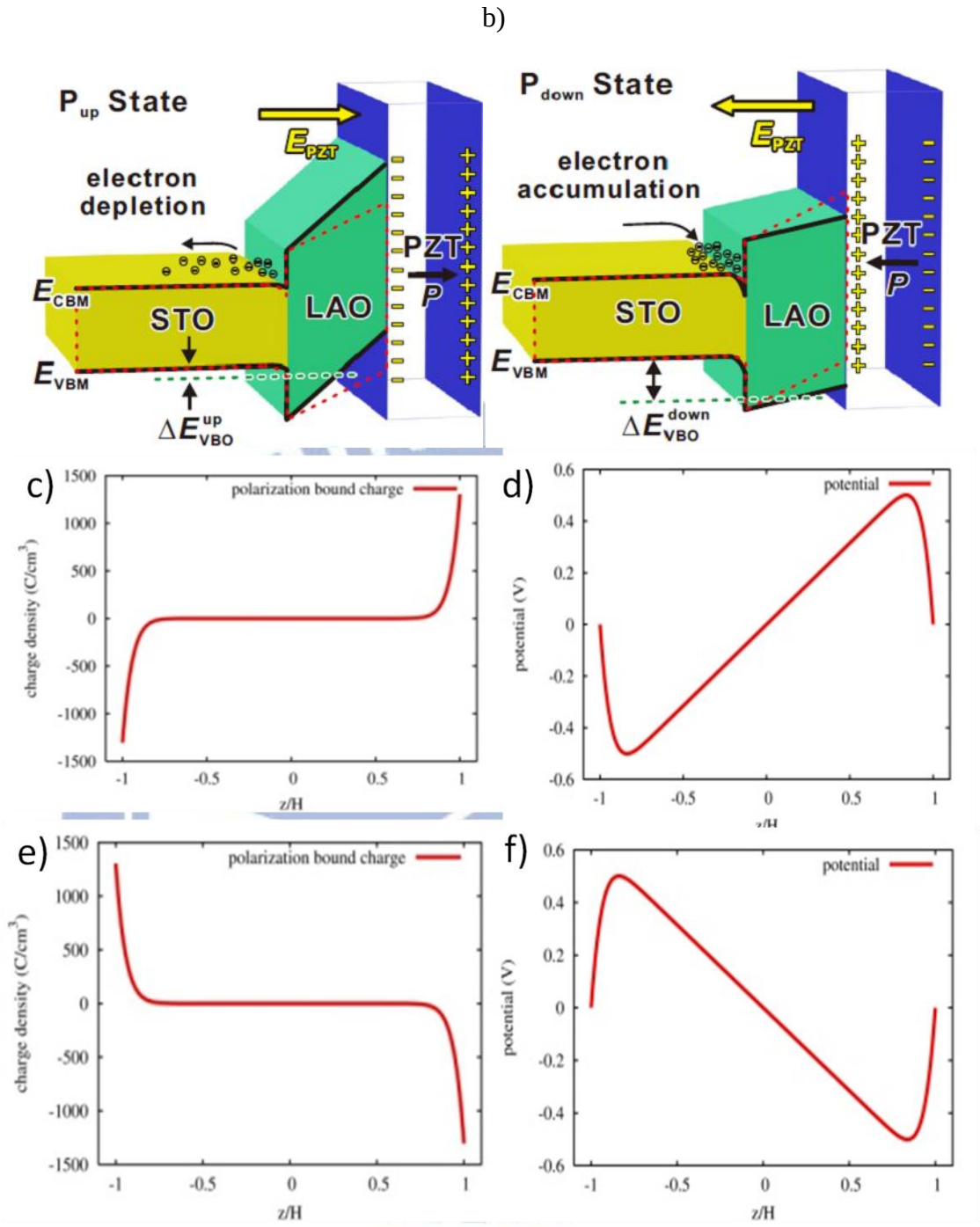

Figure C2. *Schematic band diagrams of a PZT/LAO/STO heterojunction in the presence of upward polarization P_{up} (a) and downward polarization P_{down} (b) in PZT layer. The polarization bound charge and electric potential distribution in PZT layer with upward polarization (c) and (d), and with downward polarization (e) and (f)*

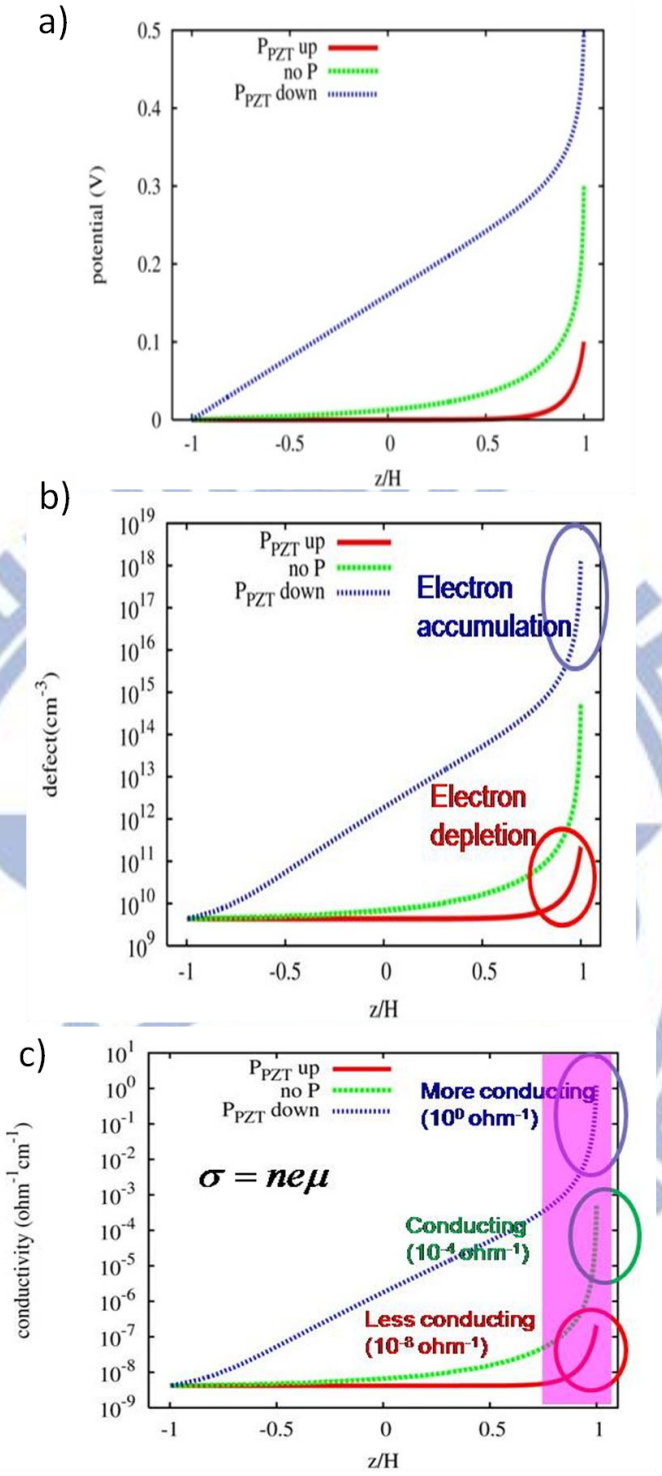

Figure C3. *Comparison of electric potential, electron concentration and local electronic conductivity in STO layer in the presence of upward polarization, no polarization and downward polarization in PZT layer (z denotes the position in the STO layer, H is half of the layer thickness, so that z/H from -1 to +1 represents the entire layer)*